AFRL-IF-RS-TR-2005-228
Final Technical Report
June 2005

SINGLE MOLECULAR DETECTION VIA MICRO-SCALED POLYMERIC OPTO-ELECTRO-MECHANICAL SYSTEMS

University of California at Berkeley

APPROVED FOR PUBLIC RELEASE; DISTRIBUTION UNLIMITED.

AIR FORCE RESEARCH LABORATORY
INFORMATION DIRECTORATE
ROME RESEARCH SITE
ROME, NEW YORK

STINFO FINAL REPORT

This report has been reviewed by the Air Force Research Laboratory, Information Directorate, Public Affairs Office (IFOIPA) and is releasable to the National Technical Information Service (NTIS). At NTIS it will be releasable to the general public, including foreign nations.

AFRL-IF-RS-TR-2005-228 has been reviewed and is approved for publication

APPROVED: /s/
GEORGE RAMSEYER
Project Engineer

FOR THE DIRECTOR: /s/
JAMES A. COLLINS, Acting Chief
Advanced Computing Division
Information Directorate

REPORT DOCUMENTATION PAGE

Form Approved
OMB No. 074-0188

1. AGENCY USE ONLY (Leave blank)	2. REPORT DATE	3. REPORT TYPE AND DATES COVERED
	June 2005	Final Sep 00 – May 04

4. TITLE AND SUBTITLE

SINGLE MOLECULAR DETECTION VIA MICRO-SCALED POLYMERIC OPTO-ELECTRO-MECHANICAL SYSTEMS

5. FUNDING NUMBERS
C - F30602-00-2-0568
PE - 63739E
PR - E117
TA - 00
WU - 55

6. AUTHOR(S)

Luke P. Lee, Albert P. Pisano, Lisa A. Pruitt and Daniel T. Chiu

7. PERFORMING ORGANIZATION NAME(S) AND ADDRESS(ES)

University of CA
Dept of Bioengineering
455 Evans Hall #1762
Berkeley, CA 94720-1762

8. PERFORMING ORGANIZATION REPORT NUMBER

9. SPONSORING / MONITORING AGENCY NAME(S) AND ADDRESS(ES)

Defense Advanced Research Projects Agency   AFRL/IFTC
3701 N. Fairfax Drive   26 Electronic Pky
Arlington, VA 22203   Rome, NY 13441-4514

10. SPONSORING / MONITORING AGENCY REPORT NUMBER

AFRL-IF-RS-TR-2005-228

11. SUPPLEMENTARY NOTES

12a. DISTRIBUTION / AVAILABILITY STATEMENT

Approved for Public Release; Distribution Unlimited.

12b. DISTRIBUTION CODE

13. ABSTRACT *(Maximum 200 Words)*

The BioPOEMS (Bio-Polymer-Opto-Electro-Microfluidic-System) Group at the University of CA at Berkley has developed three novel microfabricated, ultra-sensitive, opto-electro-mechanical systems for 'on-chip' optical detection. A micro Confocal Imaging Array (μCIA) system , a miniaturized Total Internal Reflection (mTIR) system and a Self-aligned Integrated Microfluidic Optical System (SI-MOS) have been fabricated to detect single molecules. Several Micro ElectroMechanical System (MEMS) opto-mechanical components and subsystems have been demonstrated, including stacked 2-D microlens scanners, vertically actuated lens devices for focul plane control, polydimethylsiloxane (PDMS) disposable chips with self-aligned objective lenses, multilayer chips with micromirror sidewalls for TIR excitation and polymer-based microactuators for sample handling.

14. SUBJECT TERMS
Microfluidics, microfluidics system, micro Microfluidic Imaging Array system, Minaturized Total Internal Reflection system, Self-aligned Integrated Microfluidic System, MEMS, 2-Dimensional scanner

15. NUMBER OF PAGES
177

16. PRICE CODE

17. SECURITY CLASSIFICATION OF REPORT	18. SECURITY CLASSIFICATION OF THIS PAGE	19. SECURITY CLASSIFICATION OF ABSTRACT	20. LIMITATION OF ABSTRACT
UNCLASSIFIED	UNCLASSIFIED	UNCLASSIFIED	UL

TABLE OF CONTENTS

List of Figures

List of Tables

1. EXECUTIVE SUMMARY

The goal of this effort was to engineer ultra-sensitive Micro-Polymer-Opto-Electro-Mechanical-Systems (*m*-POEMS) for biological and clinical applications. In particular, this work centered on the development of micro-optical systems with single molecule detection capabilities. To achieve this end, the following systems were developed: 1) a micro confocal imaging array (μCIA), 2) a miniaturized total internal reflection system (*m*TIR) and 3) a self-aligned integrated microfluidic system (Si-MOS). The possibility of integrating Surface Enhanced Raman Scattering (SERS) substrates with these systems was also explored. Additionally, a novel polymer-based technology was developed for constructing liquid-operated microactuators and microrobotic components for *in vitro* single cell manipulation.

An autonomous miniaturized total analysis system with 'on-chip' detection sites, as presented in Figure 1, shows the integration of a micro-optical system and polymer components with microfluidic channels. The novel design and microfabrication technology necessary to develop these prototype systems will allow portable, inexpensive optical systems to be built with detection limits comparable to those of conventional, bulky, macro-scale systems.
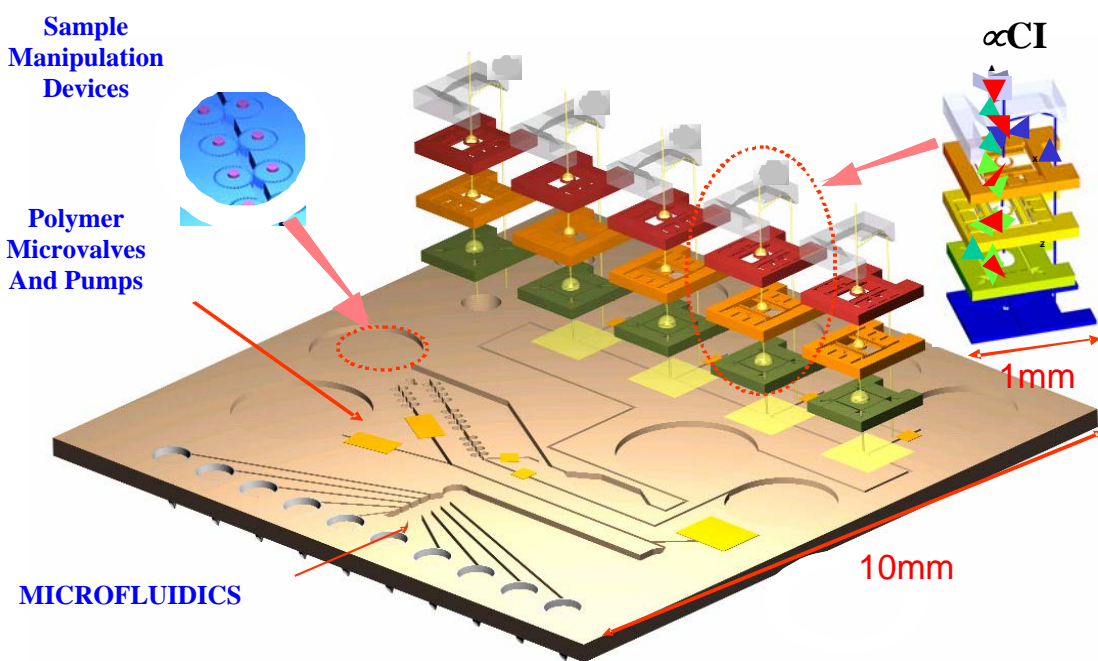
Figure 1. Schematic drawing of a fully integrated miniaturized analysis system with on-chip detection sites.

To accomplish the objective of developing a fully integrated miniaturized analysis system with on-chip detection sites, it was necessary to first develop five different microcomponents. These components included a micro scaled confocal imaging array, a miniaturized total internal reflection system, a self-aligned integrated microfluidic optical

system, surface enhanced Raman scattering substrates, and a polymer microrobotic system for single cell manipulation.

The micro-scaled confocal imaging array required the development of a miniaturized confocal laser scanning microscopes which could detect small excitation/detection volumes, and resulted in an increase in the signal to noise ratio (SNR) for epi-fluorescent detection. Micro active optical components to implement the scanning mechanism were required, and vertical integration was necessary. The key components of this array were a stacked 2-D microlens scanner for focusing, vertically actuated lens devices for focal plane control, microfabricated pinholes and collecting optics.

The Surface Enhanced Raman Scattering (SERS) required the development of substrates on integrated biochips. This resulted in high SERS signal amplification and convenient integration with the other components of the micro confocal imaging system. The key components included the batch-fabricated SERS substrates on silicon and Polydimethylsiloxane (PDMS), and the initial integration with the MEMS imaging system.

The Polymer Microrobotic Systems for Single Cell Manipulation included polymer microactuators that operated in physiological media. These microactuators were used to build complex microfluidic components such as valves, pumps, microrobotic systems, etc. These actuators were required to operate at low voltages (1-2 Volts) at approximately 22 $^{\circ}$C, which is slightly above ambient. The key components included using SU-8, a negative photoresist, as the structural material. The actuators were activated by passing a current through a thin metal resistor selectively attached to the suspended electrothermally activated polymer structure.

The Miniaturized Total Internal Reflection System was required to increase the SNR for small excitation volumes. A compact design enabled the vertical integration of all of the optical and fluidic components. The key components included a multilayer chip with micromirror sidewalls and the integration of micro/nano-fluidics on top of the multilayer chip for multiplexed detection.

The Self-aligned integrated Microfluidic Optical System (Si-MOS) included the integration of disposable microfluidic systems integrated with microfluidic channels, which increased the SNR of the disposable micro optical components fabricated in microfluidic channels. The key components included PDMS disposable microfluidic channels and the PDMS disposable self-aligned objective lenses.

These major accomplishments have also been disseminated by various publications, including 9 journal papers and 21 conference papers (Appendix I and II, respectively). Also, 7 overview presentations have been made at professional conferences

2. INTRODUCTION

More detailed descriptions of these components and systems are now presented.

2.1 SYSTEM COMPONENTS

The system components included micromachined scanners, variable focus liquid lenses, surface enhanced Raman spectroscopy substrates and polymer microrobotics.

2.1.1 MICROMACHINED SCANNERS

The micromachined scanners included stacked 2-dimensional microlens scanners, vertical microlenses, gimbaled 2-dimensional scanners and self-aligned vertical comb-drives.

2.1.1.1 Stacked 2-Dimensional Microlens Scanners

The control of the scanning of a laser beam is a basic requirement for optical systems such as barcode readers, laser printers, and scanning confocal microscopes. Even though numerous solid-state methods of optical scanning utilizing acousto-optic and electro-optic principles have recently been developed, mechanical scanners such as rotating polygon and galvanometric resonant mirrors are still more common. These mechanical scanners have relatively larger scanning angles, and are optimally tuned for large wavelength bands [1]. However, macro-scale mechanical scanners suffer from performance limitations related to power consumption, scanning speed, size and cost. Considering that many applications require multiple scanning units, the development of the miniaturization of mechanical scanners utilizing microfabrication technology is critical to making future optical systems more compact and affordable. Furthermore, those miniaturized scanners will be the basis for enabling new applications such as retinal projection displays [2-3], *in vivo* confocal microscopes [4,5] and free space optical communications for sensor networks [6].

Most miniaturized scanners are based on reflective scanning, which achieves time varying angular deflection of light through the angular rotation of sub-millimeter sized reflective surfaces. Reflective scanning devices, such as scanning micromirrors, are relatively straightforward to fabricate using silicon microfabrication technologies. Numerous silicon micromirror scanners have been developed using a variety of fabrication processes [7-9]. To achieve two-dimensional (2-D) scanning for many projection displays and imaging applications, two 1-D scanning micromirrors with orthogonal axis of rotation [4,10], or 2-D scanning micromirrors [11-13], have been used together with external lenses. In cases of reflective scanning, the optical axis is folded after reflection on each mirror surface, resulting in delicate alignment and packaging of separate focusing and scanning elements.

Transmissive scanning, in which incident light is deflected by translating a refractive element off of the optical axis, is an alternative to mechanical scanning. Transmissive scanners using moving lenses have advantages in terms of the alignment of

multiple optical components in the system, since the optical axis is not folded on the refractive surface, allowing multiple optical components to be aligned along a single optical axis. However, the fabrication of a transmissive scanner in micro-scale is not as simple as a reflective scanner, since it requires a microlens to be fabricated together with a microactuator. Microlenses need to be made of material that is transparent in the frequency ranges of interest. The substrate under the microlens is required to either be transparent or moved off the axis for light propagation when the optical axis is normal to the substrate.

Compared to micromirrors, only a few microscale transmissive scanners have been reported in the literature. Micromachined actuators with microlenses made of reflowed photoresist have been demonstrated for fiber optic switches, free space beam steering applications, and image scanners [14-16]. Microlenses from reflowed photoresist have relatively high transmission losses in the visible region [17], and the numerical apertures (N.A.) of these lenses are limited by the initial thicknesses of the photoresist films. For imaging applications in the visible range, high N.A. lenses (>0.3) with high transmittance (>95%) in the visible range are desired. Cascading independent 1-D transmissive scanners would have both for increased N.A. and provide fast 2-D scanning without cross talk in both the horizontal and the vertical directions [18].

2.1.1.2 Vertical Microlens

Three-dimensional (3-D) raster scanning is a key component for a wide range of photonic applications. Miniaturized 3-D raster scanning modules with low power requirements and low fabrication costs have been demonstrated in 3-D imaging MEMS microscopes [18], retinal displays [19], free space optical communication networks with micromotes [6], and 3-D MEMS memory [20]. As a first step, a 2-D raster scanner has been discussed in section 2.1.1 for in-plane scanning by stacking two independent transmissive microlens scanners. Integration of a vertically actuated microlens scanner to a 2-D scanner will allow a complete 3-D scanner (Figure 2).
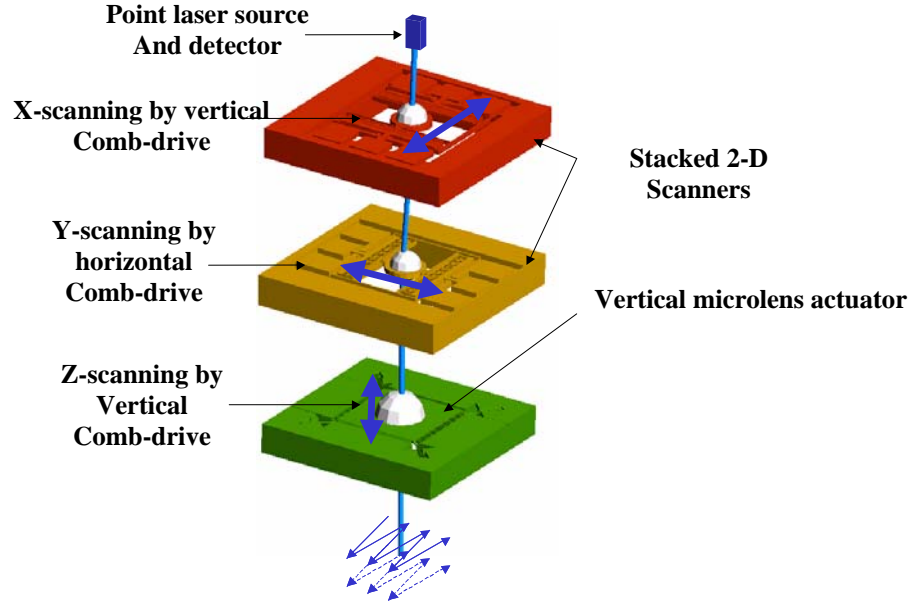
Figure 2. Concept of 3-D transmissive raster scanning.

The desired vertical actuation of microlenses for hand-held 3-D imaging should meet the following important requirements: large static and dynamic vertical displacement, low power consumption, linear force generation in its overall dynamic range for controllability, low actuation voltage, pure piston motion to minimize aberration from lens tilting, and compensation capability for undesirable lens tilting to minimize optical aberrations. Previously, vertical comb-drive actuators with limited vertical displacements have been reported using surface micromachining for phase modulator applications [21,22]. Their maximum displacement was limited by the thickness of the polysilicon layers, which was usually less than a few micrometers. As a result, silicon-on-insulator (SOI) wafers with a significantly thicker device layer have become the preferred choice for attaining large vertical displacements [19,23]. However, those devices are limited to unidirectional actuations with high driving voltages because their comb-fingers are not electrically independent and not initially engaged.

Pre-engaged and electrically isolated vertical comb-drives are favorable to accomplish linear force control with low driving voltages. A previously reported implementation of the isolated and pre-engaged vertical comb-drives [24] addresses the above objectives, but requires multi-substrate structure bonding and transfer with inherently limited alignment between comb-fingers. Lastly, monolithic implementation of vertical actuators in a single-crystal silicon layer is desirable for repeatability and reliability of the devices.

2.1.1.3 Gimbaled 2-D Scanner

Silicon-on-insulator (SOI) micromirrors provide attractive features such as a flat mirror surface, high aspect ratio structures, CMOS compatibility, and relatively simple fabrication [25]. There have been many efforts to employ vertical comb-actuators fabricated on SOI wafers [2-4]. The high force density of a vertical comb-drive actuator enables large displacements while maintaining low voltage actuation of these high aspect

SOI structures. However, previous static scanners with SOI vertical comb-drives have been limited to single-axis, uni-directional rotation because lower comb-fingers are defined in and electrically coupled through the handle wafer [19]. For bi-directional 1-D rotation, the lower comb-fingers need to be electrically isolated.

Recently, Kwon and Milanovic developed independently and linearly controllable vertical comb-drives using only a SOI device layer, which were monolithic and isolated [13,26]. In these monolithic, isolated vertical comb-drives, both the upper and the lower comb-fingers were defined in the SOI layer and were isolated by trenches, resulting in bi-directional actuations and large static rotations [13]. This trench isolation method worked well for single axis (1-D) applications such as vertical microlens scanners [26] and 1-D micromirror [13], where either the upper or the lower comb-fingers were anchored to the substrates. Our goal was to expand this to two-axis (2-D) applications.

A gimbaled structure is a common and effective way of implementing rotation around two-axes. A two-axis micromirror has been demonstrated by gap closing actuation, which required linearization of the driving signal and decoupling of crosstalk between each dimension [27]. To implement a two-axis gimbaled micromirror without cross talk between driving voltages, vertical comb-based actuation with isolated comb-banks are desired. In the two-axis gimbaled structure with vertical combs, two orthogonal vertical comb-banks for two-axis actuation are defined in the moving gimbal. They need to be electrically isolated for independent actuation in the two axes. This requires electrical isolation as well as mechanical coupling of the isolated comb-bank and gimbal. However, trench isolation in SOI does not provide mechanical coupling. Therefore, to achieve mechanical coupling with electrical isolation, backfilling an isolation trench with an additional deposition of a dielectric layer followed by chemical mechanical polishing (CMP) has been used [28]. However, the additional deposition and CMP steps add significant complexity and cost.

2.1.1.4 Self-Aligned Vertical Comb-Drive

An optical MEMS device capable of out-of-plane torsional or piston motion is a key element in high speed and high resolution optical scanning or switching applications. This kind of device is also essential for the focal length control of a microlens in a 3-D raster scanning module for a micro confocal imaging array [29]. In particular, a micro optical component on a vertical comb-drive, using silicon on insulator (SOI) technology and deep reactive ion etching (DRIE), can be modulated with large deflection at relatively low, precise control, and fast scanning speed over the full range of the out-of-plane motion. However, the fabrication of vertical combs with a single wafer is considered a challenging task, because conventional microfabrication methods are limited to defined planar geometry.

Many efforts have been made to fabricate vertical comb-drives from the flat and smooth surface of a SOI wafer. A vertical comb-drive on two layers of single crystal silicon was first demonstrated by a bond-and-etchback process with a buried oxide pattern between two layers of single crystal silicon [19]. However, it requires not only two wafers, but also a critical alignment between the upper comb and the lower comb to generate the symmetric electrostatic field. To operate a vertical comb-drive with high

electrostatic actuation in low operating voltages, the gap between the vertical combs must be minimized by incorporating a self-aligned method.

A self-aligned vertical comb-drive has been demonstrated with a 3-step etch process with a single mask that defined both the top and bottom comb-teeth arrays [23]. Both methods have been modified with a multi-level beam SOI-MEMS process, which can provide pre-engagement between self-aligned vertical combs and bi-directional motion [30]. Another simple self-aligned fabrication of vertical comb-drive was demonstrated by using the reflow of photoresist [31]. The vertical offset mechanism of this method is based on the reflow of photoresist pattern for mechanical coupling a mirror with comb-drive. In this approach, the microfabrication and characterizations of a self-aligned vertical comb-drive using a single layer of a SOI wafer will be described.

2.1.2 VARIABLE FOCUS LIQUID LENS

Variable focus microlens arrays are useful components for optical communication, biomedical instruments, and other diverse micro-optical system applications. For example, planar optical interconnection systems require two-dimensional microlens arrays for optical parallel processors. Especially for a micromachined confocal microscope, a variable focal length lens can be the equivalent of a vertical microlens scanner, which is discussed in section 2.1.2.

Recently, reversible switchable electrowetting has been receiving increasing interest for optical and microfluidic applications [32-34]. In the electrowetting process, applying an external electric field to the solid-liquid interface modifies the wetting of a liquid droplet on a solid surface, resulting in change in the contact angle of the liquid. Electrowetting is a suitable actuating mechanism at the microscale and various applications like actuators, pumps, relays, optical switches and droplet-based reactors have been investigated [33,34].

Variable focal length is a necessary attribute in many applications of optical systems. It is also desirable to implement systems without mechanical moving parts. Many different approaches have been studied, including the uses of a pneumatically-controlled liquid lens [35] and a liquid crystal based microlens [36]. Variable focal length liquid lenses with electrowetting gradients [37] and electrochemical modification of self-assembled monolayers [38] have also been demonstrated. However the numerical apertures of these lenses are limited because the liquid lenses are immersed in another liquid solution, resulting in relatively small difference in the index of refraction. Other droplet deformation methods including electrowetting require an electrode to be placed inside a droplet [32]. The immersion of electrodes in the droplets causes severe optical distortion.

2.1.3 SURFACE ENHANCED RAMAN SPECTROSCOPY (SERS) SUBSTRATES

Raman spectroscopy is a highly-sensitive and label-free optical detection technique for biomolecules. Because it represents functional chemical bonds in molecules [39], the Raman spectrum provides an optical fingerprint of chemical and

biological molecules. It also complements infrared absorption spectroscopy, in that it has the capability to detect symmetric bonds and its spectrum is free of the background from water absorption.

Though the extremely low quantum efficiency of Raman scattering makes detection difficult, when used with the proper enhancing substrates, surface enhanced Raman scattering has a much greater fluorescence optical cross-section [40]. Enhancing substrates include colloidal metallic nanoparticles, which are widely used in solution-based chemical and biomedical analyses [41,42]. A nanoparticle self-assembly-monolayer on silicon and polymer chips has also been demonstrated as a SERS substrate [43]. However, the sample preparation of such substrates requires significant manual efforts, and thus hinders their applications on large-scale integrated biochips. The development of effective substrates would lower the detection limit of biomolecules on an integrated MEMS biochip using the micro confocal imaging array.

2.1.4 POLYMER MICROROBTICS

A polymer microrobotic platform provided a promising approach for engineering inexpensive, miniaturized, high throughput, bio-manipulation tools for 'lab-on-a-chip' applications. Moreover, SU-8 microactuators could be used to construct novel active polymer-based devices, such as mixers, valves and pumps or even mechanical cell lysing devices and cell sorters.

Electrical actuators are required for the manipulation of single molecules via a pathway that is compatible with the living environment of the cell. Electrostatic [44], thermal [45,46], shape memory alloys [47], and piezoelectric microactuators [48] cannot operate in physiological media. Their operation is typically accompanied by electrolysis, high temperatures, restricted actuation control and poor repeatability, making these types of actuators unsuitable. Electroactive polymer actuators based on ionic absorption and swelling [49,50] can operate in ionic media, but are limited to a single -out of plane-degree of freedom motion that constrains their use in most practical applications. Alternatively, isolating the actuator from the biological sample greatly restricts the extent of the possible manipulation setups [51].

Nanoscale metallic actuator structures on silicon and PDMS chips fabricated with a newly developed batch technique offer many advantages. Previously actuators have been made by Electron-beam lithography [52,53], but that fabrication method is restricted to making one actuator at a time. Fabrication techniques compatible with standard microfabrication technology are required to enable the monolithic large-scale integration of the SERS substrate on silicon or polymer-based biochips.

2.2 MICROSCALED SYSTEMS

Microscaled systems that are described include a micromachined confocal line scanner, a micromachined confocal imaging array microscope, and a miniaturized total internal reflection system.

2.2.1 MICROMACHINED CONFOCAL LINE SCANNER

A complete handheld 1-D laser scanning confocal microscope system was developed for fluorescent detection by the integration of a microfabricated pinhole, an off-the-shelf diode laser, a photodiode, and beam splitters. This system can substitute for expensive conventional confocal apparatus needed for microchannel based biochip applications and provide a solution for multiplexed bioanalytical systems such as electrophoresis, transverse isoelectrofocusing, and nanopillar-based Surface Enhanced Raman Scattering (SERS) microsystems [54]. Also this 1-D line scanning system can be easily upgraded to a complete confocal imaging system with 2-D imaging capabilities.

2.2.2 MICROMACHINED CONFOCAL IMAGING ARRAY MICROSCOPE

Conventional laser scanning confocal microscopes widely used in biological imaging and metrology are bulky bench-top instruments, and require samples to be placed in the microscope. Size reduction and portability are desired for applications such as *in vivo* imaging, planetary investigation, and handheld micro total analysis systems. A micromachined transmissive confocal microscope system and its micromachined components would achieve a dramatic reduction in the size and the cost of a confocal microscope.
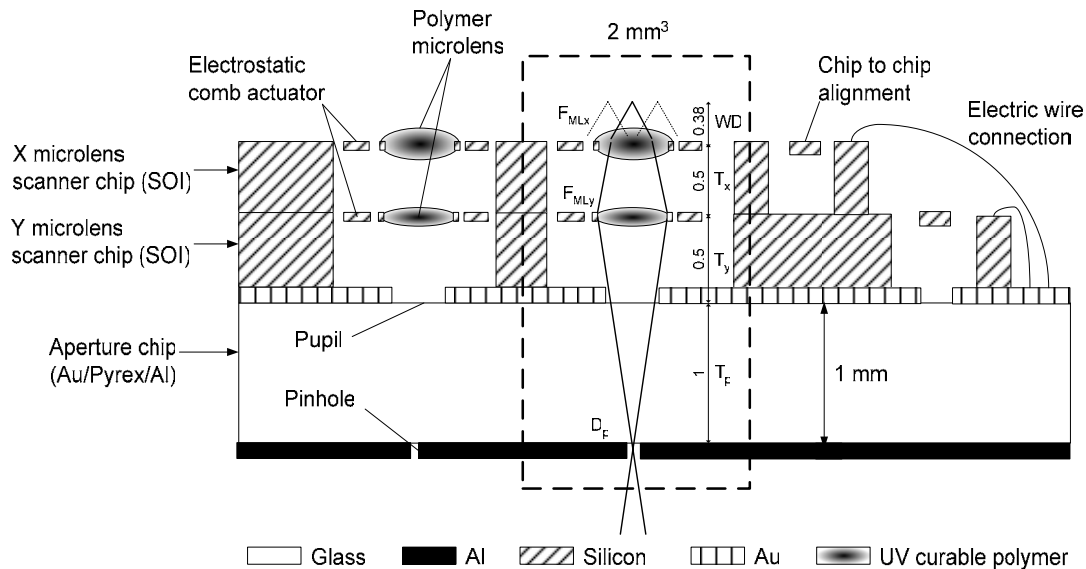
Figure 3. A side view of the device architecture of the micromachined transmissive scanning confocal microscope.

A diagram of a micromachined miniature scanning confocal microscope is presented in Figure 3. This microscope employs electrostatically-actuated microlenses for focusing and scanning. The objective lenses, scanners, a pupil, and a pinhole are also shown. Objective lenses composed of two vertically cascaded polymer microlenses are integrated with the micromachined comb-actuators. Raster scanning would be implemented by electrostatically actuating each microlens in the orthogonal directions. The necessary micromachined components for this system will be discussed.

Miniaturization of a confocal microscope required miniaturization of its components and the assembly of the miniaturized elements. Recently, notable advances toward miniaturization have been achieved in high-resolution endoscope applications by the use of micromachined components [5,55]. Fiber-optic confocal microscopes have been demonstrated using micromachined devices such as a diffractive lens plate and two orthogonal scanning micromirrors [55], or 2-D scanning micromirrors and a commercial gradient-index-lens [5]. Fiber-optic scanning confocal microscopes that use a single-

mode optical fiber for illumination and detection [56], multiple micromirrors for scanning, and a separate objective lens for focusing, have performed well in monochromatic imaging. However, this fiber-based approach is not ideal for polychromatic or fluorescent imaging due to the wavelength dependence of the fiber splitter and diffractive lenses. Also, the folded optical path caused by multiple mirror scanners requires delicate component alignment and assembly.

Transmissive scanning, which scans incident light by translating refractive lenses off the optical axis, has advantages in alignment and integration since the beam path is not folded after passing through the scanning lenses. In section 3.1.1 is described stacked 2-D microlens scanners, which achieve 2-D transmissive scanning with a straight optical path that passes through multiple substrates [29]. The microlens scanners can perform both 2-D scanning and focusing of visible light by employing cascaded refractive polymer microlenses moving in orthogonal directions. Previous microlens scanners based on photoresist-reflowed microlenses [15,16] have limited transparency in the visible spectrum. The stacked microlens scanner has optically transparent polymer microlenses, potentially making it attractive for high-resolution imaging applications. Due to its simplified beam path, reduced number of components, and design based on free space optics, this micromachined microscope can be batch fabricated, allowing integration of multiple miniaturized confocal microscopes on a chip.

The goal here is to build a miniature confocal microscope that can be batch fabricated and inexpensive, and that can be arrayed for various parallel imaging applications. This goal can be achieved by stacking microfabricated optical components in the vertical direction using transmissive scanning.

2.2.3 MINATURIZED TOTAL INTERNAL REFLECTION (MTIR) SYSTEM

Because of its unique capabilities, Total Internal Reflection Fluorescence Microscopy (TIRFM), also known as evanescent wave microscopy, has in recent year received considerable recognition. TIRFM enables the determination of surface molecular dynamics of single molecules through the detection of a thin evanescent wave at a glass/liquid interface. TIRM has been successfully utilized in detecting real time DNA surface attachment and hybridization [57, 58] and recording molecular motor activity [59].

The distinctive advantages of TIRFM in applications where confined fluorescence excitation near a solid surface is of interest, combined with the design simplicity of optical configurations employing TIR [60], have motivated the design of miniaturized evanescent excitation-based optical systems. Such systems will be of major importance in the further development of integrated advanced micro total analysis systems (µTAS's) with a capability of massive parallel processing, which can be used for high throughput screening.

Based on TIR, disposable plastic prisms integrated on biochips [61] with several different types of evanescent waveguides, including fiber [62], channel [63], and planar [64, 65] waveguides, have been proposed to address the requirements for ultra-sensitive,

high-throughput platforms. In all of these systems, the excitation laser beam comes from the side of the chip, which requires highly precise aligned at a specified angle to achieve efficient light coupling and to create a strong evanescent field. Such an optical configuration is unsuitable for the development of a fully integrated miniaturized system, since it requires the precise alignment of the tilted optical components onto a chip.

Moreover, the fabrication of high refractive index waveguides and short-period gratings requires the use of special equipment, which would in turn greatly increase the cost of the chip. Gratings and waveguides also suffer from light coupling and propagation losses. These limitations can only be overcome with the use of bulky, high power, expensive lasers. Plastic prisms, on the other hand, can be inexpensively fabricated, but their use in an array-type format for high throughput processing is still questionable.

2.2.4 SELF-ALIGNED INTEGRATED MICROFLUIDIC OPTICAL SYSTEM (SI-MOS)

Micro-total analysis systems (μTAS) [66] have been developed to not only miniaturize the TAS system, but also to enhance its performance as a total analysis system. The techniques of micromachining [67, 68] have served in this development. The components of micrometer size are integrated together for different functions. Recently, micro-optical components such as microlenses [69-71], waveguides [72-74], and detectors [75,76] have been used to accomplish laser-induced fluorescence detection (LIF) in analytical microchips and a μTAS, resulting in increased detection limits compared to other conventional detection methods [77-80].

Light emitting diodes (LED's) have also been recognized as low-cost excitation sources for fluorescence excitation [81, 82]. The vertical microlenses [83] and planar microlenses [81] have been integrated with microfluidic channels to couple excitation light to the channels.

3. DESIGN

The designs of the micro-scaled confocal imaging array, the miniaturized total internal reflection system, the self-aligned integrated microfluidic optical system, the SERS substrates, and the polymer microrobotic system for single cell manipulation are presented in this chapter.

3.1 SYSTEMS COMPONENTS

Several microcomponents required for these microfluidic systems needed to be developed and fabricated. These components included micromachined scanners, vertical variable focus liquid lenses, Surface enhanced Raman Spectroscopy substrates, and polymer microrobotics.

3.1.1 MICROMACHINED SCANNERS

The designs of the micromachined scanners that are included here are for stacked 2-dimensional microlens scanners, vertical microlenses, gimbaled 2-dimensional scanners and self-aligned vertical comb-drives.

3.1.1.1 Stacked 2-Dimensional Microlens Scanners

A unique cascading approach to implement 2-D transmissive scanning via the vertical stacking of independent 1-D microlens scanners is described.

3.1.1.1.1 Transmissive Scanning

A lens moving transverse to the optical axis changes the propagation direction of incident light and shifts the focal spot. A ray optic illustration of the 1-D transmissive scanning principle is shown in Figure 4, where Δy_1, f, Δy_p, θ, and M represent the lens displacement, lens focal length, image displacement, scan angle, and absolute value of transverse magnification, respectively.

The transverse lens translocation of Δy_l causes translocation of the image Δy_p with the relationship of :

$$\Delta y_p = (1+M)\Delta y_i \qquad (1)$$

for a finite conjugate system, as presented in Figure 4(a). For the infinite conjugate system shown in Fig 4(b), M is zero, so that Δy_p is simply equal to Δy_l. In both cases, the scanning angle is determined by the lens focal length and lens displacement, with the relationship of:

$$\theta = \tan^{-1}(\frac{\Delta y_l}{f}) \quad . \qquad (2)$$

In this simple ray optic illustration, a large displacement of the lens with a short focal length is desired for large scanning angles. Another difference from mirror scanners is that the scanning angle can be increased without increasing the actuator displacement by decreasing the focal length of the lens. If one more lens is cascaded and actuated in the orthogonal direction with the first lens, 2-D scanning of the image can be easily achieved. To implement transmissive scanning in micro-scale, the microlens and microactuator need to be integrated as one device, which is called a microlens scanner.

(a)

$\Delta y_p = (1+M) \Delta y_l$

Δy_l

$\theta = \tan^{-1}(\frac{\Delta y}{f})$

Point source

Image

Lens

y: lens displacement
M : magnification

(b)

Δy_l

$\Delta y_p = \Delta y_l$

f
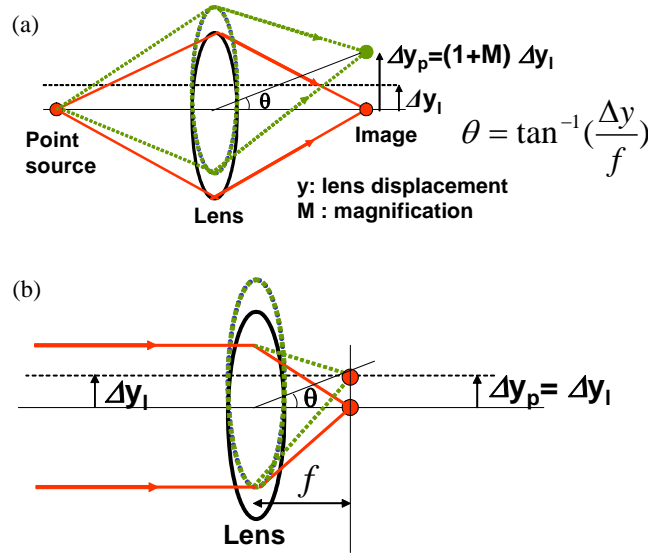
Lens

Figure 4. Ray optic illustration of transmissive scanning lenses: (a) finite conjugate system and (b) infinite conjugate system.

3.1.1.1.2 Stacked 2-D Microlens Scanners

The described transmissive scanning is implemented by cascading electrostatically actuated polymer microlenses as shown in the schematic diagram Figure 5. A stacked 2-D microlens scanner consists of two vertically stacked 1-D microlens scanners. A 1-D microlens scanner, a polymer microlens fabricated on a lateral electrostatic comb-drive actuator, is the basic unit to actuate the polymer microlens in one direction.
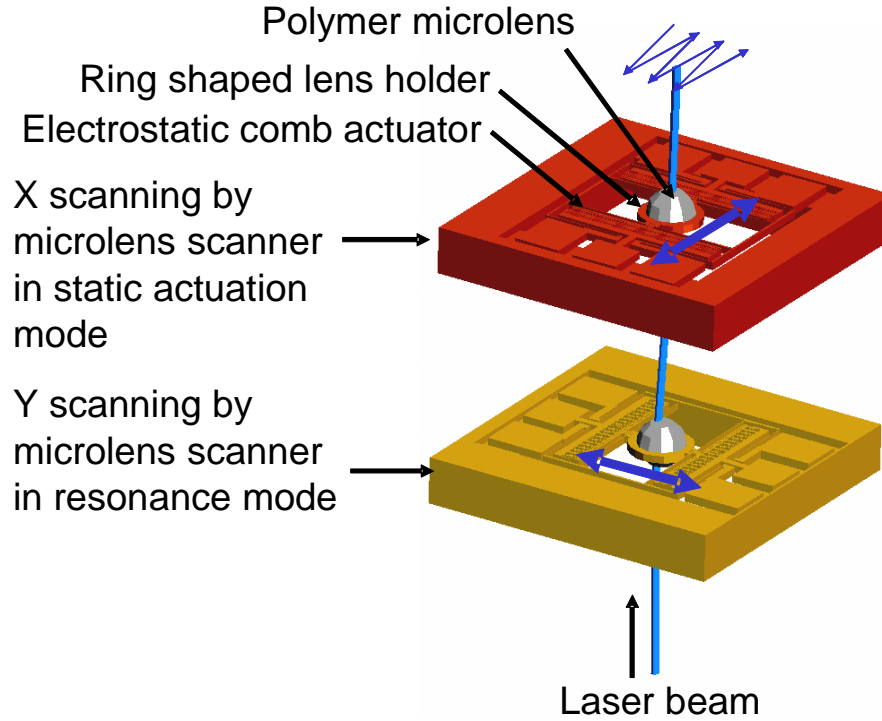
Figure 5. Conceptual diagram of a stacked 2-D microlens scanner.

The 1-D microlens scanner has two identical comb-drives connected to a ring shaped lens-holder designed to hold a droplet of liquid polymer during its fabrication step. The substrate under the lens and actuator are then removed to form an optical window. The two independent 1-D scanners share the same optical axis through the optical window and actuate two microlenses in orthogonal directions. Therefore, light passing through the two lenses can be focused and steered in 2-D within 1 mm of optical path length, which is designed to be twice the substrate thickness. Raster scanning can be easily achieved by actuating the two microlens scanner with different scanning speed. The Y microlens scanner is designed for a fast resonance frequency and operated in the resonance mode, which will result in it having a high line scanning speed. The X microlens scanner on the bottom is designed for large displacements, and will operate in an off-resonance mode. The actuation frequency of X microlens scanner, the frame rate, can be operated at an arbitrary frequency below its resonance frequency. In this way, raster scanning can be achieved with a large number of horizontal lines in one frame.

This integration scheme has several advantages. Since integration is simply the assembly of independent microlens scanners, vertical stacking and transmissive scanning allow modular development, testing, and integration of each component. Secondly, the optical alignment issues required in 2-D raster scanning are simplified. In a reflective scanner using micromirrors, the optical axis is folded at every mirror surface, and alignment between the mirrors and external lenses requires alignment in 3-D space. In cascading transmissive scanning, however, the alignment is simply the alignment in plane between the two microlens scanners, which is the conventional alignment method for integrated circuit (IC) fabrication and lithography. Thirdly, there will be less mechanical crosstalk than with a single lens 2-D scanner, since x scanning and y scanning are

15

performed on different chips. A potentially higher scanning speed can be expected since the masses of the microlenses in the resonating microlens scanners can be smaller than that of a single lens 2-D scanner, resulting in higher resonance frequencies. Also, in many cases a large number of optical surfaces can give more design freedom.

3.1.1.1.3 Design Parameters of Stacked 2-D Microlens Scanners

Design of the stacked microlens scanners includes the mechanical designs of microlens scanners and the optical system. Resonant frequency and maximum displacement of the actuator are major mechanical design parameters that determine the scanning speed and the scanning range. Optical system designs can be tailored for particular applications. The design parameters of a stacked microlens scanner are presented.

For the stacked 2-D microlens scanner design of Figure 5 for high-speed raster scanners, the resonance frequencies of the Y microlens scanner and maximum displacement of X microlens scanner are the main design goals. These parameters are mainly controlled by changing the dimensions of the folded flexures based on the conventional comb-drive design process [84]. The resonant frequency of the microlens scanner from a simple damped harmonic oscillator model with folded spring is determined by:

$$f_0 = \left(\frac{2Ehb^3}{ML^3} \right)^{1/2}$$
(3)

where f_0, E, h, b, M, and L denote the resonance frequency of microlens scanner, the Young's modulus of single crystal silicon, the device layer thickness of SOI, the beam width of the folded flexure, and the beam length of the flexure, respectively. The maximum displacement of the microlens scanner is designed by considering degradation of electrostatic stability from non-linear spring constant [85]. The maximum displacement before side pull-in (y_{SI}) is:

$$y_{SI} = d\sqrt{\frac{k_{side}}{2k_y}} - \frac{y_0}{2} = d\sqrt{\frac{k_x}{2k_y}\left(\frac{3}{8}\left(\frac{x}{b}\right)^2 + 1\right)^{-1}} - \frac{y_0}{2} \approx d\frac{L}{x} - \frac{y_0}{2}$$
(4)

where d, k_{side}, k_y, k_x, y_0, and x indicate the gap between the comb-fingers, the deflection dependant non-linear spring constant, the spring constant in actuation direction, the spring constant in the side pull-in direction, the initial overlap of the comb-fingers, and the desired maximum displacement, respectively. This simplified expression is acquired by substituting the deflection dependant non-linear spring constant [86] for the pull-in displacement [87]. From this equation, the width and length of flexures can be determined for specific resonance frequencies and maximum displacements. Setting d, h, and y_0 at 2 μm, 20μm, and 5μm, respectively, and the microlens flexure widths of $b = 4$

16

μm, 8 μm, and 12 μm, a range of resonance frequencies is obtained. The length of flexure was set to 500 μm for the fast resonating microlens scanner, and to 800 μm for microlens actuator actuated in the off-resonance mode with the large static displacement.
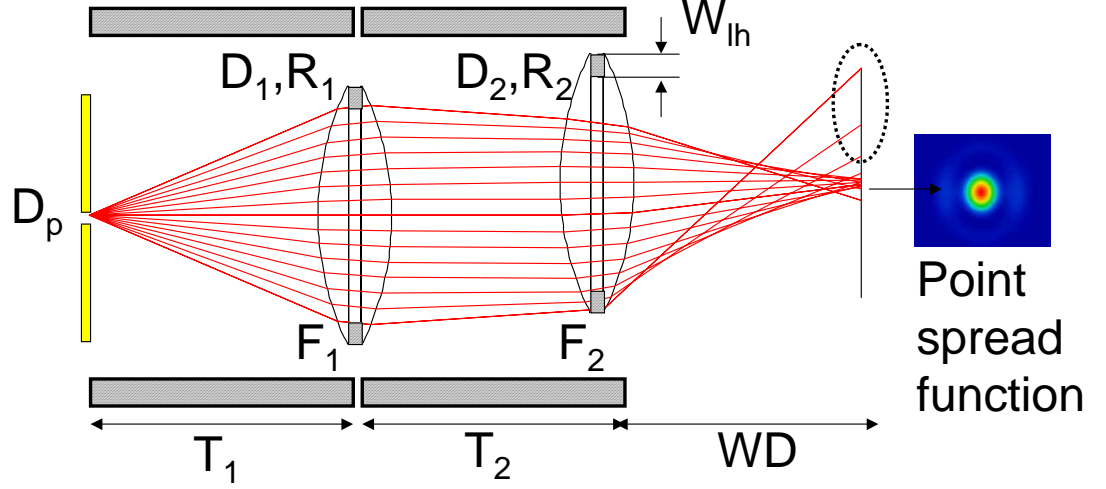
Figure 6. The optical design parameters of a stacked 2-D microlens scanner.

Figure 6 illustrates the optical design parameters of a stacked 2-D microlens scanner for a finite conjugate system. A pinhole with a diameter of D_p is the point light source. T_1, T_2 and WD denote the distance between the pinhole and the first lens, the distance between the two lenses, and the working distance. R, D, F, and W_{lh} represent the radius of curvature, the outer diameter, the focal length, and the lens holder width, respectively. Subscript numbers 1 and 2 indicate the Y and the X microlens scanner, respectively. The exact determination of these parameters depends on the specific applications and the required specifications. This 2-D scanner is designed for a miniaturized microscope system that had the major design considerations of high imaging resolution and a large field of view. We set T_1, T_2, F_1, F_2, and D as 1500μm, 500μm, 1000μm, 500μm, and 500μm, respectively, for the microscope system. Having a microlens with a larger focal length will reduce the mass of Y microlens scanner, resulting in a higher resonance frequency.

3.1.1.2 Vertical Microlens

The pre-engaged, isolated vertical comb-banks were to be fabricated in a monolithic SOI layer. This design enabled the bidirectional, low voltage, large displacement, and linear actuation of the microlens with unique coupled torsion flexures. These isolated comb-banks make it possible to compensate for slight lens tilting due to variations in fabrication, as well as to actuate both upwards and downwards movement, thereby doubling the total static scanning range.

Large vertical displacement microlens scanners require low (< 10 Volts) actuation voltage based on silicon-on-insulator (SOI) technology. The uniquely isolated and pre-engaged vertical comb-drive sets and coupled-torsion flexure designs provide both upward and downward piston motions using low driving voltages.

3.1.1.3 Gimbaled 2-D Scanner

A backside island isolation method for SOI MEMS technologies and a vertical comb-drive based 2-D gimbaled micromirrors with large static rotation using the isolation method are introduced. This design of this isolation method provided electrical isolation and mechanical coupling of SOI structures without additional dielectric backfill and planarization.

The backside island is a hidden layer beneath the gimbal designed to allow the independent application of actuation potentials to the gimbal and inner mirror. The fabrication process of the backside island isolation structures was designed for integration into an established vertical comb-drive process, thereby allowing implementation of two-axis gimbaled structures. The maximum static optical deflections of the gimbal and mirror were designed to be 46° and 15°, respectively.

3.1.1.3.1   Design of the Two-Axis Gimaled Micromirror

The designs of the two-axis gimbaled micromirror and the cross section of the required beams are shown in Figures 7 and 8, respectively. The 2-D gimbaled mirror design was based on two unique features: the vertical comb-drives for actuation and the backside island isolation for coupling, as shown in Figure 7. In this design, the micromirror and gimbal were independently actuated by separate vertical comb-drives. The independent actuation was achieved by selectively activating separate vertical comb-drive banks (V_1-V_5) in the gimbal and mirror. The gimbal axis utilized four isolated comb-drive banks on each side of the rotation axis to achieve bi-directional rotation about the gimbal axis. For example, by actuating electrodes V_1 and V_2, rotation in 'positive' direction was achieved, since the comb-drive bank with electrode V_1 pulled the gimbal structure down, while the comb-drive bank with electrode V_2 pulled the gimbal structure up. Thus, 'pure' torque was applied on the suspension beams. To achieve rotation in the opposite direction, electrodes V_3 and V_4 were activated. In all of these cases, the reference ground signal (*GND*) was applied to the entire gimbal through the right side torsion flexure. To achieve rotation of the mirror axis, two independent potentials to the comb-drive banks along that axis were required. Without the present isolation technology, this would not be achievable. Namely, the gimbal was grounded (*GND*) through the right torsion flexure of the gimbal, whereas the potential of mirror (V_5) was applied through the left torsion flexure of the gimbal. At the same time, the gimbal and mirror needed to be mechanically coupled. The isolated coupling was achieved by a backside island below the gimbal structure, as shown in the dashed rectangle in Figure 8. Note that the design of the backside island connected the full thickness SOI beams that were at different potentials. The insulating buried oxide was sandwiched between the SOI layer and the backside island.
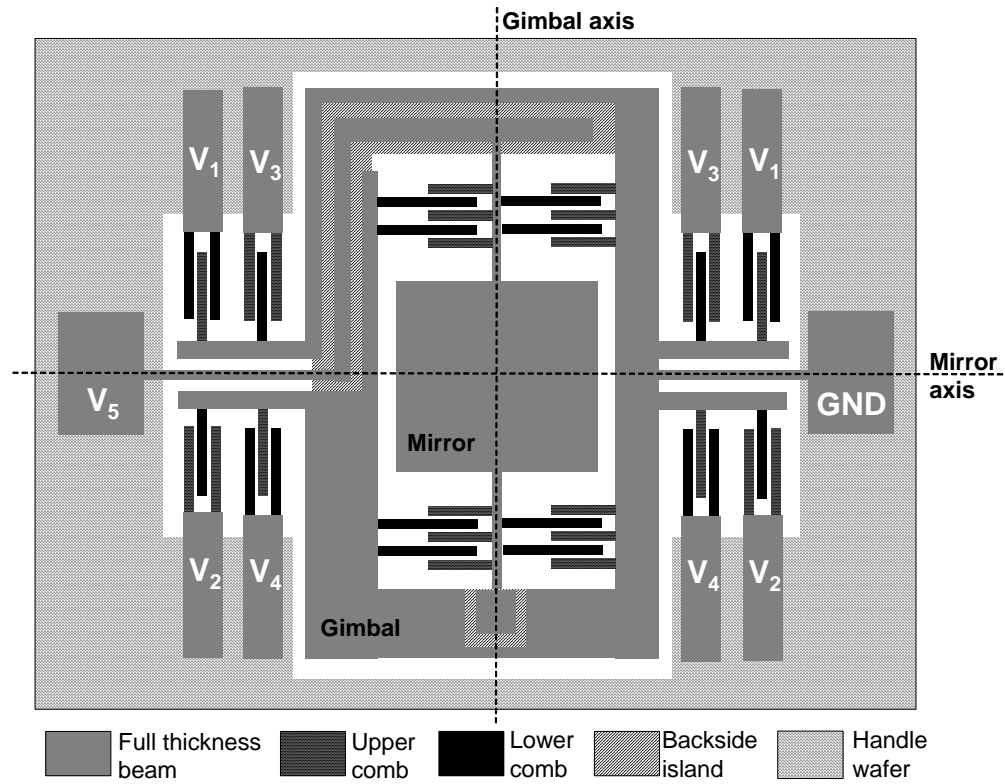
Figure 7. Top view of a two-axis gimbaled micromirror based on backside island isolation and vertical comb-drives.
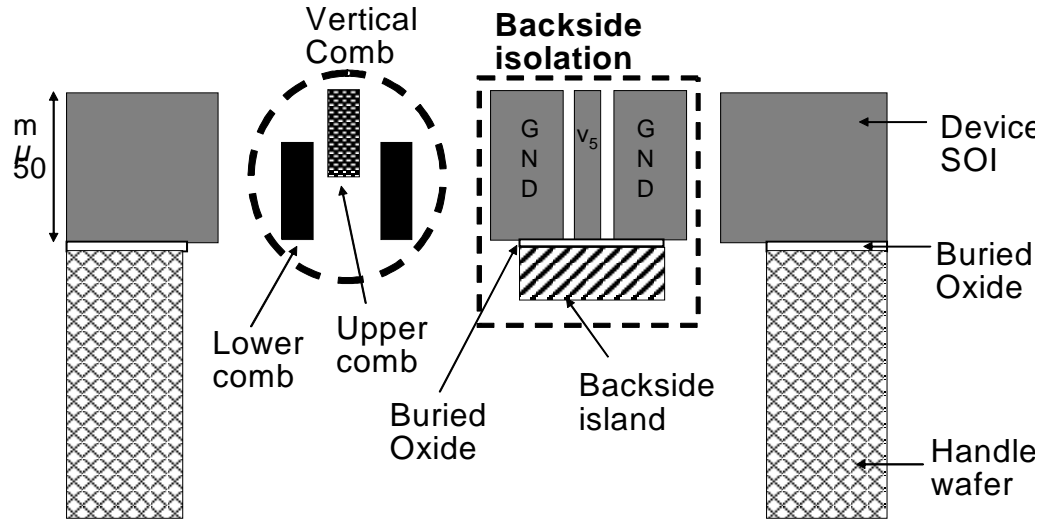
Figure 8. Cross sectional view of a vertical comb-drive and its backside island.

3.1.1.3.2   Concept of the Backside Island

The backside island is designed as a silicon island located under the SOI device layer formed from a timed etch of the handle wafer. The backside island mechanically connects the trench-isolated structures in the SOI, but allows for the electrical isolation, as the buried oxide layer is sandwiched between the island and SOI structures. In this way, the mirror and gimbal can be mechanically coupled while maintaining electrical isolation without having to refill the dielectric in the isolation trenches.

3.1.2 VARIABLE FOCUS LIQUID LENS

Microfabricated Planar Electrodes-based Liquid Lens (µPELL), a variable focal length liquid lens based on electrowetting, is described. Control of the focal length of liquid lenses is achieved by electrically-modulating the contact angle of a liquid droplet on a solid surface. Microfabricated planar electrodes enable the control of a liquid droplet shape without physical contact between the electrodes and the liquid droplet. This enables the elimination of invasive electrodes, which is an obstacle to electrowetting liquid lenses. Focal length control through µPELL is designed to have more than 30% variability of its original focal length and a response time of 100ms. This new variable focal length liquid lens implements the reversible electrowetting without physical contact between the electrodes and the liquid lens.

3.1.2.1 CONVENTIONAL ELECTROWETTING USING INVASIVE ELECTRODES

Figure 9 shows a basic concept of electrowetting with an invasive electrode. When it is assumed that the movement of the surface charge in a droplet is sufficient for conduction, and in the presence of an applied voltage, the electrolyte and the ground electrode form a parallel plate capacitor. This is a valid approximation for applied voltage frequencies below 1MHz [34].
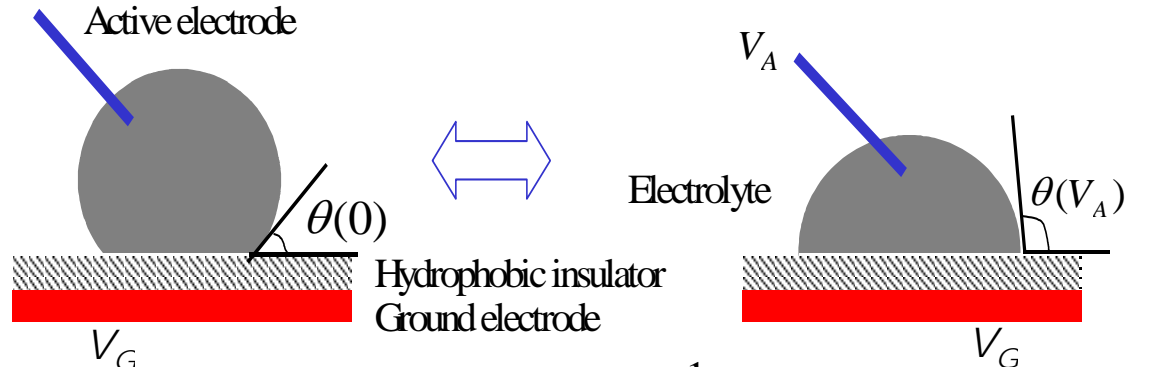
Figure 9. Electrowetting using an invasive electrode.

Under this assumption, the relationship between the contact angle of the droplet θ and the applied potential V_A is shown in Eq. (5). V_A, d, ε and γ_{LV} are the applied voltage, the thickness of insulation layer, the dielectric constant of the insulating layer, and the interfacial tension between liquid and vapor, respectively [32].

$$\cos[\theta(V_A)] = \cos[\theta(0)] \ + \ \frac{1}{2}\frac{\varepsilon}{d\gamma_{LV}}V_A^{\ 2} \tag{5}$$

Electrowetting can be thought of as controlling the surface energy of the liquid-solid interface. The surface tension of the liquid will make the shape of the droplet such that the total surface energy is minimized. The focal length droplet of a liquid lens can be controlled electrically. However, invasive top electrodes would cause severe distortions of a liquid lens' shape, which has hindered the development of droplets to be used as lenses.

3.1.2.2 ELECTROWETTING USING NON-INVASIVE PLANAR ELECTRODES

The main concept of how to implement a liquid droplet lens without distortion is through patterning the ground electrode at the bottom of the droplet, as shown in Figure 10. In this design the invasive electrode was replaced with a new transparent patterned electrode.
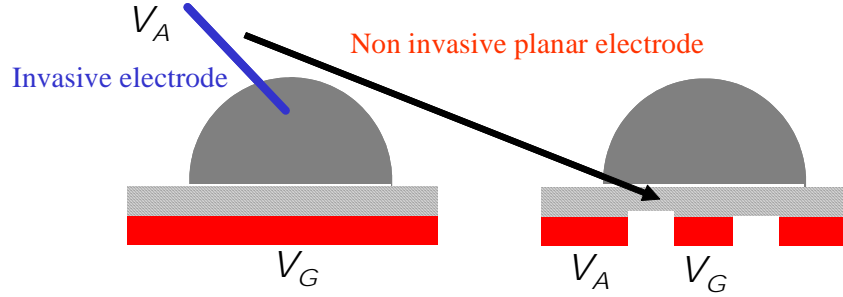
Figure 10. The concept of a non invasive planar electrode.

The design of a μPELL, which is presented in Figure 11(a), illustrates two different capacitors C_A and C_G, which represent the capacitance between the droplet and active electrode and the capacitance between the droplet and ground electrode, respectively, with an equipotential droplet surface. The bottom ground electrode was patterned and actuation voltage was applied between the ground electrode in the center of the droplet and the active electrode in the edge of the droplet.
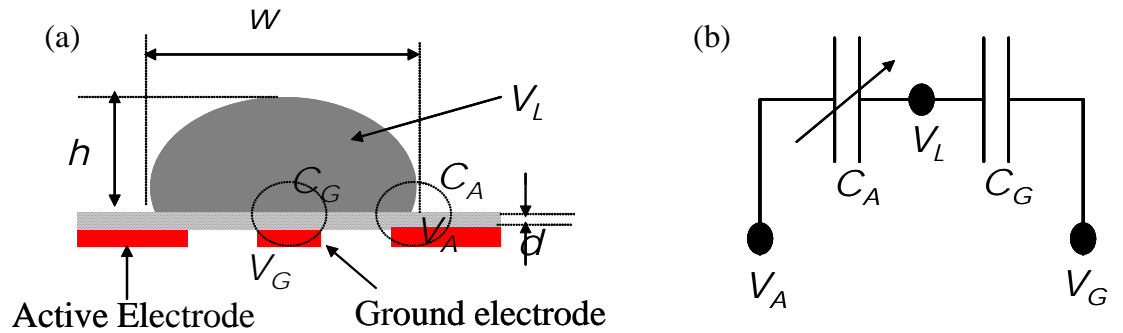
Figure 11. (a) Schematic diagram of a non-invasive planar electrode (b) Equivalent circuit model of the μPELL.

Potentials at the active electrode, ground electrode, and liquid droplet were V_A, V_G and V_L, respectively. The height and width of the liquid lens were represented by h and w. By considering Eq. (5) and a constant liquid droplet volume condition, C_A varied as the contact angle of the liquid droplet was modulated by the applied voltage.

The modified electrowetting scheme can be represented by two capacitors in series (Figure 11 (b)), one of which is a variable capacitor. The applied voltage will decrease the contact angle, which in turn will cause an increase in width w under a constant volume condition. Unlike the invasive electrode method shown in Figure 9, the potential of the liquid lens, V_L, is a function of the applied voltage, V_A. V_L is then represented by Eq. (6), in which the potential of the liquid lens is initially V_G, and increases as C_A becomes larger, caused by a decreasing contact angle.

$$V_L = \frac{C_A V_A + C_G V_G}{C_A + C_G}$$
(6)

Since the potential of the droplet is no longer a constant, Eq. (3) can be modified by substituting V_A with $(V_A - V_L)$ into it, resulting in Eq. (5).

$$\cos[\theta(V_A)] = \cos[\theta(0)] + \frac{1}{2}\frac{\varepsilon}{d\gamma_{LV}}(V_A - V_L)^2$$
(7)

Considering Eq. (6) and Eq. (7), it is expected that the change in the contact angle of the liquid droplet will become saturated as the change in contact angle C_A increases, resulting in an increase of V_L.

3.1.2.3 SIMULATION OF DROPLET SHAPE USING SURFACE EVOLVER

To test the feasibility of using a liquid droplet as a variable focus lens, the change in droplet shape was simulated using the public domain program Surface Evolver [88]. The simulation was carried out by varying the contact angle under the conditions of normal gravity and a 1 µl water droplet. The first step was to calculate the contact angle of the droplet at the given voltage using Eq. (7). The Perform droplet shape simulations were performed using the Surface Evolver, and the results of the simulations are presented in Figure 12. The contact angles were 110°, 100°, 90° and 80°. The droplet dimensions were determined by measuring the widths and heights of the droplet deformation results. The approximate effective focal lengths were calculated using Eq. (8), and the relationships between the contact angles and the actuation voltages were determined.

$$f = \frac{r}{\Delta n} = \frac{1}{n_{water} - n_{air}}\left[\left(\frac{w}{2}\right)^2 + h^2\right]$$
(8)

Significant changes in droplet shapes, which are directly related with the change in optical power, were observed. Figure 13 shows the calculated inverse focal

lengths with respect to the contact angles. The inverse focal length varied approximately linearly with contact angles from 70° to 110°, which is the range of operation of the developed liquid lens. The calculated inverse focal length variations ranged from 345D to 470D, showing that the droplet lens can have very high power as it undergoes more than a 30% variability of its original focal length. Using the previous contact angle model and the droplet deformation simulation, the relationship between applied voltage and focal length can be predicted by solving the combined equations (6), (7) and (8) with the results from the Surface Evolver simulation.
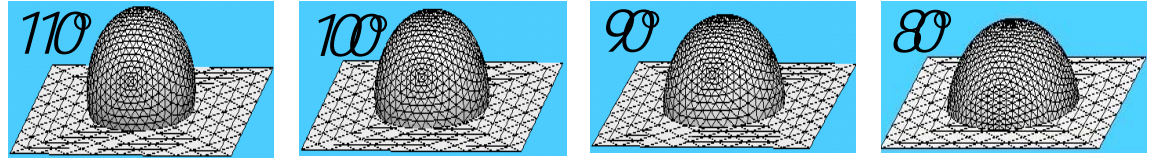
Figure 12. Droplet shape simulations with respect to a contact angle using Surface Evolver.
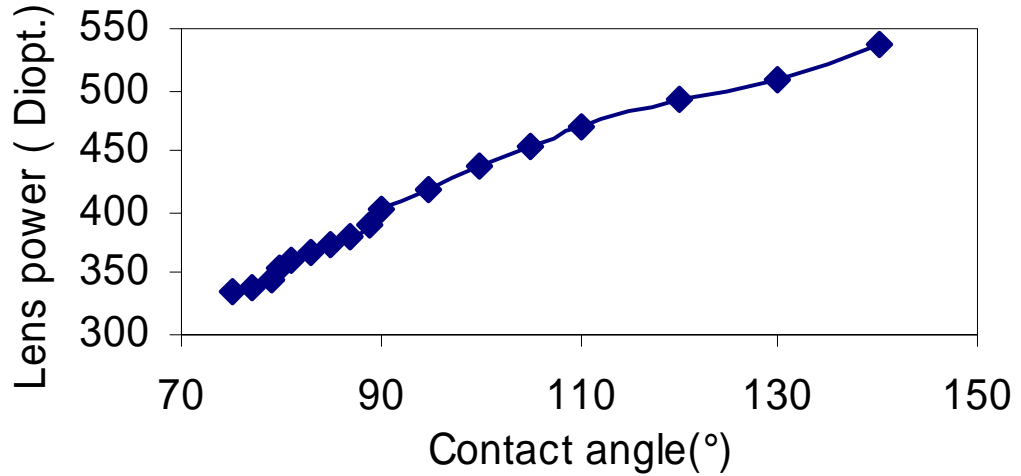
Figure 13. Calculated lens optical power with respect to the contact angle of the droplet.

The Surface Evolver does not have a model for the direct simulation of electrowetting. The previous electrowetting-on-dielectric simulation relied on the Lippmann-Young equation (Eq.(5)) to extract contact angle information from the applied voltage, and then a visual representation of the droplet shape was yielded by Surface Evolver. An electrowetting model was developed by adding an electrostatic energy term in the total surface energy function of the Surface Evolver. This enabled a direct simulation of the droplet profile change with the Surface Evolver by inputting an applied voltage.

All of the surface energy terms in Surface Evolver are described in the form of line integrals. Therefore, to implement an electrowetting model in the Surface Evolver, the electrostatic energy term in line integral needed to be added to the total surface energy. A potential V is applied to the conducting liquid, and the electrostatic energy from the induced electric field across the dielectric is described in Eq. (9), which was then integrated to become Eq. (10).

$$\frac{dU}{dA} = \int_0^t \frac{1}{2} \vec{E} \vec{D} dz \tag{9}$$

$$\frac{dU}{dA} = \frac{1}{2} t \vec{E} \vec{D} = \frac{1}{2} \frac{\varepsilon_0 \varepsilon}{t} V^2 \tag{10}$$

The dielectric layer thickness, the charge displacement, the free space permittivity and the dielectric constant are represented by t, D, ε_0, and ε, respectively. At the solid-liquid interface, the electrostatic energy contribution can be obtained by integrating the electrostatic energy over the interfacial surface (Eq. (11)). The equivalent edge integral form was rewritten for implementation in Surface Evolver (Eq. (12)).

$$E = \iint_{SL} \frac{\varepsilon_0 \varepsilon}{2t} V^2 \vec{k} d\vec{A} \tag{11}$$

$$E = \int_{\partial(SL)} \frac{\varepsilon_0 \varepsilon}{2t} V^2 y \vec{i} \, d\vec{l} \tag{12}$$

SL denotes the solid-liquid interface and E represents the electrostatic interfacial energy. In the Surface Evolver the user defines an initial surface shape, in this case, a cube, and the program will iterate and move the vertices of surface in the direction of a minimized energy under specific constraints. The gravity field and the surface energies of the solid-liquid, solid-gas, and liquid-gas interfaces, which determine the initial contact angel, are taken into account. To incorporate the electrostatic energy contribution, Eq. (12) is prescribed onto the four edges of the cube. The resulting droplet shape simulation

using the electrowetting model is shown in Figure 14. The simulation results agreed with the simulation based on the Lippmann-Young equation.
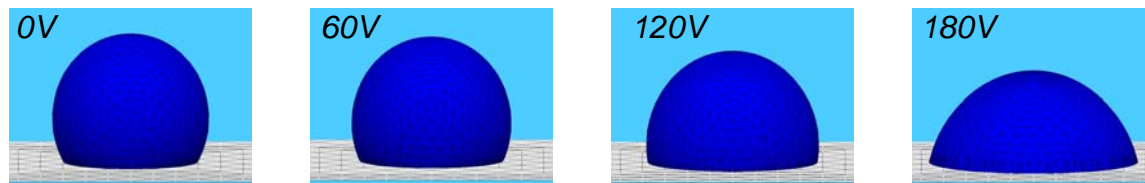
Figure 14.   Droplet shape simulation using the developed electrowetting model in the Surface Evolver.

3.1.3 SURFACE ENHANCED RAMAN SPECTROSCOPY (SERS) SUBSTRATES

Nanoscale metallic pillar structures on silicon and well structures on PDMS chips were developed with a novel batch fabrication technique. The average density and size of the nanopillar and nanowell structures were controlled in the fabrication, and the on-chip Surface Enhanced Raman Spectroscopy (SERS) substrate made by this fabrication technique was compatible with standard microfabrication technology.   This enabled the monolithic large-scale integration of the SERS substrate on silicon or polymer-based biochips for multiplexing high-throughput biomolecule detections. The enhancement factor of Raman scattering signal was projected to be 1000 times higher than the ordinary metallic films.   A SERS substrate with associated microcomponents is presented in Figure 15.
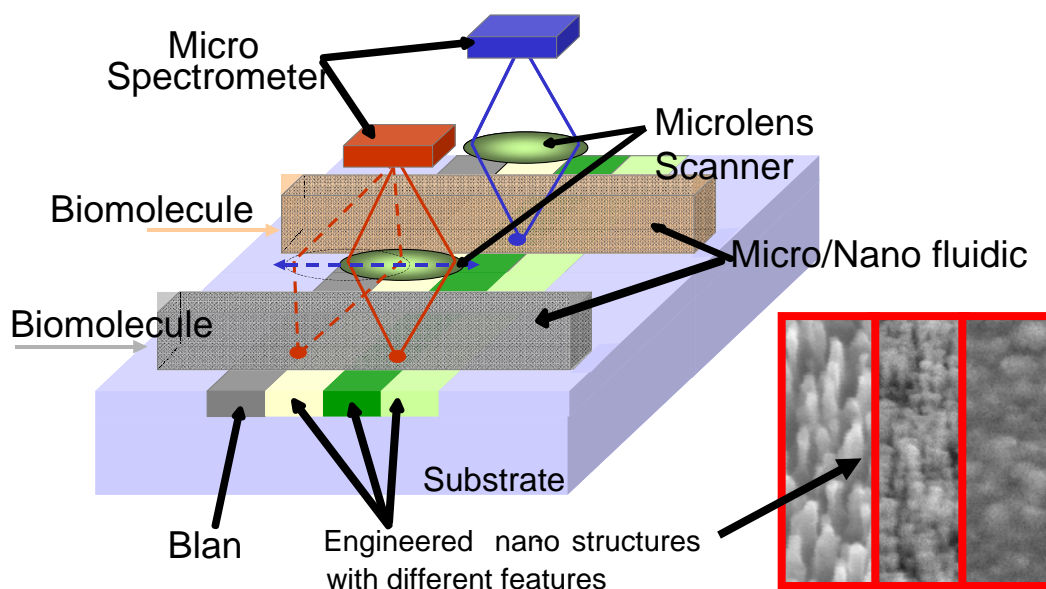
Figure 15. Schematic diagram of a SERS on-chip system.

3.1.4 POLYMER MICROROBTIC WORKSTATION PLATFORM

A microfabricated polymer microrobotic workstation-platform was required to position and exert mechanical forces on single cells. The workstation needed to include a three degrees of freedom microrobotic arm and a pushing beam with a sharp tip at its end that could mechanically stimulate a target cell. Two types of actuators, a chevron and hot-and-cold-arm, were designed to open and locate in two-dimensional space the gripper of the microrobotic platform and to move the pushing beam.

The hot-and-cold-arm actuator needed to be activated by passing a current through a metal resistor-heater. In a conventional hot-and-cold-arm actuator, the current enters the hot arm and exits at the cold arm side. In the design of this hot-and-cold-arm actuator, a separate lithographic step would define the metal resistor, and its dimensions would be different than the dimensions of the organic structure (SU-8). This feature is extremely important for achieving high performance hot-and-cold-arm actuators. It allowed the patterning of a U-shape heating element on only the hot arm (Figure 16). When electric current enters and exits the hot arm, heat is not generated on the cold arm and the flexure, and the temperature difference between the hot arm and the cold arm is thus maximized. That concept was used to design the actuators of the gripper of the microrobotic platform (Figure 17). An ANSYS model of the microrobotic arm was constructed to illustrate the amplification mechanism (Figure 18).
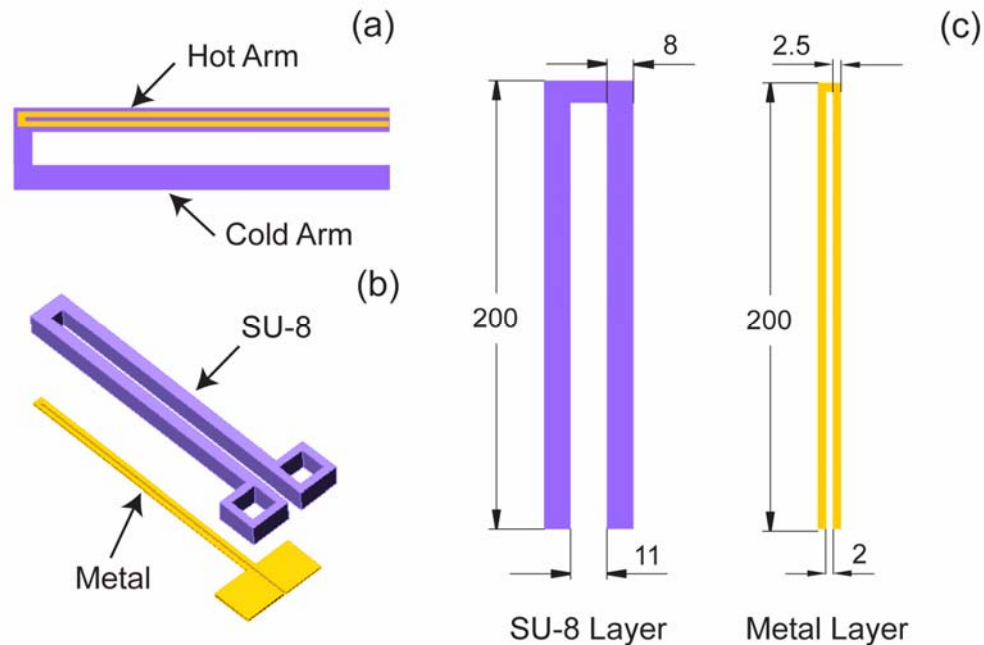
Figure 16. (a) Top view of the modified hot-and-cold arm actuator where the metal resistor is patterned on only one side, (b) Three dimensional view showing the two-layer structure, and (c) Typical dimensions of each layer (in μm).
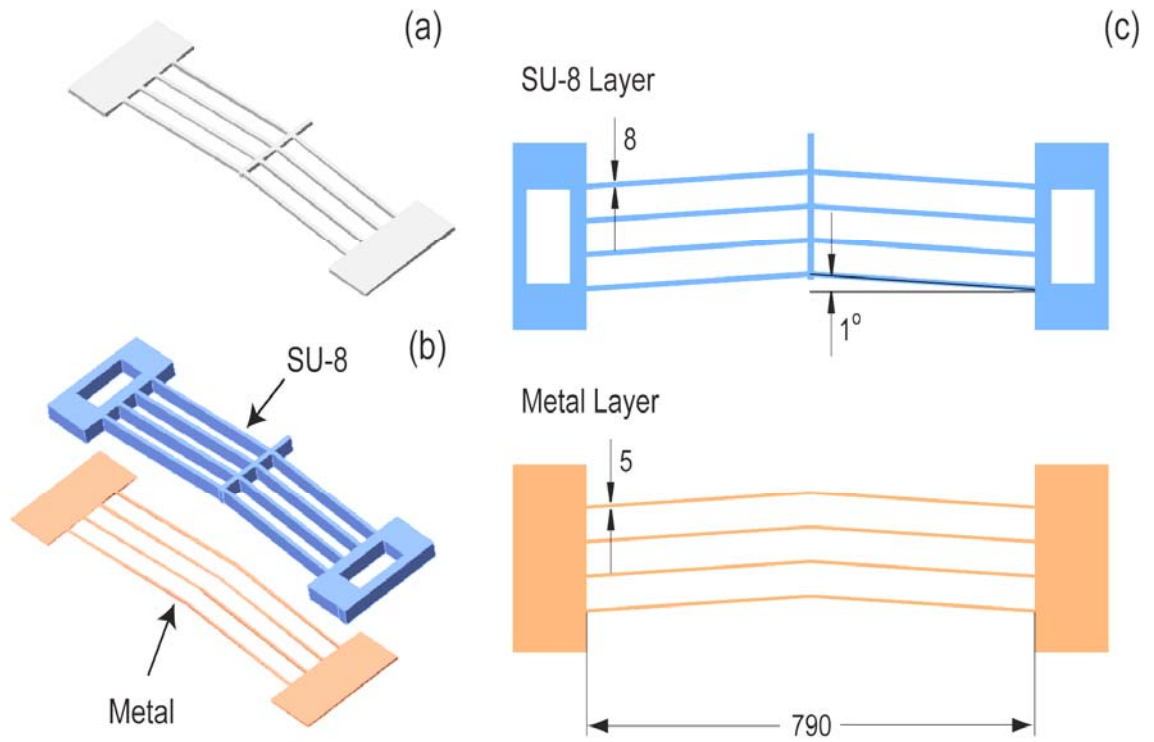
Figure 17. (a) A conventional one-layer chevron actuator (typically made from silicon), (b) The proposed SU-8 based actuator consisting of two layers, and (c) Typical dimensions of each layer (in μm).
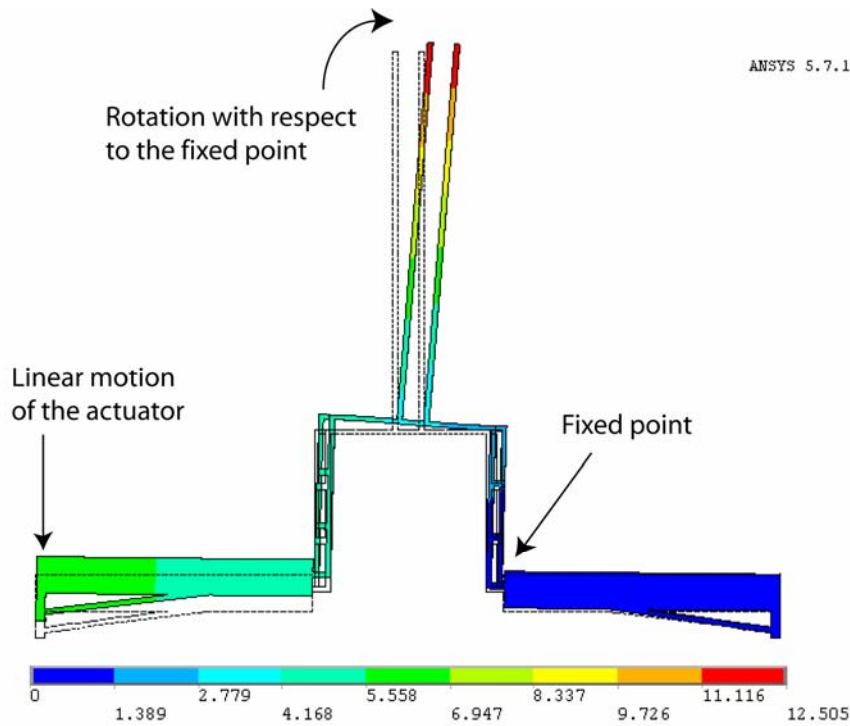
Figure 18. Mechanics of the microrobotic arm.

3.2 MICROSCALED SYSTEMS

The designed microscaled systems included a micromachined confocal line scanner, and microscaled confocal imaging array microscope, a miniaturized total internal reflection system, and a self-aligned integrated microfluidic optical system.

3.2.1 MICROMACHINED CONFOCAL LINE SCANNER

The laser confocal line scanning system was essentially a miniaturized laser scanning confocal microscope operating in x-y scanning mode, as shown in Figure 19(a). A laser confocal excitation and detection scheme was implemented using a microfabricated 1-D scanning microlens and pinhole (dashed box) together with off-the-shelf components. A collimated laser light from a laser diode (633 nm) was focused on a 20 µm confocal pinhole (P) through a beam splitter and collection lens. The confocal pinhole was imaged by the microlens in the MEMS microlens scanner onto the microfluidic channels with a magnification of 0.2, which made a roughly 4 µm excitation spot on the sample. System transverse resolution was better than 4 µm since the pinhole was larger than the Airy disk diameter of the collection lens.

The excitation spot was scanned over multiple microfluidic channels fabricated in PDMS and the emitted fluorescent signals from different microfluidic channels passed the confocal pinhole again and was directed back to the photodiode by a collection lens

through the beam splitter. Because the spot size for excitation and detection was smaller than the width of the channel, fluorescent signals from the different microfluidic channels were detected using a detection system. This multiplexed detection capability with small detection volume is of importance because it can use densely packed microfluidic channels for high throughput applications. Figure 19 (b) shows line scanning of the confocal illumination spot by the electrostatic translation of microlens at 1.16 kHz.
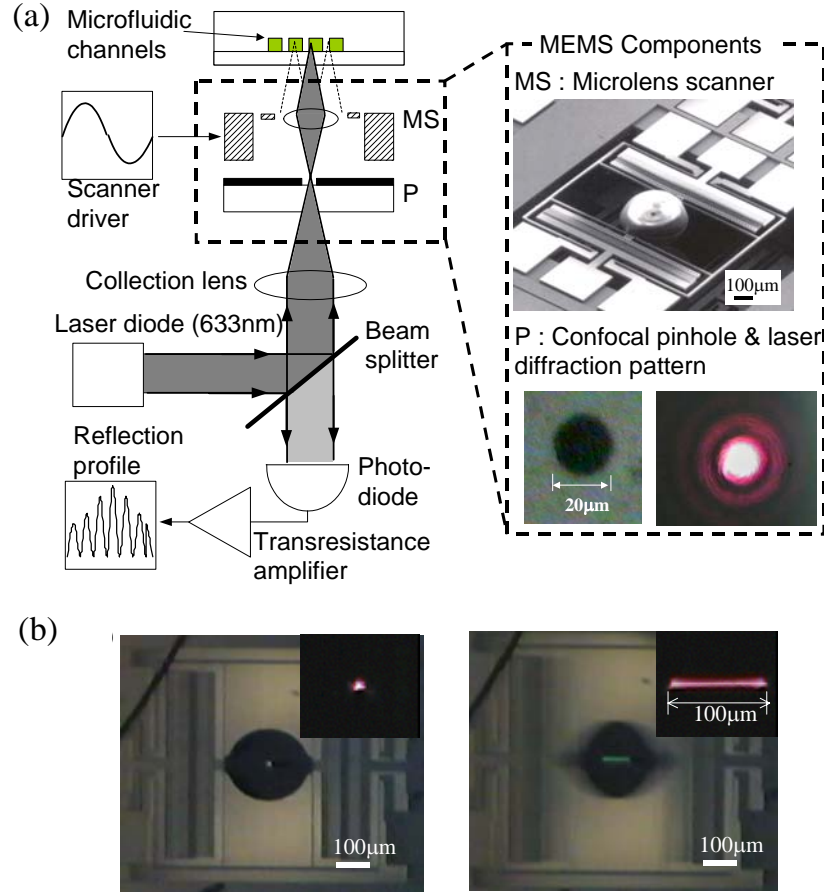
Figure 19. (a) System block diagram of a laser scanning confocal line scanner and its MEMS components (dashed box), and (b) Microlens scanner with a confocal pinhole.

3.2.2 MICROSCALED CONFOCAL IMAGING ARRAY MICROSCOPE

The architecture of the micromachined transmissive scanning confocal microscope, illustrated in Figure 20 (a), consisted of three vertically stacked chips: two microlens scanner chips, and an aperture chip. The microlens scanner chips had microlens scanners as active components for focusing and scanning, and the aperture chip had passive metal patterns such as pupils, pinholes, and electrical connections. The two polymer microlenses worked as doublet objective lenses of the microscope, which was

designed to de-magnify the pinhole onto the focal plane to make a small illumination spot. The doublet objective lens was designed as a Petzval's doublet, a traditional medium power objective lens design using two biconvex lenses.

Major design parameters and device dimensions in millimeter are denoted in Figure 20(a). The focal length of the X microlens, F_{MLx}, was set to the distance between F_{MLx}, F_{MLy}, the lens diameter, and the pinhole diameter are 0.5 mm, 1 mm, 400 µm, and 20 µm, respectively. The distance between pinhole and the Y microlens is designed to be 1.5 mm, which is the sum of the thickness of the Y microlens scanner chip and the thickness of the pinhole chip. The simulated magnification and f-number for this design

Figure 20. (a) Device architecture of the micromachined transmissive scanning microscope, and (b) Schematic diagram of the transmissive raster scanning.

were 0.39 and 1.43, respectively. This doublet objective focused incoming laser light into a spot on the sample.

The raster scanning of the focused illumination spot is implemented by actuating two polymer microlenses in orthogonal direction with different scan-rates, as shown in Figure 20 (b). The electrostatic comb-drive resonates or statically actuates the microlens in one direction. By cascading these microlens scanners, the light can be focused as well as steered in two dimensions within only a 2-mm optical path. In this vertically cascaded transmissive scanning approach, optical alignment is simpler than with reflective scanning, because the two microlens scanners are aligned in plane along the straight optical axis normal to the chips, adhering to the conventional alignment method for IC fabrication and lithography.

Once the overall theme of transmissive scanning was determined, the optical system design was more restricted by availability of the micro optical components and

fixed parameters from the microfabrication process. From the previous sections, two biconvex microlenses with positive lens power were available for the objective lens design. Two positive microlens components with the distance determined by the thickness of the wafer is the starting point for the system design. The Petzval lens is a 150 year old lens design that still remains in various lens libraries. The original Petzval lens was based on a cemented doublet and an air-spaced doublet. However, the term is now generally applied to lenses containing two separate positive powered lens groups. In a sense, the stacked microlens scanner is a form of a Petzval lens.

The Petzval lens is widely used for high-aperture narrow field applications. This lens configuration of two widely spaced doublets is common for medium powered microscope objective lenses. The power layout for this type of lenses is arranged so that the optical work (bending of the marginal ray) is evenly divided to the two lenses. This layout allows a thin-lens arrangement with the space equal to the effective focal length of the objective lens, and that of the second lens about equal to that of the objective lens. This makes the focal length of the first lens twice of the focal length of the second lens. This configuration is ideal for high aperture, narrow field applications, which is suitable for scanning microscopes. The focal lengths can be determined by solving Equations (13) and (14).

$$F_{MLx} = T_x = F \qquad (13)$$

$$F_{MLy} = 2 \cdot F_{MLx} = 2 \cdot T_x \qquad (14)$$

This configuration is also beneficial for scanning because the beam diameter of the second lens' surface is smaller than that of the first lens, and will reduce vignetting caused by lens movement. The conventional thickness of a 4 inch silicon wafer is 500 µm, and can be thinned down to 200 µm. First, T_x was set to 500 µm, which is the thickness of SOI wafers. Then the effective focal length of the system, F, was set to 500 µm, and F_{MLx} and F_{MLy} were set at 0.5 mm and 1 mm, respectively. This design allowed for a Petzval lens configuration.

The first order calculation of the pinhole position and working distance can be made using following two equations:

$$s' = F \cdot (1 - m) \qquad (15)$$

$$s = F \cdot (\frac{1}{m} - 1) \qquad (16)$$

where m, s', s denotes magnification, image position, and object position. From the trade off of resolution and detector sensitivity, a pinhole diameter of 20 µm was set experimentally. To design a 5 µm illumination spot with m of -0.25, s' and s were determined to be 0.6 mm and 2.5 mm, respectively. Since the magnification is determined by the pinhole position at a given lens focal length, the distance between the

pinhole and the X microlens needed to be maximized. A 1 mm thick glass wafer was selected for the pinhole chip rather than a 0.5 mm thick glass wafer, which would result in increased magnification. From the thickness of the glass wafer, T_p was set 1 mm. Because the X and Y microlens scanners were also to be fabricated 0n the same SOI wafer, T_y was also 0.5 mm.

The transmissive scanning confocal microscope design was based on off-axis actuation of the lens elements. Therefore the system parameters such as resolution and aberration vary depending on the position of the lenses. To simulate the off-axis characteristics, a computer model of the micro confocal microscope was constructed using a ray tracing software, Code V^{TM} (ORA, USA). Important system characteristics including illumination spot size, aberration, and scanning range could be simulated before fabrication of the actual system. The Code V model shown in Figure 21 was based on the dimensions that were just discussed. The movement of each lens was modeled using de-centered coordinates. The simulated moving axis of each lens and the distance between the components are shown in the figure.
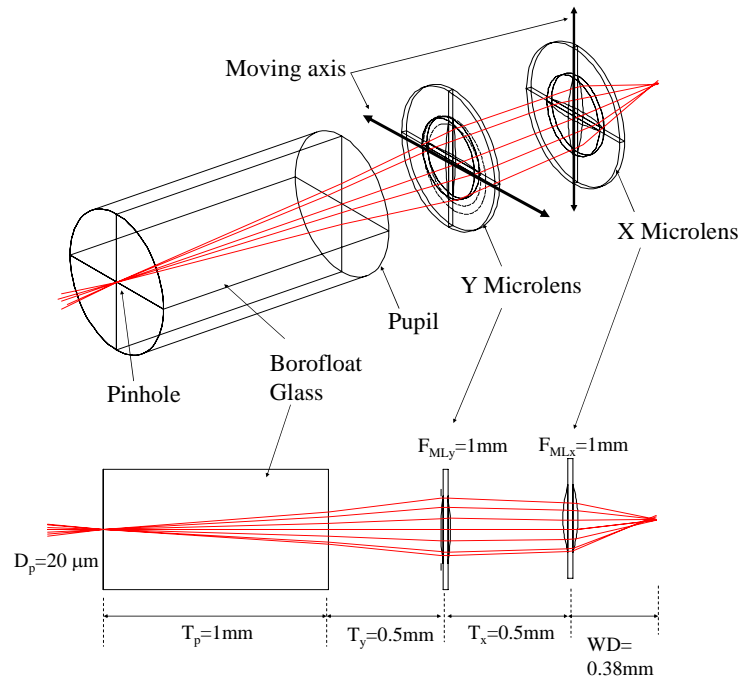
Figure 21. Computer model for the micro-transmissive microscope using Code V.

The point spread function (PSF) is the image of an ideal point object. PSF is an optical analogy to an impulse response from a linear system such as an electric circuit. Transmissive scanning is a time varying system caused by lens actuation. The point spread functions vary with the movements of the X and Y microlenses. Therefore, different positions in the field of view had different PSF's and illumination spots. The

variations of the PSF's at the center and the edges of the field of view were simulated using the Code V model, and the results are shown in Figure 22. The displacement of the X and Y microlens scanners in micrometer is represented by (x, y), respectively. At the center of field of view, both microlenses were on axis and the system's PSF was symmetric. At the edges of the field of view, the microlenses were transversely off from the optical axis. This off-axis configuration distorted the shapes of PSF's, as shown in the figure. The PSF's at the edge of the field of view had a wider Full-Width Half-Maximum (FWHM) than at the center, and were not symmetric. The image quality of this system will degrade at the edges.

(x, y) = (-50, 50)	(x, y) = (0, 50)	(x, y) = (50, 50)
(x, y) = (-50, 0)	(x, y) = (0, 0)	(x, y) = (50, 0)
(x, y) = (-50,-50)	(x, y) = (0, -50)	(x, y) = (50, -50)
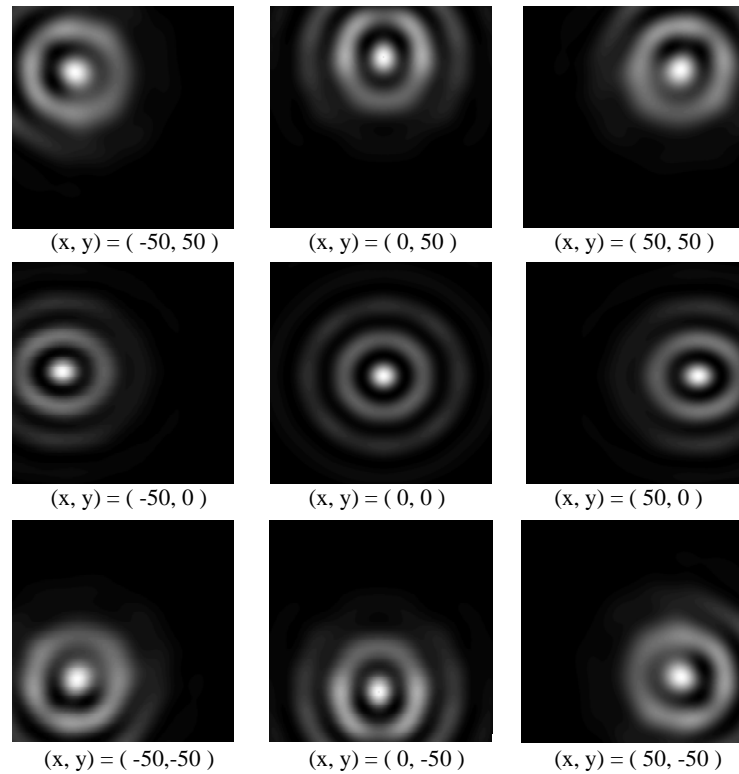
Figure 22. Variation of the point spread functions over the field of view.

The modulation transfer function of illumination was also calculated from the Fourier transform of the point spread function, as shown in Figure 23. Simulated modulation transfer function of the illumination spot of the micro transmissive confocal microscope. The thick dashed line represents the theoretical diffraction limit. The solid line and thin dashed line represent the Modulation Transfer Function (MTF) at the center and the edges of the field of view, respectively. The system is aberration limited. Since the system was to have only two positive lens elements, the on-axis spherical aberration was not correctable within this design.
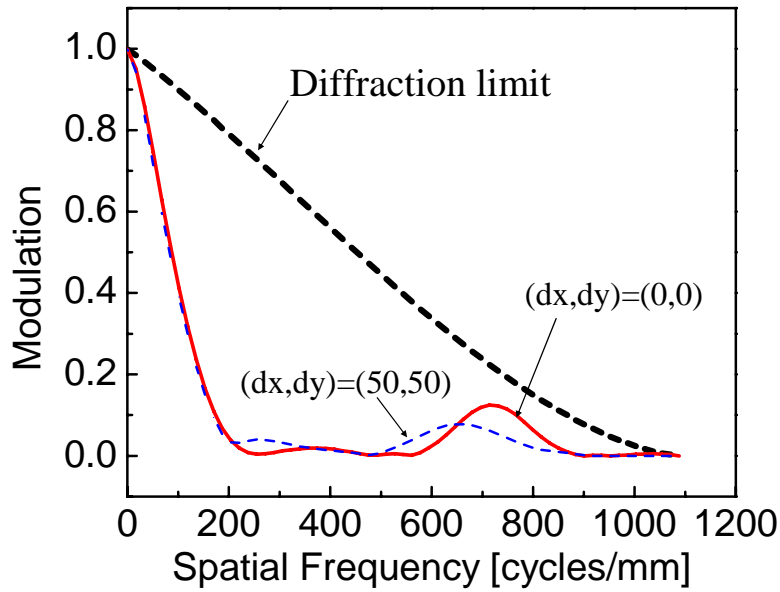
Figure 23. Simulated modulation transfer function of the illumination spot of the micro-transmissive confocal microscope.

The aberration of the system over the field of view is also simulated using the Code V. Figure 24 shows the simulated ray aberration curves at different field of view locations. At each position, the aberration curves for the X and Y axis were plotted at the left and right side, respectively. The type of the dominant aberration can be appreciated by interpretation of the shape of curves. At the center of the field of view (dX = dY = 0), and the under-corrected spherical aberration was dominant, while asymmetric off-axis aberrations such as comma and de-center was dominant as one of the lens moved off from the optical axis.
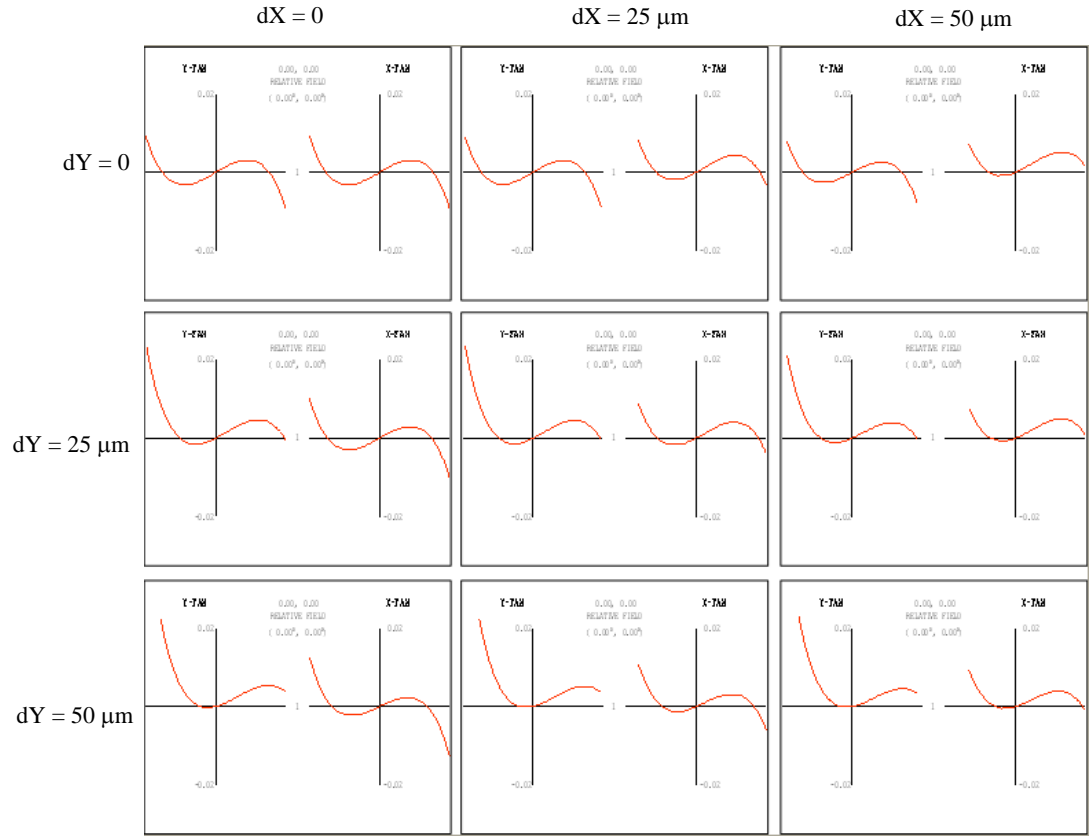
Figure 24. Ray aberration plots for different microlens displacements.

The limiting pupil size also changes as a lens moved off the axis. The movement of the microlenses will cause vignetting of the laser beam. To examine the worst case vignetting effect, a footprint plot of the laser beam on the X microlens scanner (the second microlens) was simulated at different microlens displacements (Figure 25). The beam size at the first lens was assumed to be the same as the diameter of the first lens. Thick solid circle denotes the pupil of the X microlens in the figure. The displacements of the X microlens and Y microlens are denoted by dX and dY, respectively. When the microlenses were actuated to 50 µm, the simulated footprint plot showed that a maximum of 20% vignetting will occur at the edges of the field of view. The vignetting reduced the effective entrance pupil size, and less light passed though the system. The effective numerical aperture was reduced, resulting in a degradation of the system resolution at the edges of the field of view. This would cause non-uniform brightness and resolution over the field of view. However, this was the worst-case simulation, and the reduction of the first lens' beam diameter surface will reduce the vignetting effect at the maximum range of the scanner.

dY=0μm   dY=25μm   dY=50μm

Footprint of incident beam
1: dX=0μm
2: dX=25μm
3: dX=50μm

X Microlens Pupil
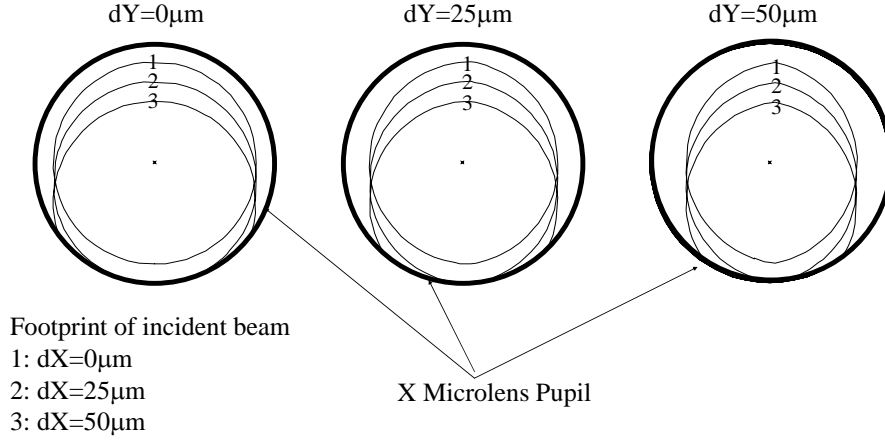
Figure 25. Footprint plots of the laser beam on the X microlens scanner at different microlens displacements.

3.2.3 MINATURIZED TOTAL INTERNAL REFLECTION (MTIR) SYSTEM

A total internal reflection (TIR)-based biochip utilizing a polymer-filled cavity with a micromirror sidewall has been designed (Figure 26). The implementation of a micromirror sidewall cavity will facilitate the precise alignment of the system's excitation light beam. The incident angle of illumination can be easily modified by selecting polymers of different indices of refraction so that optical losses are minimized.

This design will enable the hybrid, vertical integration of a laser diode and a CCD camera, resulting in a compact optical system. One of the advantages of the TIR design is the vertical assembly of the laser source with the micromirror, which allows the integration of a vertical surface cavity emitted laser (VSCEL) array with a TIR array chip. Because external optics were not necessary, this system will be useful for high-throughput applications.
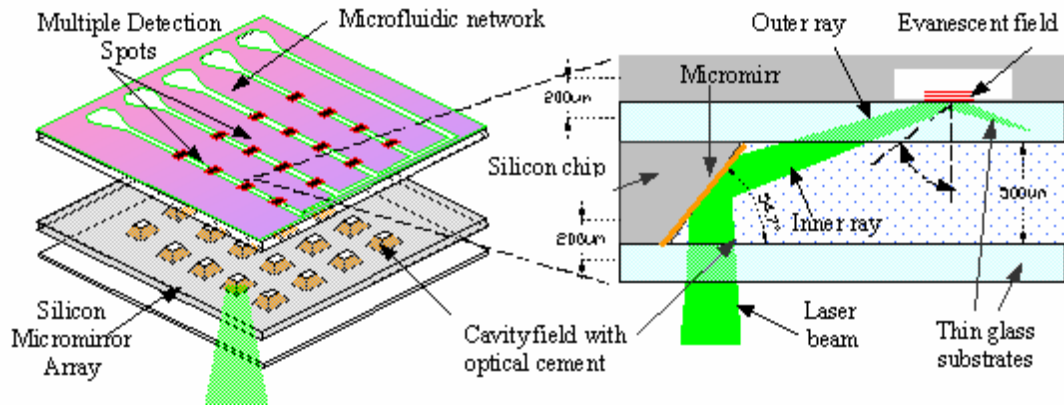
Figure 26. Conceptual drawing of the TIR-based microchip (left). A schematic cross sectional view of the four-layer chip (right).

The biochip will consist of a polymer-filled cavity for efficient light coupling. One of the reflective sidewalls of the cavity will act as a micromirror that directs the excitation light at a predefined angle. Sample delivery microfluidic channels were designed at the top of the chip. The chip will be fabricated using a combination of standard bulk micromachining techniques and PDMS casting. It will enable the hybrid vertical integration of all of the optical components, providing great design flexibility for future miniaturization. The design can potentially incorporate hundreds of detection sites on a single chip, suiting it for various array-type bioassays. In such a configuration the chip would be scanned with respect to a stationary excitation-detection system.

TIR takes place when light travels from a high (e.g. glass coverslip, index of refraction n_1=1.52) to a lower (e.g. water, cells, index of refraction n_2=1.33-1.38) refractive index medium at an incident angle above the critical angle:

$$(\theta_C = sin^{-1}(n), \text{ where } n=n_2/n_1). \tag{17}$$

The light is reflected at the interface and an evanescent component, which decays exponentially with distance, exists near the surface of the lower refractive index media. The selective excitation of fluorophores located only within the evanescent electromagnetic field (generally less than 200 nm) will result in high signal to noise ratio fluorescence enabling the detection of single fluorescent molecules. For a weakly focused beam of wavelength λ, the intensity of the evanescent field $I(z)$ (measured in units of energy per unit area per second) as a function of the distance z from the interface, can be calculated from [89]:

$$I(z) = I(0)e^{-z/d} \tag{18}$$

$$d = \frac{\lambda}{4\pi}\left(n_1^2 \sin^2 \theta - n_2^2\right)^{-1/2} \tag{19}$$

where $I(0)$, the intensity of the evanescent wave at the interface ($z=0$), depends on the two indices of refraction n_1 and n_2, the incident angle of illumination θ and the polarization of the incident light. The p-polarized (parallel to the plane of incidence) and s-polarized (perpendicular to the plane of incidence) components of $I(0)$ are given by:

$$I_S(0) = |A_S|^2 \frac{4\cos^2 \theta}{1-n^2} \tag{20}$$

$$I_P(0) = \left|A_P\right|^2 \frac{\left(4\cos^2\theta\right)\left(2\sin^2\theta - n^2\right)}{n^4\cos^2\theta + \sin^2\theta - n^2} \qquad (21)$$

where A_P and A_S are the corresponding p-polarized and s-polarized incident electric fields amplitudes at the interface. Operation near the critical angle assures strong evanescent intensity. Proper selection of the angle θ is therefore a key feature when designing TIR optical configurations.

3.2.4 SELF-ALIGNED INTEGRATED MICROFLUIDIC OPTICAL SYSTEM

The self-aligned integrated microfluidic optical system (Si-MOS) was designed as a disposable system that could detect fluorescence from a single molecule. The Si-MOS design features two-dimensional planar microlenses that enable the amplification of fluorescence, and high numerical aperture (NA) designs of the integrated planar microlenses that can enhance the amplification of the system by up to 28 times. Disposable self-aligned integrated planar systems were designed using polydimethylsiloxane (PDMS), as shown in Figure 27. Disposable self-aligned compound microlenses on microfluidic channels can be used effectively as low-cost, rapid, and sensitive diagnostic biochips.
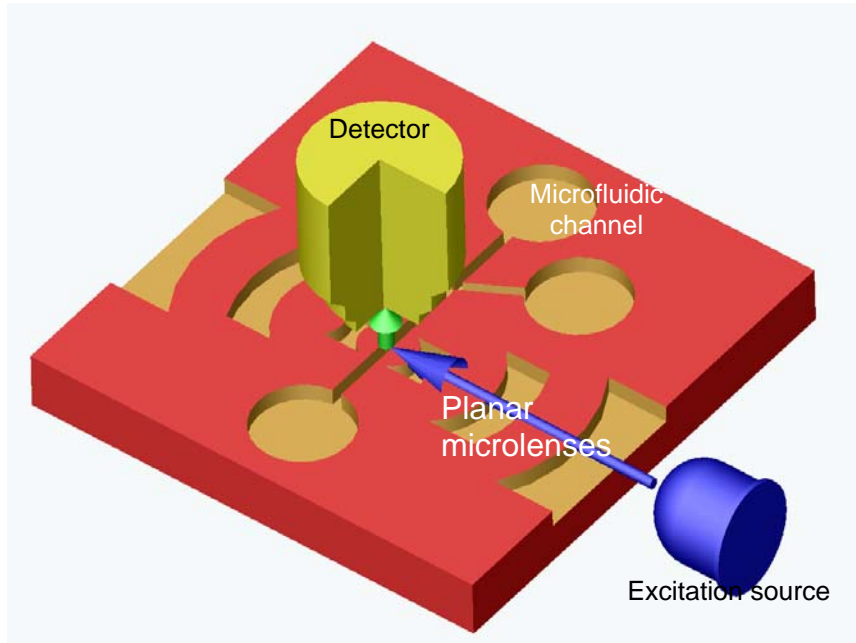
Figure 27. Self-aligned 2-D compound microlens on a microfluidic channel.

The dimensions of the planar microlenses were designed by simulations to minimize the total aberration and to produce a high NA. It was required that the planar

microlenses were fabricated with conventional surface micromachining techniques [68]. The results of the optical simulations using the ray tracing methods are shown in Figure 28. Each design has a different number of collector lenses and collimator lenses. One set of compound microlenses consisted of four different microlenses. In design 1 and design 3, the first lens is used as a collector and the second lens is as a collimator. In design 2, the first and second lenses are used as collectors and the third lens is a collimator. In design 4, the entire four lenses are used as collectors. Even though design 4 had a relatively high spherical aberration, the efficiency of condensation was increased. The refractive index of 1.41 for PDMS [84] was used in these optical simulations. The wavelength of the incident light used was 500 nm. The alignment between the microlenses and the channels was not considered. The planar microlenses and microfluidic channels were to be micromachined together in pre-aligned states in the fabrication process.
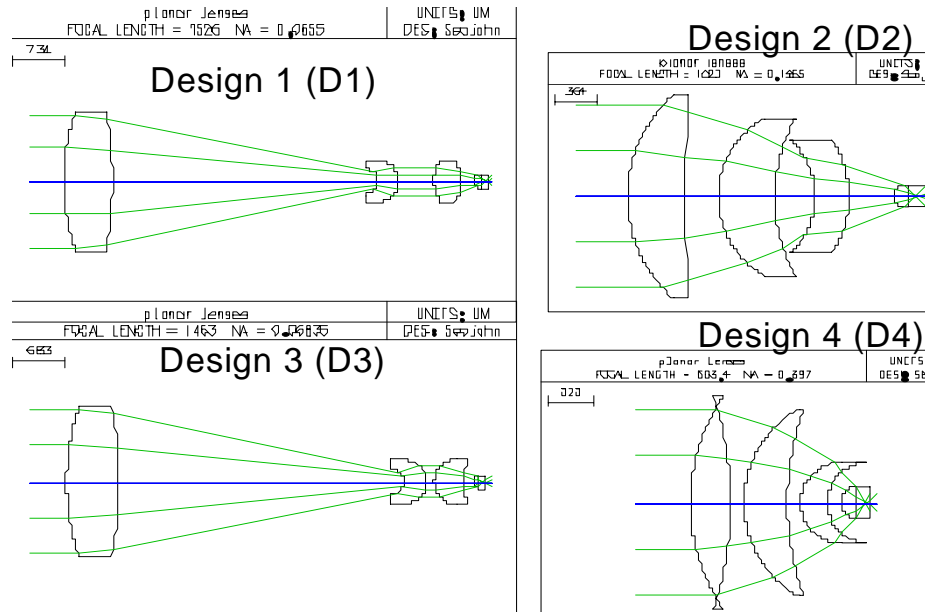
Figure 28. Optical simulations of high NA planar microlens designs.

4. FABRICATION AND ASSEMBLY

The system components and systems were fabricated at the Berkeley Microfabrication Laboratory, University of California at Berkeley, Berkeley, CA.

4.1 SYSTEM COMPONENTS

4.1.1 MICROMACHINED SCANNERS

4.1.1.1 Stacked 2-D Microlens Scanners

The fabrication of the stacked 2-D Microlens Scanners required a combination of three different fabrication processes: (1) the silicon actuator fabrication, (2) the polymer fabrication process for the microlens, and (3) the aligned assembly for the multi-chip stacking. Because of its force stiffness, its vertical stiffness and its ability to achieve high aspect ratios, silicon-on-insulator (SOI) was chosen as the substrate material for the fabrication the lens actuators. A two-mask fabrication method based on deep reactive ion etching (DRIE) was used. In addition, polymer microlens fabrication using the surface tension of liquid phase polymers and a ring shaped lens holder provided a biconvex polymer microlens on the actuators after the actuators were released. The design parameters described in the previous section were implemented in the fabrication steps presented in Table I, which are further displayed in Figure 29.
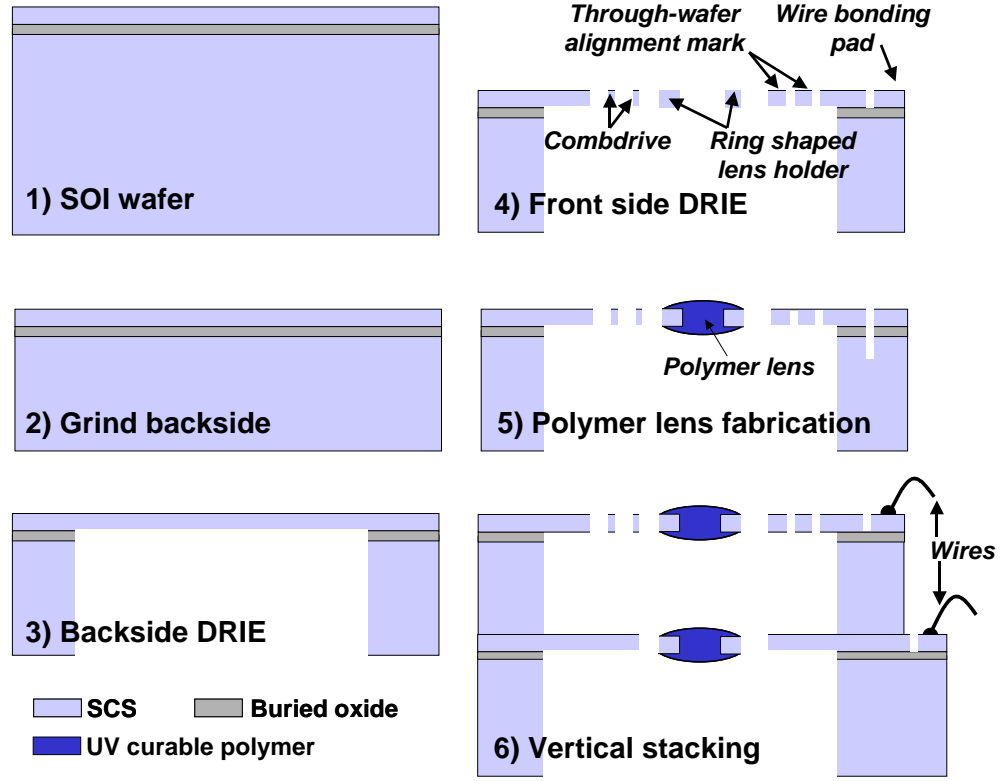
Figure 29. Fabrication process of the stacked 2-D microlens scanner.

Table I. Fabrication steps of the 2-D microlens scanner

Step	Process
1	A SOI wafer with a 20-μm-thick device layer on a 2-μm-thick buried oxide layer on a 525-μm-thick back substrate was prepared. A 0.3 μm-thick thermal oxide was grown to protect the front device layer during the grinding and polishing step.
2	The back substrate was ground and polished (Aptek, CA, USA) to the desired thickness, and oxide on the surface was stripped in buffered hydrofluoric acid (HF). In the grinding step, the lens-to-lens distance was determined by the back substrate thickness. Substrate thickness as thin as 100 μm have been reported in the literature [87]. The distance between the lenses can ranged from 100 μm to 525 μm. The design parameters such as T_1 and T_2 are controlled in this step. For these experiments, T_1 and T_2 were set at 500 μm.
3	A thermal oxide layer of 0.6 μm was grown on the wafer as a front-side etch mask, and then patterned with the first front side mask. The patterns for the actuators, the lens holders, and the alignment marks were transferred onto the oxide mask layer in this step. The second backside mask for the optical windows

	was aligned with the front side and patterned on a 9 μm thick photoresist layer that was coated on the backside of the wafer. The oxide on the backside was also patterned using the thick photoresist mask. All front and backside masks were prepared before beginning the DRIE etching steps to avoid lithography occurring on the etched wafer. The back substrate of the SOI wafer was etched down to the buried oxide by deep reactive ion etching (DRIE) to define the optical window. Then the buried oxide layer was removed from the backside by reactive ion etching to prevent possible membrane explosion in the next front side DRIE step.
4	The actuators were defined in the 20-μm thick front SOI layer by front side DRIE. A low frequency DRIE recipe was used to reduce the footing effect [90]. Because the optical window area included the whole actuator area, the actuators were released from the substrate without wet etching. This large backside opening area was the optical window and provided vertical clearance for the next lens fabrication step. In addition, it prevented squeeze film damping and stiction of the actuator to the substrate.
5	An ultraviolet (UV) curable polymer droplet (NOA63, Norland Products, USA) was placed manually onto the ring shaped lens holder using a glass capillary with 10 μm inner diameter (TIP10TW1, WPI, USA) attached to digitized micromanipulators (MP-285, Sutter Instrument Company, USA) and a time-gated pressure controller (PV830, WPI, USA). This experimental setup is a conventional micropipette setup for injecting of small amount of liquid into a single cell. Silanized glass capillaries were used to reduce the residual polymer on the tip. This setup was used to inject a small volume (10 nl) of the polymer onto the silicon lens holder. NOA63 is a UV curable optical adhesive used for bonding of achromats and was chosen because of its excellent transmission characteristics (larger than 98.5% at 400 nm – 1400 nm), low fluorescence, and high viscosity. The high viscosity in the liquid phase prevented the spreading of the polymer into the actuator region. NOA63 was injected from the glass capillary into the ring shaped lens holder. The ring shape lens holder spatially confined the liquid phase polymer and determined the diameter of the lens. Unlike conventional polishing techniques for lenses, surface tension of the polymer liquid induced a parabolic biconvex lens shape. The focal length of the lenses (F_1 and F_2) was determined at this stage by controlling the volume of the polymer at a given diameter. The volume of the droplet applied was controlled by maintaining the injection pressure at 10 *psi* and varying the injection time with a time gated pressure controller. The liquid phase polymer was then cured under a long wave UV (320 nm-400 nm) lamp (UVC Minilamp, Norland Optical Adhesive, USA) with an average intensity of 2 mW/cm^2 for 30 minutes.
6	Two dies were stacked and aligned under the microscope using through-wafer alignment structures. The through-wafer alignment marks were used to align the top and bottom dies. Using a normal reflective microscope, the alignment mark in the bottom die was seen though the overhanging alignment mark in the top die. After the manual alignment using micromanipulators, the two stacked dies

were glued using epoxy. An alignment accuracy of $\pm 5\ \mu$m was easily achieved using this method. An alignment error of this magnitude can also be corrected using the DC offset in the driving signal of the actuator. Finally, the devices were wire-bonded and packaged.

Fabricated 1-D microlens scanners are shown in Figure 30. Single sided microlens (Figure 30 (a)) had a shorter truss than the double side devices (Figure 30 (b)). Parts of the 1-D microlens scanners were enlarged, and are presented in Figure 31: a ring shaped lens holder, polymer microlens, comb actuators and flexures. These microlens scanners were fabricated in array as shown in Figure 32 (a). Scanning electron micrographs taken from the bottom of the scanner chip showed the etched window defined in handle wafer by the wafer etching (Figure 32 (a)). The substrate materials underneath the devices were removed to release devices and form optical windows.
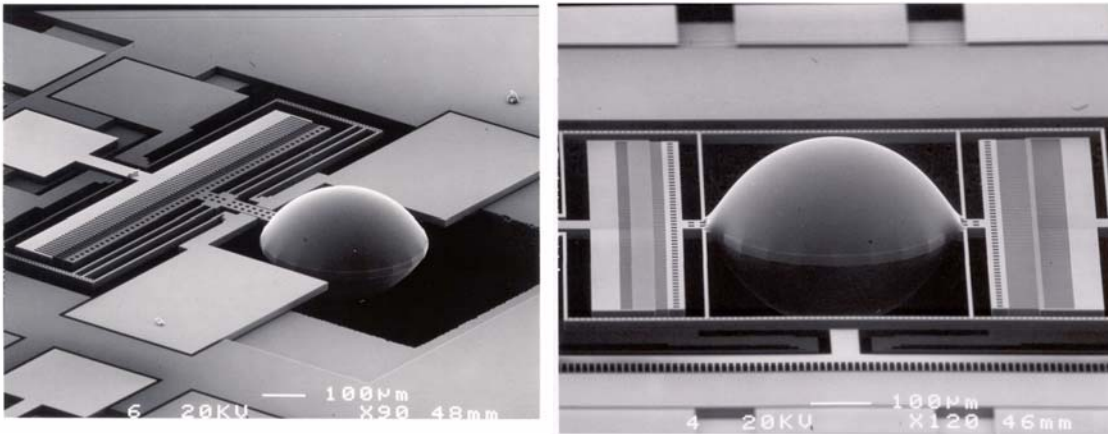
Figure 30. Scanning Electron micrographs of 1-D microlens scanners: (a) a single sided microlens scanner, and (b) a double sided microlens scanner with the thickest microlens.
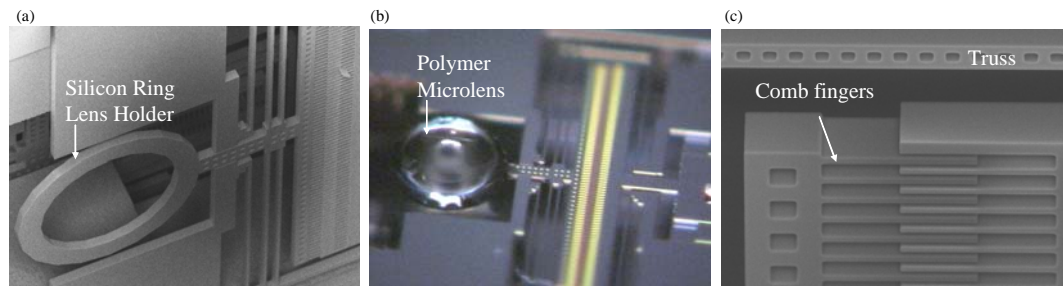
Figure 31. SEM micrographs of a 1-D microlens scanner: (a) silicon ring lens holder, (b) fabricated polymer microlens, and (c) comb fingers and a truss.
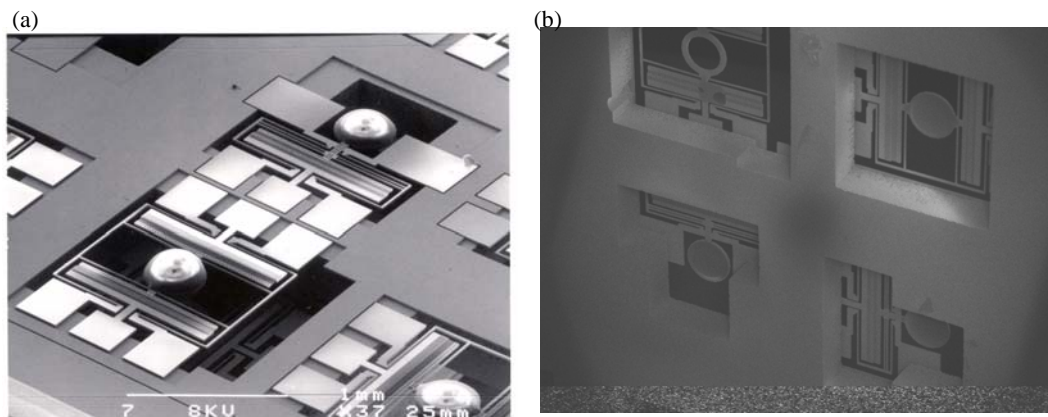
Figure 32. SEM micrographs of microlens scanners taken (a) from the top, and (b) from the bottom.

In Figure 33 are shown SEM micrographs of stacked 2-D microlens scanners. Two 1-D microlens scanners were orthogonally aligned and vertically stacked. Note the outer diameter of the microlens was only 400 µm. The X and Y comb-drives with transparent biconvex polymer lenses are shown in Figure 33(a). Two orthogonally aligned comb-drives in the top and the bottom chip are shown in the Figure. Figure 33(b) shows the top view of the devices under the optical microscope used for alignment.
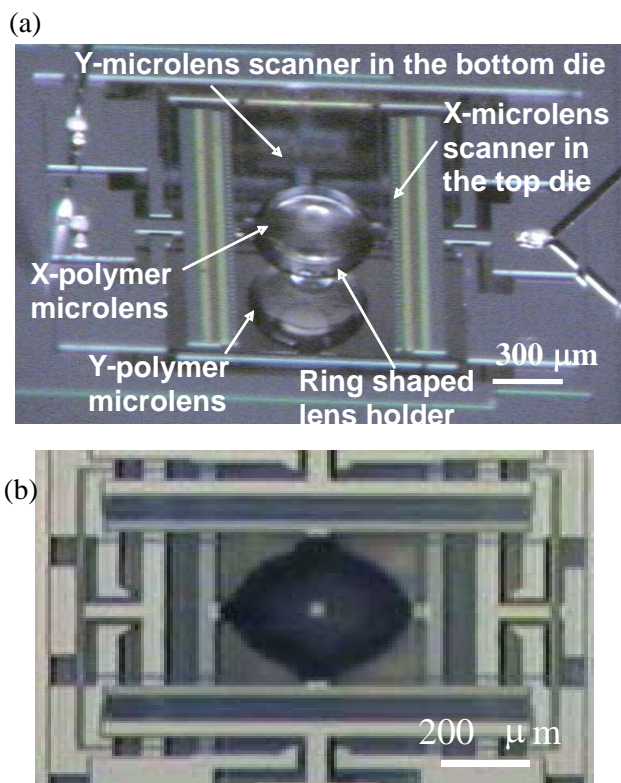
Figure 33. SEM micrographs (a) of a stacked 2-D microlens scanner, and (b) of a top view.

4.1.1.2 Vertical Microlens Scanners

A four-mask fabrication methodology, which provided three design layers and a backside opening, has been previously demonstrated [24]. The process has been improved to allow the self-aligned positioning of those layers for implementation of vertical actuators [26]. A step-by-step outline of this improved fabrication process shown in Figure 34 is described in Table II.

Table II. Fabrication steps of the vertical microlens scanners

Step	Process
1	A double-side polished wafer of 300 μm thickness with a wet oxide was etched with a buried mask and then fusion bonded with another wafer. The resulting SOI wafer was ground and polished to the desired device layer thickness of 50 μm, and the oxide was then stripped.
2	The remaining three front masks were prepared as follows: After a new thermal oxidation step, the first front-side mask for the *Upper* comb-fingers and *High* rigid beams was patterned. The mask designs were actually larger than the desired *High* and *Upper* to allow the alignment margin in the next step. Then a layer of a Low Pressure Chemical Vapor Deposition (LPCVD) oxide was deposited. The second front-side mask was then applied. This second mask had the actual device layers' dimensions and was used to pattern the LPCVD oxide and the thicker thermal oxide underneath it. This effectively self-aligned all three device layers with a single photoresist mask.
3	The self-alignment etch for masks was performed with this second mask, resulting in oxide layer with twice the thickness on the front-side. This self-alignment in the mask level simplified the previously demonstrated self-alignment method [23], which required multiple deep reactive ion etch (DRIE) steps. The backside of the wafer was patterned with thick resist, completing the preparation of all four masks for DRIE.
4	A large backside window was opened using DRIE, followed by a 20 μm thinning of the *Upper* layer from the backside using the buried oxide mask, which resulted in a 30 μm thick *Upper* layer.
5	All three layers were defined by a front-side DRIE step through the entire device layer, followed by a RIE timed-etch of the remaining thin low temperature oxide (LTO).
6	The *Lower* layer was then thinned down to desired thickness by the final front side DRIE, which in this case was 30 μm. In this way, the fabrication of the self-aligned vertical comb-fingers with a pre-engagement of 10 μm was accomplished. After cleaning the surface oxides and any polymer residue, the microlens was integrated. An UV curable polymer droplet was applied to the ring shape lens holder, and the surface tension of the polymer formed a lens shape previously characterized [18]. Exposure to UV light solidified the polymer droplet on the 300 μm diameter lens holder. Fabricated unidirectional and bidirectional devices are shown in Figures 35(b) and (c), respectively.
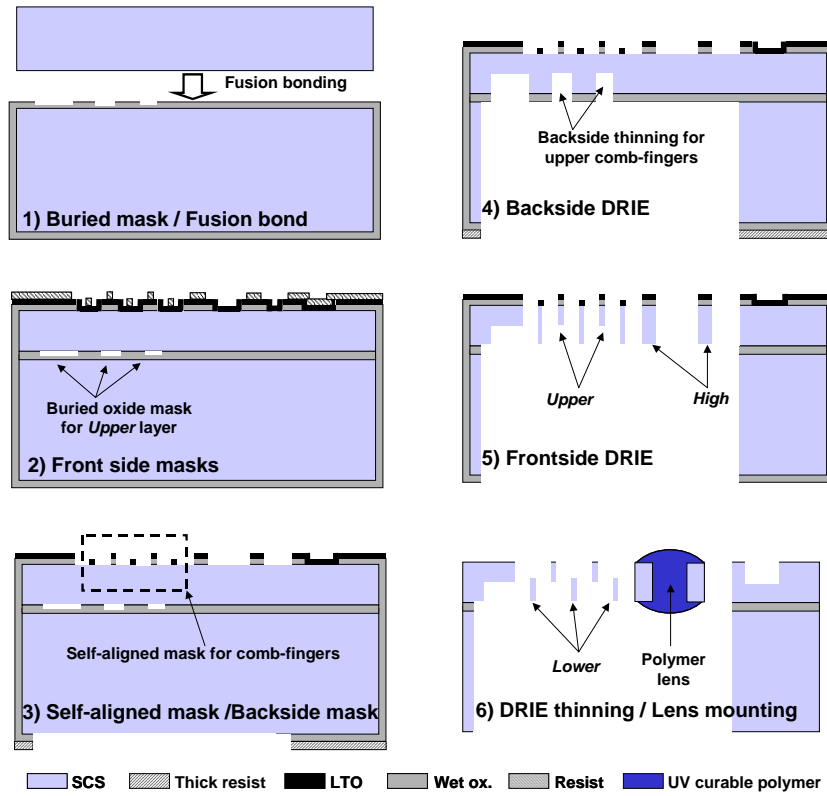
Figure 34. Fabrication process for the vertical microlens scanner.
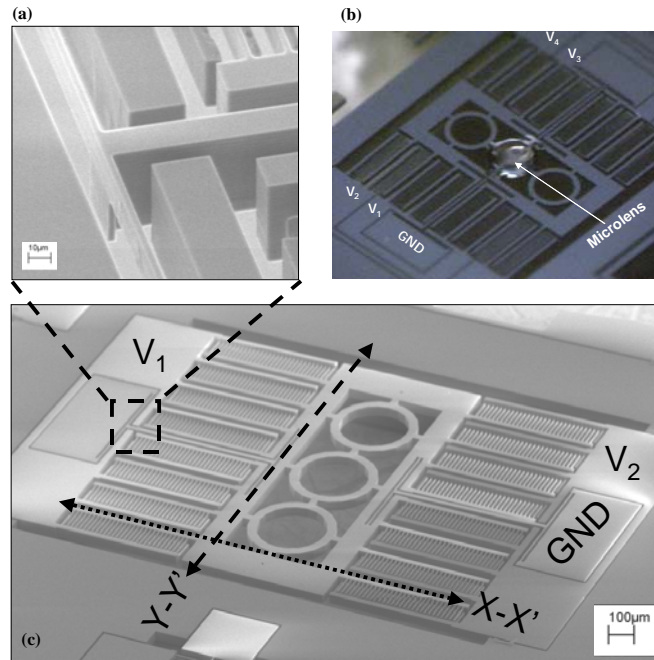
Figure 35. Fabricated microlens scanners: (a) SEM micrograph of a coupled torsion flexure, (b) photograph of a bi-directional device with a polymer lens, and (c) SEM micrograph of a unidirectional device.

48

4.1.1.3 Gimbaled 2-D Scanner with a Backside Island

A thin backside island can be fabricated by a two-step deep reactive ion etching (DRIE) process from the backside as shown in Figure 36 is described in Table III..

Table III. Fabrication steps for the Gimbaled 2-D Scanner with a Backside Island

Step	
1	Masks were patterned into oxide and a thick photoresist layer.
2	Timed DRIE from the back determined the thickness of the island. The island mask was also cleaned by RIE.
3	Blank DRIE from the back transferred the step height of the island until the buried oxide was exposed. The buried oxide was also cleaned by RIE.
4	Finally, the device structure was defined from the front using DRIE. The buried oxide layer under the island served as an insulated connector for the top device structure.
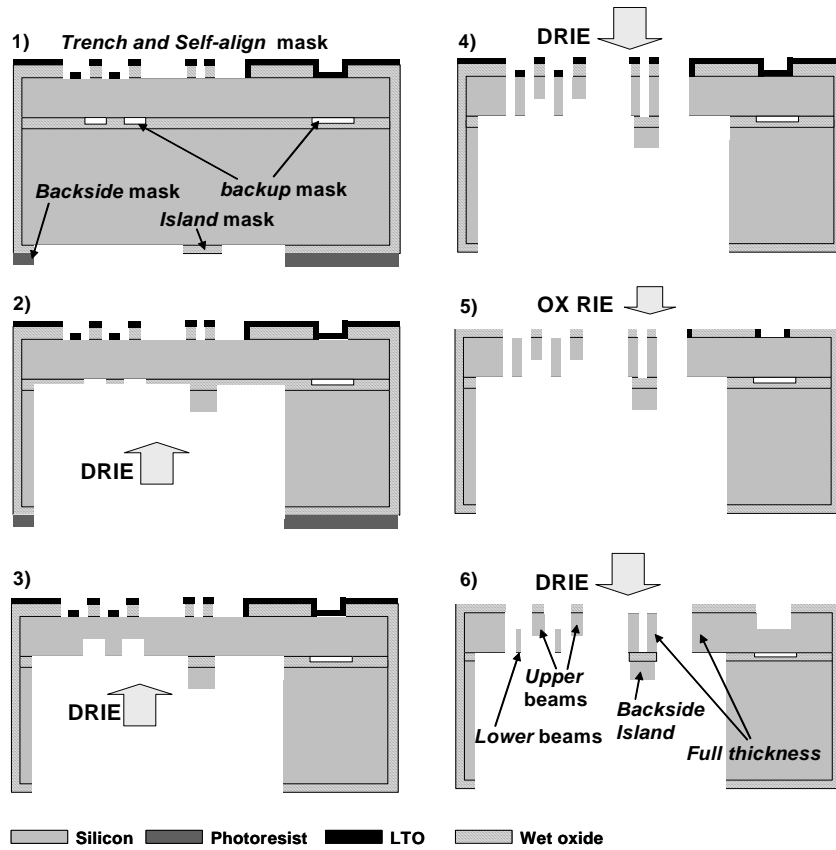
Figure 36. The two-step DRIE backside island process for isolation.

4.1.1.4 Self-Aligned Vertical Comb-Drive

The microfabrication procedure for the self-aligned vertical comb-drive presented in Figure 37 is described in Table IV. The vertical comb drive was fabricated on a SOI wafer using three masks to define a comb drive, a bimorph cantilever, and an optical window.

Table IV. Fabrication steps for the self-aligned vertical comb-drive

Step	Process
1	A 2.3 μm thick oxide was thermally grown in steam at 1150 ˚C on a SOI wafer that had a 10 μm thick top polysilicon layer on an 1 μm thick buried oxide layer on a 500 μm thick silicon substrate..
2	A 0.7 μm thick LPCVD polysilicon layer deposited on the thermal oxide layer was defined by the first mask, and then etched by reactive ion etching.
3	The patterned polysilicon layer protected the oxide on the bimorph cantilevers during the final HF release
4	A second 0.5 μm thick thermal oxide was grown on a polysilicon structure and silicon to serve as a masking layer in defining the structure of comb drives. The polysilicon thickness was reduced down to 0.2 μm during oxidation.

5	After definition of the oxide on the top silicon, the 500 µm thick bottom silicon substrate was etched away by deep reactive ion etching to provide an optical window (Figure 37 (3)).
6	The top silicon structures were etched by DRIE with the previously defined 0.5µm thick oxide mask (Figure 37 (4)).
7	All the grown thermal oxide layers including the exposed buried oxide of the SOI wafer were removed by hydrofluoric acid (HF) (Figure 37 (5)).

The temperature and thickness of the thermal oxidation step (1) were key design parameters that governed the offset between the self-aligned vertical combs (Figure 37 (1)).   Because the thermal oxide and single crystal silicon of a bimorph cantilever are much thicker, this did not significantly affect the residual stresses on the bimorph cantilevers (Figure 37 (2)). The residual stress in the bimorph cantilever resulted in a vertical offset between movable and fixed combs.
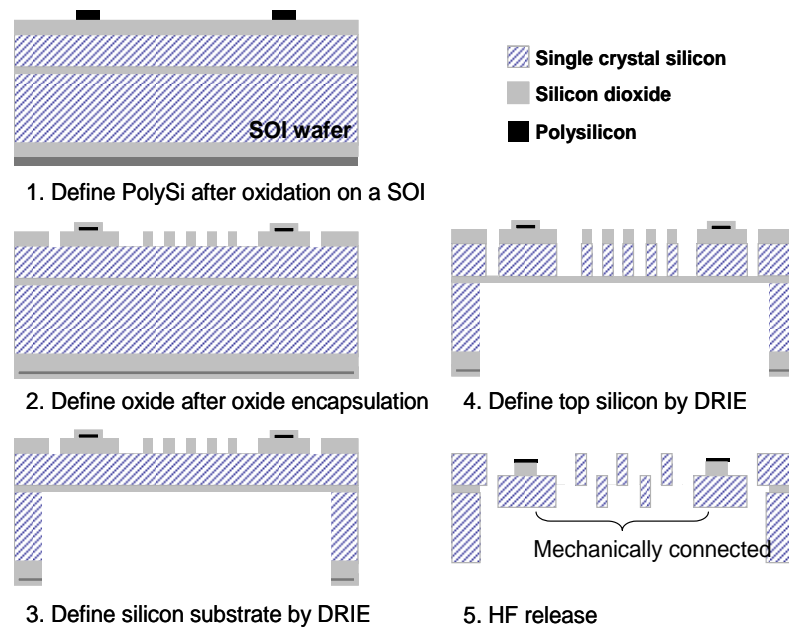
Figure 37. Microfabrication procedure of a self-aligned vertical comb drive using a single SOI wafer.

4.1.2 VARIABLE FOCUS LIQUID LENS

The variable focal length liquid lens unit consisted of four main functional parts, as shown in Figure 38. These four parts were: (1) a transparent electrode pattern, (2) an electrolyte liquid droplet, (3) a hydrophobic insulating layer, and (4) protective structures. Applying an electrical field in the vicinity of the water droplet on a hydrophobic insulating layer, by virtue of an induced capacitive force, significantly altered the contact angle of the droplet, as discussed previously. The chamber with a height comparable with a droplet was designed to prevent evaporation.
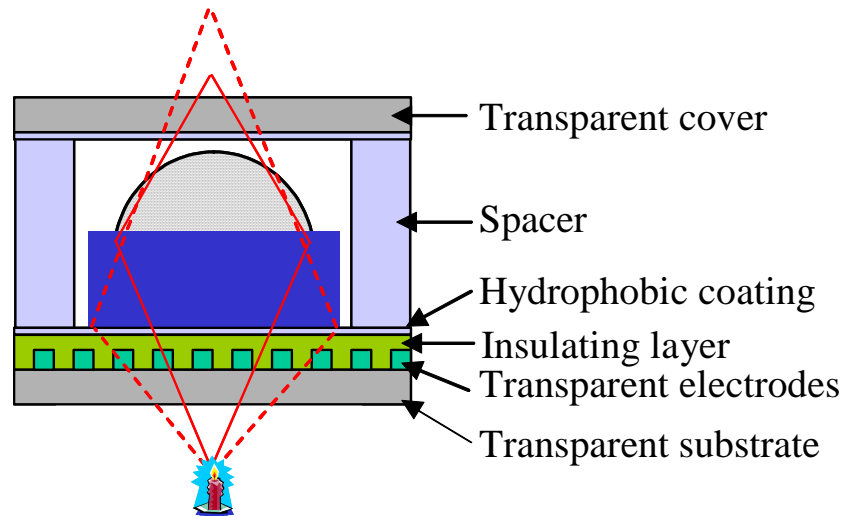
Figure 38. The schematic diagram of a variable focus liquid lens.

Figure 39 (a) shows the design of a concentric electrode pattern that eliminated the need for an invasive electrode in droplets. Other designs of the electrode such as a grid shape electrowetting switch and island active electrode were also tested, but those designs resulted in lenses with more optical distortion than the concentric electrodes. Additionally, concentric electrodes were easily aligned with the liquid droplet in the patterned optical axis.

The fabrication process for the planar electrodes is shown in Figure 39 (b) and is presented in Table V.

Table V. Fabrication steps for variable focus liquid lens

Step	Process
1	First, indium tin oxide (ITO) was deposited on a glass substrate.
2	Then ITO was patterned and wet etched in an aqueous solution of 20% hydrochloric acid (HCl) and 5% nitric acid (HNO$_3$).
3	1 μm-thick Parylene-N was deposited at room temperature on the patterned transparent electrodes.
4	Finally, Cytop™ was spin-coated as a hydrophobic layer on top of insulating layer of Parylene-N.

Because it prevented the electrical breakdown of the hydrophobic surface, a pinhole-free Parylene-N layer was necessary for the switchable electrowetting of the droplet. It was important to maintain the original hydrophobicity of the Cytop™ layer without contaminations to increase the dynamic range of liquid lens.

ITO 100Å
Glass substrate

Pattern ITO
Wet-etch ITO

Deposit 1um
Parylene-N

Coat Cytop™
0.5um

(a)   (b)
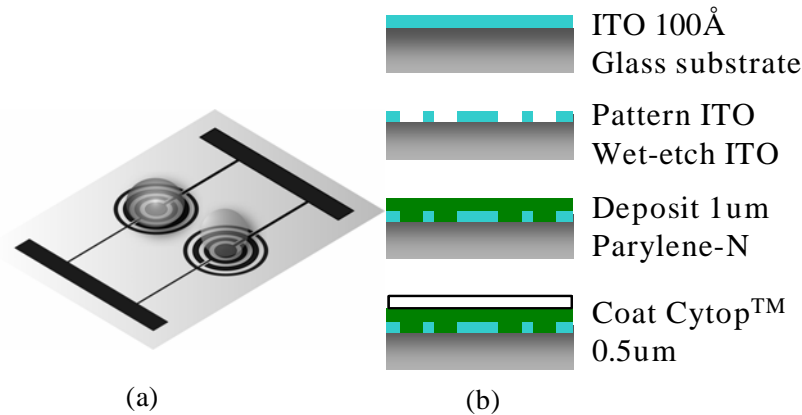
Figure 39. Bottom electrode panel (a) Tested electrode patterns (b) Process flow diagram.

4.1.3 SURFACE ENHANCED RAMAN SPECTROSCOPY (SERS) SUBSTRATES
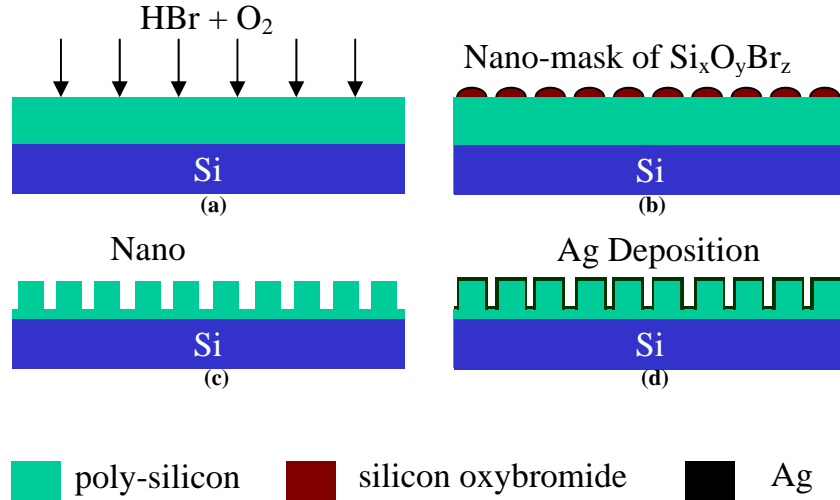
Figure 40. Fabrication process of silicon nanopillars.

The patterned nano pillar structures were created on a silicon wafer using the batch fabrication techniques are shown in Figure 40, and the processing steps are presented in Table VI.

Table VI. Fabrication steps for SERS substrates

Step	Process
1	First, by using mixed hydrogen bromide (HBr) and oxygen (O_2) gases, a polysilicon substrate was simutaneously etched by the HBr and oxidized by O_2.
2	Subsequently pure HBr gas was used to etch uncovered polysilicon substrate.
3	20~50 nm thin films of silver were then deposited using an electron beam evaporator. The sample was mounted in a slanted angle with respect to the silver target and kept rotating during the evaporation process for better coverage on surface.

In 7 seconds high-density nanoscale silicon oxybromide islands natually formed on the polysilicon surfaces. HBr has a extremely high etching selectivity of polysilicon to oxides (200:1), therefore high-aspect-ratio nano pillar structures can be created. The scanning electron microscopy image of a nanopillar structure is shown in Figure 41.
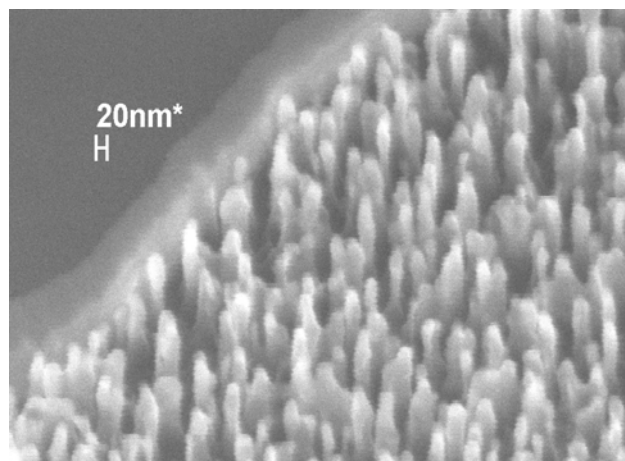
Figure 41. SEM micrograph of silicon nanopillars.
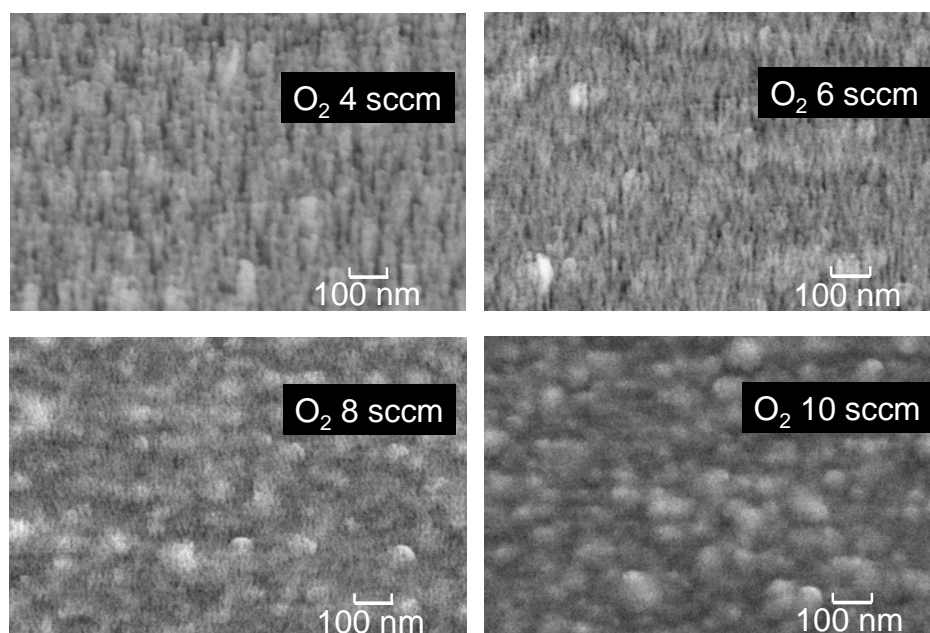
Figure 42. SEM micrographs of nanopillar substrates.

The SEM of nanopillars made under various conditions are shown in Figure 42. The morphology of the nanopillars was dependent on the oxygen flow rate and etching time. The substrates were etched for 1 minute. The surface topology was characterized using an atomic force microscope and the relationship between the pillar density, height and the gas flow rate were compared with etching time.
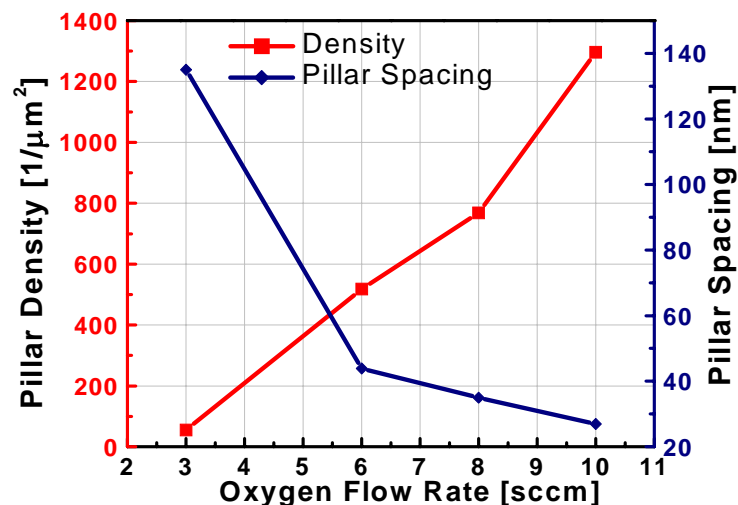
Figure 43. Pillar density and spacing verses oxygen flow rate.

The density and aspect ratio of nanopillars were controlled by the O_2 passivation time, the gas flow rate, and the HBr etching times (Figures 43 and 44). The density and spacing of the nanopillar structure were directly dependent on the oxygen flow rate during passivation. As shown, the pillar spacing decreases as the oxygen flow rate increases, and it is close to zero when the flow rate is high enough; that is, the nanopillar tends to smooth out with very high oxygen flow rate.
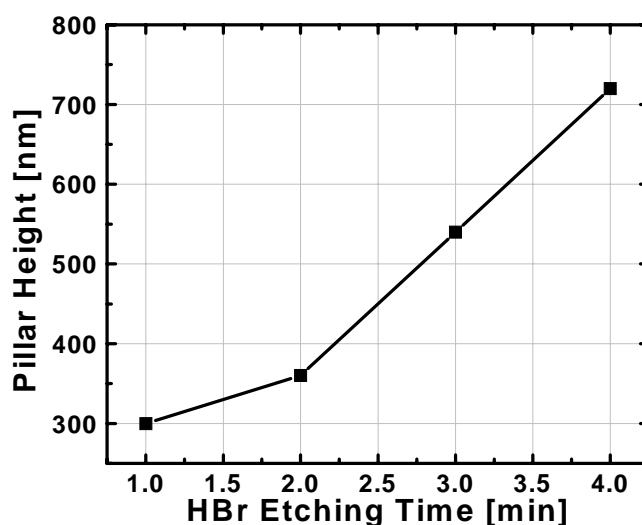
Figure 44. Nanopillar height verses etching time.

The nanopillar structures can be clearly visualized by high magnification dark field microscopy [91] for characterizing the devices and conducting biological experiments. Because the nanopillar substrates were transparent in the visible spectrum, a special dark field configuration was used. A slightly focused and wide light beam was illuminated on the backside of the chip. A partial-reflective glass slide was brought very close to the surface of the nanopillars, and thus the nanopillars were illuminated by the multiple total internal reflections occurring at the interface of the glass slide and nanopillar surface. Due to the scattering from the metallic nanopillar, the structures

appeared larger than their actual size in the images, as shown in Figure 45. These dark field microscopy photographs are of nanopillar structures that were fabricated at the conditions of (a) 1 min etching and 4 sccm O_2 passivation, (b) 1min etching and 6 sccm O_2 passivation, and (c) 1min etching and 10 sccm O_2 passivation.

(a)

(b)

(c)
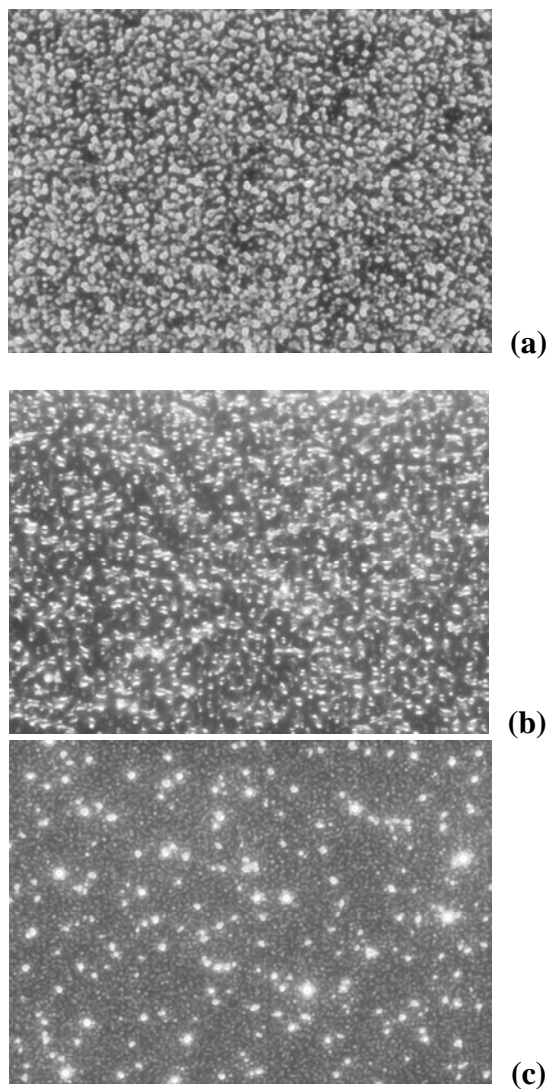
Figure 45. Dark field microscopy images of nanopillar structures at 1 minute etching (a) 4 sccm O_2 passivation, (b) 6 sccm O_2 passivation and (c) 10 sccm O_2 passivation.

The metalized nanopillar structures were then directly used as the SERS substrates.
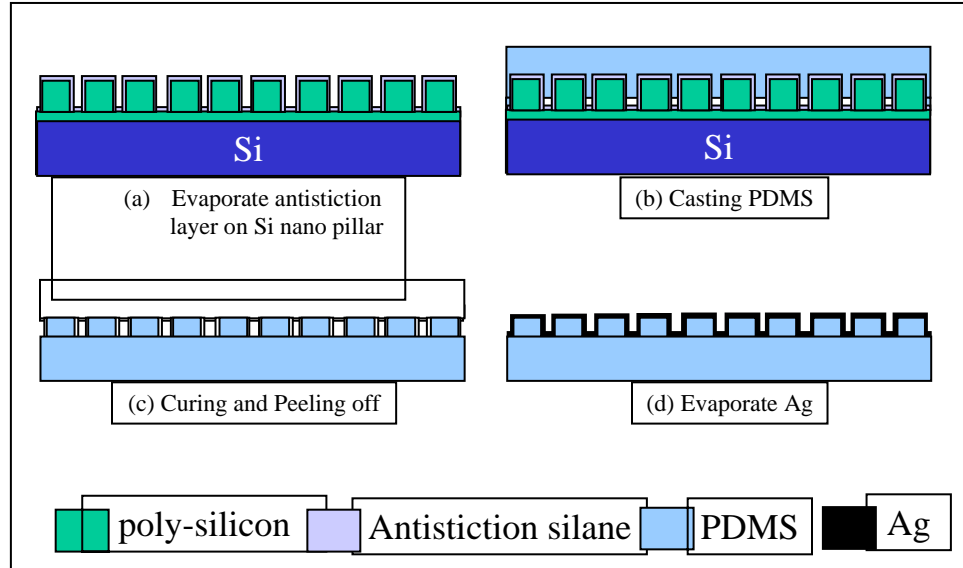
Figure 46. Fabrication of the PDMS nanowells.

The silicon nanopillar can also be used as the mold for Polydimethylsiloxane (PDMS) replication, as shown in Figure 45. In order to keep the integrity of the nanoscale structure on the PDMS during the peeling off process, the silicon nanopillar was salinized with an anti-stiction agent (tridecafluoro-1,1,2,2-tetrahydrooctyl)-1-trichloro-silane ($C_6F_{13}CH_2CH_2SiCl_3$) in a chemical vapor deposition chamber before casting PDMS [92]. The PDMS layer was cured at room temperature and then peeled off. A 20 nm silver (Ag) layer was then evaporated on the PDMS surface. Figure 46 shows a SEM micrograph of a Ag deposited nanowell structure on PDMS.
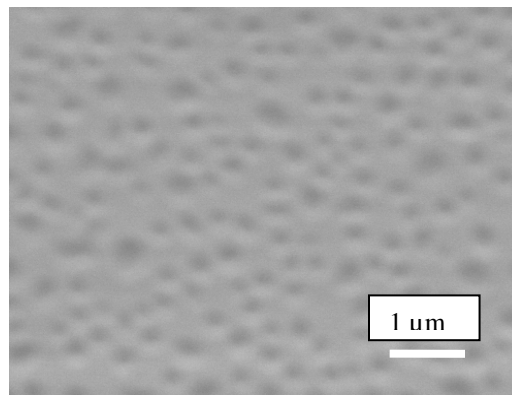
Figure 47. SEM micrograph of the PDMS nanowell.

4.1.4 Polymer Microrobotics Workstation

Polymer microrobotics actuators were fabricated using surface micromachining techniques in a three-mask process (Figure 48) that is described in detail in Table VII. Three photolithographic steps were used to pattern the dimples, the Cr/Au heating

elements and the SU-8 structures. Novel polymer (SU-8) actuators were developed that can be activated in ionic physiological media. To demonstrate the ability of those actuators to operate in liquid environment, a microrobotic workstation capable of manipulating single cells solution was fabricated. Those actuators were electrothermally activated and used to build various microfluidic components, including mechanical pumps, valves, cell manipulators or even cell sorters and cell lysing devices.
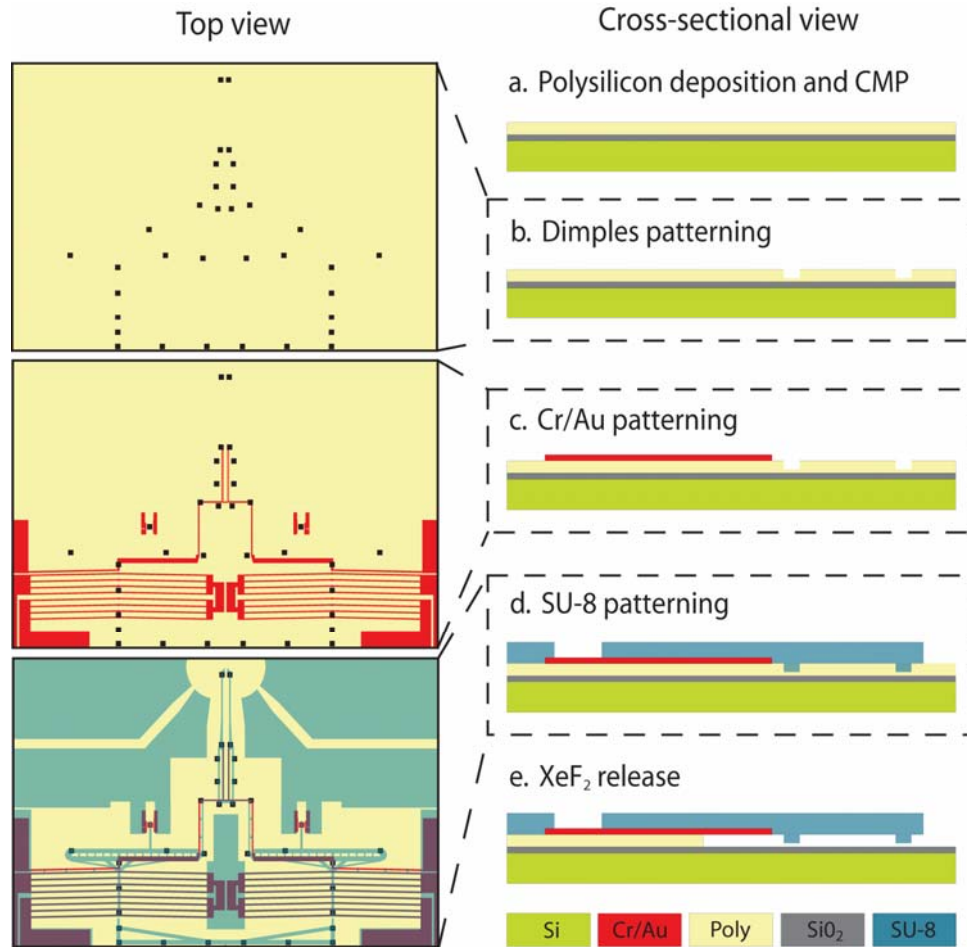
Figure 48. Schematic drawing of the fabrication process of the microrobotic workstation.

59

VII. Fabrications steps for the polymer microrobotics

Steps	Process
1	Starting with an oxidized silicon wafer, a layer of 2 µm undoped polysilicon was chemically vapor deposited followed by chemical-mechanical polishing (CMP). The silicon dioxide layer provided thermal and electrical isolation while the polysilicon layer was used as the sacrificial layer.
2	CMP made the polysilicon surface smooth and reflective, and was an extremely important step for patterning the thick SU-8 film. The UV light during exposure can be severely scattered if the polysilicon surface is rough, making impossible to resolve patterns the SU-8 film.
3	The first photolithographic step transferred the 1 µm deep dimple areas to the polysilicon film. The metal heating resistors, connecting lines and pads of the actuators were subsequently defined by lift-off. Those metal elements consisted of a 20 nm / 360 nm thick electron-beam evaporated Cr/Au film.
4	A 20 µm thick SU-8-2015 layer was then spun on the wafer and photolithographically patterned to form the structural layer. The wafer was diced, the individual chips were hard baked on a hot plate at 120 ^{o}C for 15 min and then dry etch-released in xenon difluoride. Xenon difluoride has excellent selectivity to SU-8 and it produced gas phase products that eliminating stiction problems.
5	The released structure was hard baked for a second time at 95 ^{o}C for 15 min to enhance the crosslinking of the SU-8 film.

The released SU-8/Au/Cr structure bent slightly out of plane (Figure 48). Due to the swelling and expansion of the SU-8 layer, the structure restored its flatness when immersed in liquid.
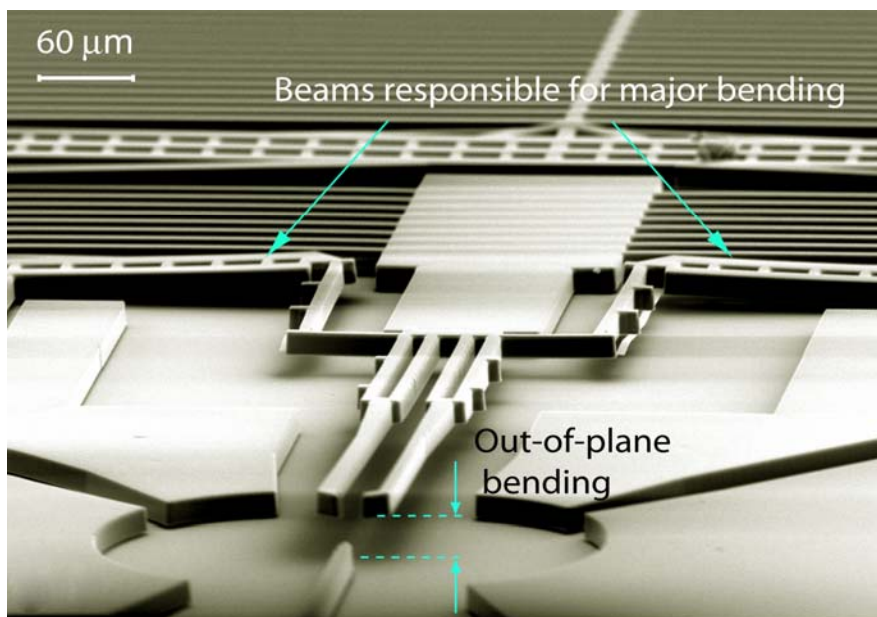
Figure 49. The supporting beams (shown with blue arrows) causing out-of-phase bending of the released cell gripper.

The SU-8 structures suffered from (in-plane) tensile residual stresses. Hot-and-cold arm actuators were anchored at one end and therefore the residual stress was relieved upon release. That was not the case for the SU-8 based chevron actuators. Because both ends were anchored to the substrate, the residual stress was not fully relieved. Although they backbend several microns upon release (backbending of 6.5-7 µ*m* at the center of the V-shape beam was typically observed), some residual stress was still present that severely restricted motion.

The remaining residual stress was compensated for by adding longer (1200 µm) and wider-stronger (12 µm) sets of SU-8 chevron beams (without a Cr/Au layer) (Figure 49). The longer chevron beams were facing in the opposite direction than the chevron actuators, and acted as restoring springs that pushed the SU-8 actuators forward, thus reducing the backbending of the chevron actuators by up to 5 µm.

Another way that eliminated the residual stress was to add crosslinks to the polymer network while the actuator was being manually stretched. This was done by using a probe tip to force the actuator forward, several microns from its released position (typically 21 microns from the unreleased position corresponded to 0.25% strain). While the actuator was stretched, current was passing through. The generated heat produced crosslinks to the remaining unpolymerized SU-8 molecules. The additional chemical bonds in the stretched position counterbalanced the bonds formed during exposure and post-exposure bake (PEB), and reduced the backbending to 2-3 microns. The actuator finally returned to its initial position (zero backbending) when immersed in liquid due to the swelling of the SU-8. In Figure 49 the backbended V-shaped SU-8 beams have pushed the chevron actuators forward. The red circles indicate the points of contact.
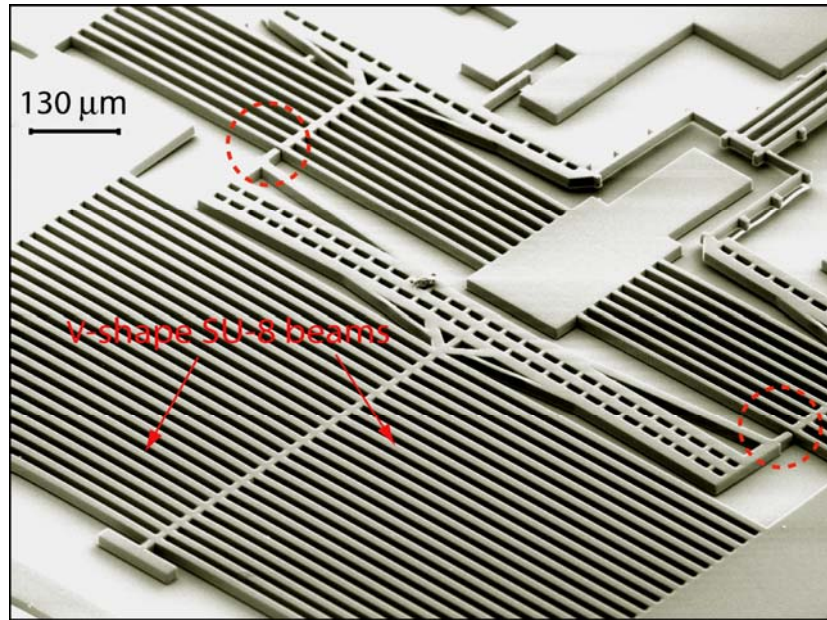
Figure 50. Design method to relieve the residual stress on the SU-8 chevron actuators.

4.2 MICROSCALED SYSTEMS

A computerized multi-channel high voltage source was developed for the multichannel electrokinetic pumping and electrowetting experiments. A total of six high voltage channels were electrically isolated from each other, and were controlled by Atmel microprocessors through a digital-to-analog (DA)/AD link. A Labview program that ran on a personal computer (PC) utilized a graphical user interface (GUI), communicated with the microprocessors in the high voltage source, and displayed the acquired data. High voltages of up to 1500V were generated with a limiting current capacity of 0.5 mA. This was achieved by using a voltage source for the photomultiplier. Figure 50 shows the system block diagram and a photograph of the developed system.
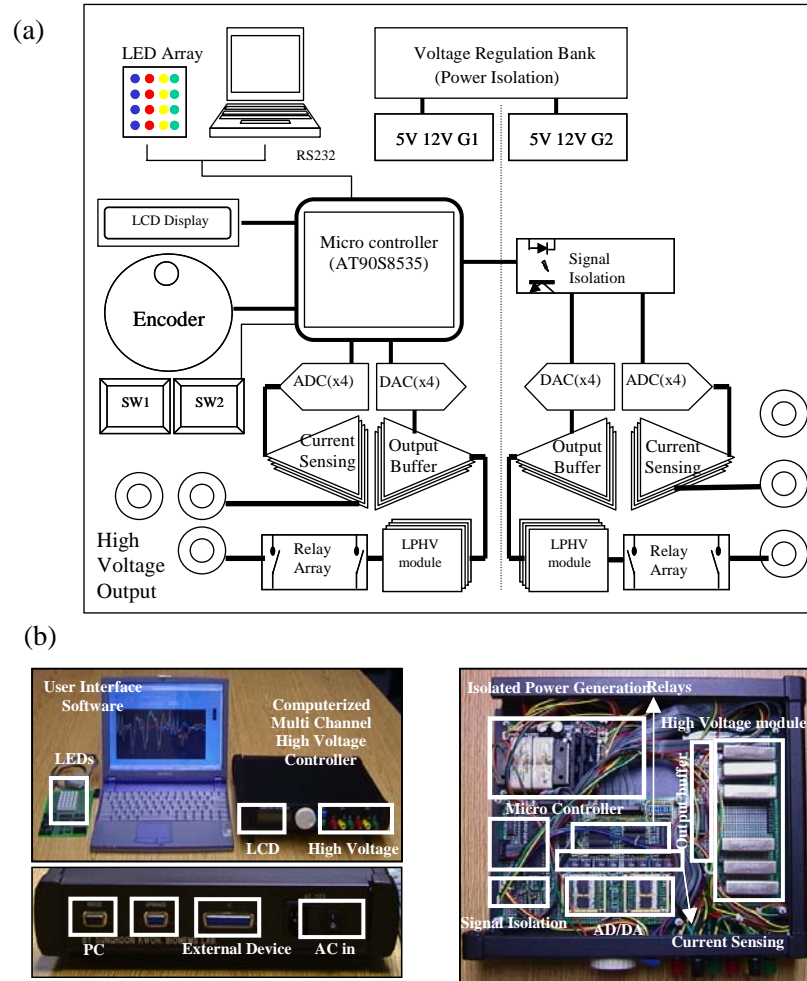
Figure 51. Computerized, multichannel high voltage source (a) block diagram and (b) photograph.

The computerized multichannel high voltage source specifications are presented in Table VIII.

Table VIII. Computerized multichannel high voltage source specifications

	Software	Controller
Features	**Windows based GUI**	**Stand alone as well as PC connectable via RS232**
	Labview 5.0	**LCD display (Character, 20*2)**
		Optical encoder and switches
		Easy program upgrade
		Two different grounds
		Microcontroller (AT90S8535), 128K external EEPROM
Functions	**8 channel arbitrary waveform generation**	**8 channel High voltage source: 0-1250V, independent arbitrary waveform**
	Downloaded control algorithms and waveforms to microcontroller	**8 channel current sensing**

Upgraded external controller program	8 channel controllable mechanical relay
	Two isolated internal power source (two 5V and two 12V)
	External EEPROM : special waveform memory

4.2.1 GIMBALED 2-D MICROMIRROR

For a gimbaled two-axis micromirror with vertical comb drives, the backside island process (Section 4.1.1.3) was incorporated with the vertical comb drives fabrication process (Table IX). Figure 52 shows the fabrication process for the gimbaled micromirror.

Table IX. Fabrication steps for the Gimbaled 2-D Micromirror

Step	Process
1	The process begins by fabricating the 4" SOI wafers. One wafer, intended for the SOI handle is double-side polished with a thickness of 300 ± 1 μm. The second wafer, which will become the device layer, was an *n*-type wafer, standard thickness (525 ± 25) μm, and was single-side polished. A wet thermal oxide of 1 μm was grown on both wafers. The oxide on the handle wafer's side was patterned before the bonding. After 1 μm thermal oxides were grown on both wafers, the wafer intended for the SOI handle was patterned with the mask *Backup* (Figure 52), and the oxide was etched down to the silicon. After removing the photoresist mask and cleaning, the wafers were pre-bonded, annealed, and ground and polished to the desired device layer thickness. Using the finished SOI wafers, the two front-side masks were prepared utilizing oxides of two thicknesses. The mask preparation was designed to provide self-alignment of vertical comb-drives. Because the *Backup* mask was already buried within the SOI wafer, the mask preparation process required that both front-side masks be aligned to that buried layer. On the backside of the wafer, two additional masks were employed and aligned to the front-side features. The masks for *Backside* and *Island* were patterned on the 1.5 μm of oxide from front-side preparation and an additional 9-μm thick photoresist layer, respectively. These two masks were used to generate two different step heights in the next DRIE steps.
2	The backside island was fabricated by DRIE etching from the back side of the wafer. The concept of backside etching was previously described. The first backside DRIE was timed, as it determines the thickness of the backside island. After the timed etch, the island mask was removed by RIE. The next backside DRIE was performed until the etched trench reached the buried oxide.
3	Figure 36 shows a schematic cross section of the chip and the path of the light beam as it passes through. A polymer-filled cavity and its micromirror sidewall are implemented to direct the excitation light beam at an angle above the critical angle The backside DRIE for the upper comb fingers exposed the insulating oxide and the buried *Backup* mask (Figure 52 (2)). The insulating oxide was then thinned by a timed oxide etch to 1.2 μm, which

	exposed the backside of the device silicon layer in the patterned areas of the buried *Backup* mask. In the final backside DRIE step, the actual Backup DRIE into the device layer was performed. This etch is timed to leave a desired thickness of Upper beams. In most cases about 20 µm of device layer silicon was etched such that the remaining Upper beam thickness was 30 µm. Lastly the insulating oxide was fully removed from the backside.
4	The front-side DRIE steps are shown in Figures 52 (4) and (5). First DRIE etched through the device layer, as shown in Figure 52 (5). The second and final DRIE was then performed until the *Lower* beams were lowered to the desired height of 30 µm. The final result is shown in the schematic in Figure 52 (6).

1) Two step backside masking

Backside mask

Island mask

2) Backside DRIE Si/ RIE SiO$_2$

3) Backside blank DRIE Si / RIE SiO$_2$

4) Frontside DRIE Si

Backside island

SCS   Thick resist   SiO$_2$
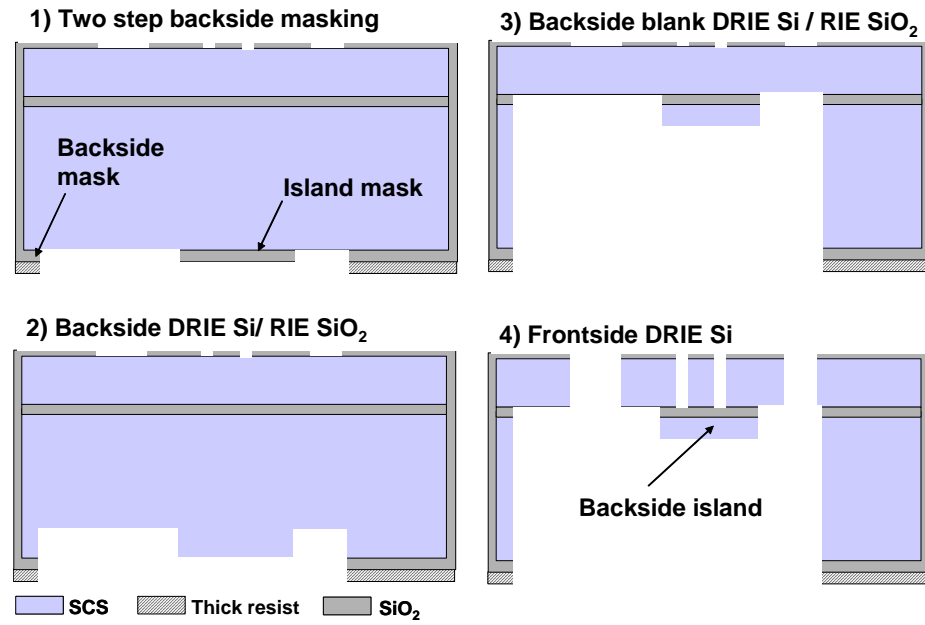
Figure 52. Fabrication process of the vertical comb based gimbaled micromirror.

4.2.2 MICROMACHINED CONFOCAL LINE SCANNER

Figure 53 shows the micromachined transmissive confocal microscope, which has objective lenses, scanners, a pupil, and a pinhole of the confocal microscope. In this section, the fabrication of the transmissive scanning confocal microscope will be discussed as follows: fabrication of the stacked 2-D microlens scanner, fabrication of the aperture chip, and assembly.

2 mm

Objective lens + scanners + Pupil + Pinhole
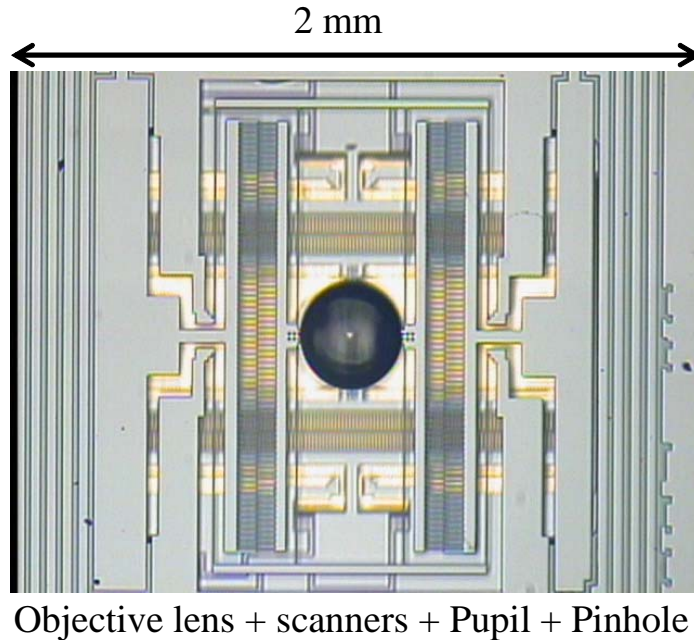
Figure 53. Microscope photograph of the transmissive scanning confocal microscope.

4.2.2.1 Single Microlens Scanner Chip

The single microlens scanner chip is designed in such a way that stacking of two identical microlens scanner chips can result in a stacked 2-D microlens scanner. This is achieved by proper arrangement of X and Y microlens scanners in a chip and stacking with an offset. Because X and Y scanners are alternated in a row in a scanner chip, stacking of two identical scanner chips with an offset of 2 mm allow orthogonal arrangement of X and Y scanners and opens the window for electrical connection to the devices in the bottom chip.

The microlens scanners are fabricated on a silicon-on-insulator (SOI) wafer using multiple deep reactive ion etching (DRIE) steps: front side etching for actuator definition and backside through wafer etching to open an optical window. The polymer microlenses are fabricated within the SOI electrostatic comb actuators using UV curable polymer injection. The focal length of the microlens is controlled by injection volume

and the surface tension induces a biconvex lens profile. Two microlenses with focal lengths of 0.5 mm and 1 mm have been fabricated.
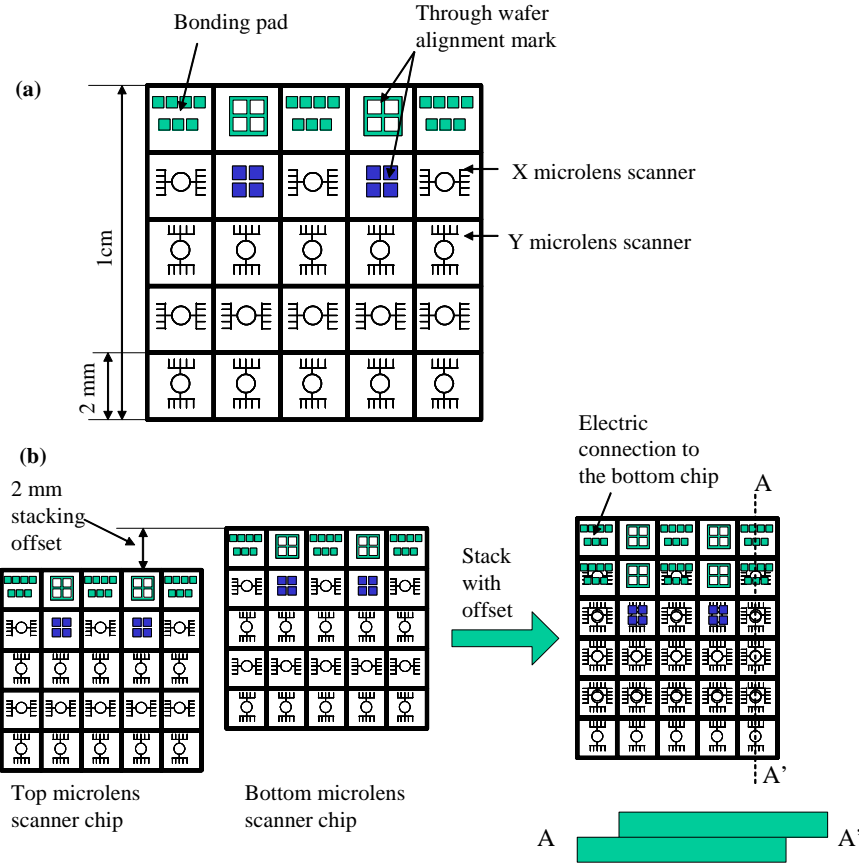
Figure 54. Design of a microscanner chip and (b) Stacking two identical chips with an offset.

4.2.2.2 Aperture Chips

The aperture chips are fabricated on a 1 mm-thick Pyrex^{TM} wafer according to the fabrication steps shown in Figure55. Gold patterns for pupils and electrical connection are patterned on the front side of the wafer by electron beam sputtering of the gold and lift-off patterning. Gold is selected due to its affinity to bonding wires. Aluminum patterns for pinholes are patterned on the backside by sputtering of aluminum and dry etching patterning. The aluminum is selected as pinhole material since the dry etching is required to define a small pinhole size. These patterns of pinholes and pupils are lithographically aligned in the fabrication step.

1) 1mm-thick glass wafer

2) Sputter 250 nm-thick Aluminum on the backside
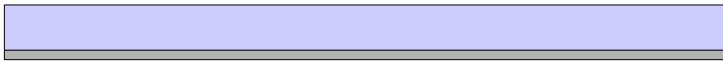
3) RIE Aluminum to define Pinholes

4) Pattern Photoresist on the frontside
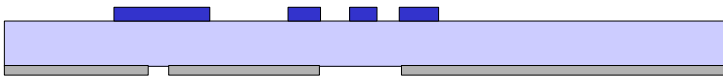
5) E-beam evaporate Au/Cr (0.5 μm)
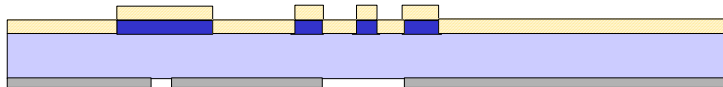
6) Lift-off Au/Cr to define pupil and pad

Pupil

Alignment Mark for Stacking

Wire Bonding Pad

Pinhole

Glass		Aluminum
Photoresist		Gold
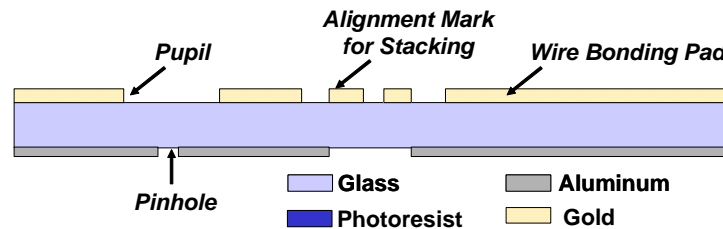
Figure 55. Fabrication process for the aperture chip.

Figure 3.37.   Fabrication process for the aperture chip. Pupils, alignment marks for stacking, and wire bonding pads are gold patterned on the top side of the glass wafer. Pupil is patterned on the backside aluminum layer and is lithographically aligned to the pupil.
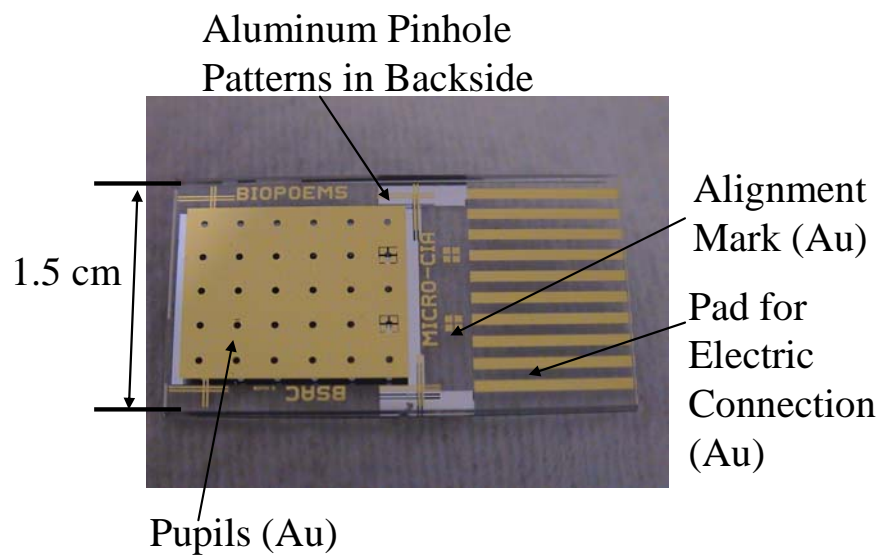
Figure 56. Photograph of a fabricated aperture chip.

The aperture chip has passive pinholes and pupils made of aluminum and gold on either side of the glass wafer. It works as a base for the stacked 2-D microlens scanner. Bonding pads for electrical connection is patterned on the gold layer.

4.2.2.3 Assembly Sequence

Two microlens scanners and the aperture chips are stacked as the assembly sequence shown in Figure 57. First, an aperture chip with 'positive' alignment marks on the surface is prepared. Positive and negative represent just one type of complementary alignment mark. Then a Y microlens scanner chip is stacked via aligning the negative alignment mark (through wafer) in the Y microlens scanner chip and the positive alignment mark on the aperture chip. Epoxy glue is applied at the edge of the chip. Finally, the X microlens scanner is stacked on top of the Y microlens scanner with a horizontal offset of 2 mm, leaving electrical connections for Y microlens scanners open. Epoxy glue is applied to the edge of the three chips and wires are bonded between the X and Y microlens scanner chips and aperture chip. This offset stacking method described in the previous section makes it possible to use same SOI microlens scanner chip as X and Y microlens scanner with different lens focal lengths. The picture of the transmissive scanning confocal head is shown in Figure 58. More than 15 transmissive confocal scanning microscopes are fabricated with the dimension smaller than 1 cm^2.
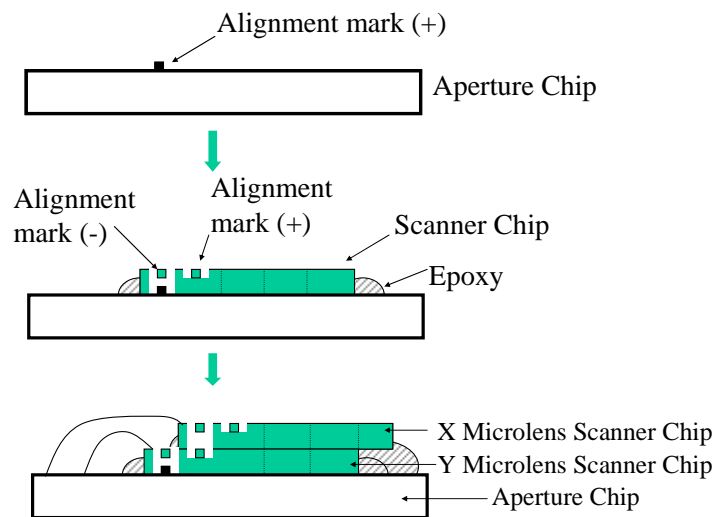
Figure 57. Assembly sequence of a transmissive scanning confocal microscope.
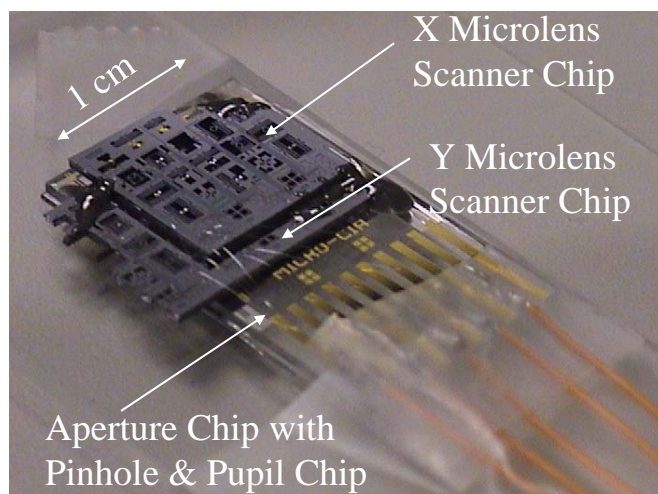
Figure 58. Photograph of a microfabricated transmissive scanning confocal head.

4.2.3 MINIATURIZED TOTAL INTERNAL REFLECTION SYSTEM

Figure 59 shows a schematic cross section of the Miniaturized Total Internal Refection (MTIR) system and the path of a light beam as it passes through the system. A polymer-filled cavity and its micromirror sidewall were implemented to direct the excitation light beam at an angle above the critical angle on the glass-liquid interface. The geometry of such a micromirror made it possible to vertically integrate a light source directly below the micromirror without the need for any additional external optics. More importantly, this design eliminated the need to align the system with a light beam at the desired angle. The angle of the tilted micromirror was accurately defined by the microfabrication process (54.7° for standard KOH etch of a {100} silicon wafer), which can be changed by properly selecting polymers of different indexes of refraction. Dynamically changing the incident angle [93] is not an advantageous feature for lab-on-a-chip applications, since it would require the use of a complex optical and mechanical configuration and the interaction of the end-user with the system.
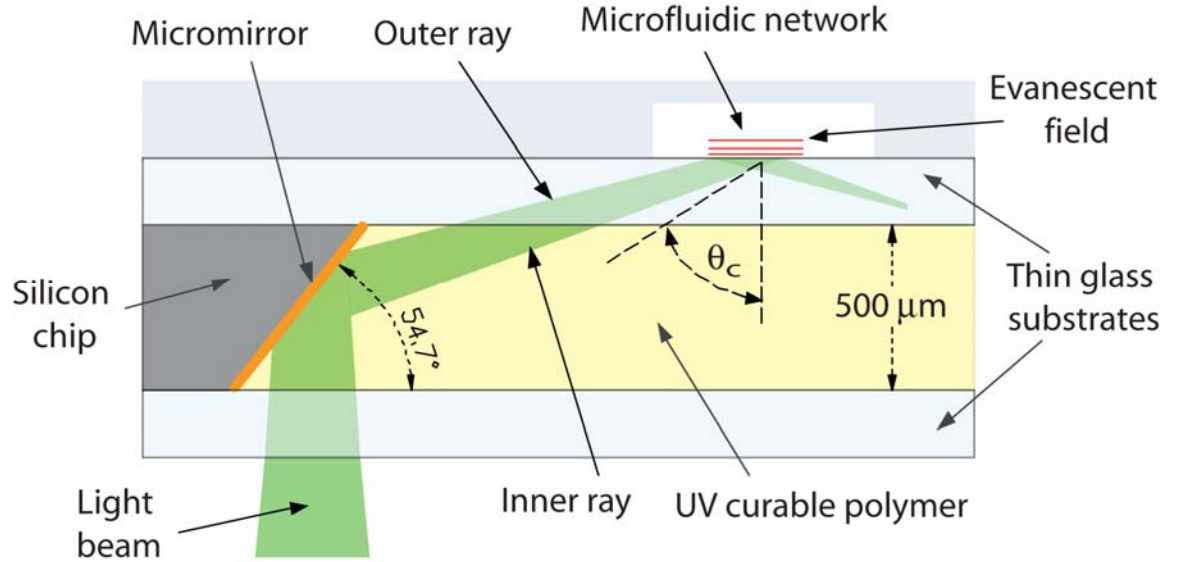
Figure 59. Schematic cross-section of the four layer chip.

The chip consists of four substrates stacked together. A silicon substrate (Table X) that contains the micromirror, sits between two thin (~200 µm) glass (AF-45, index of refraction n_1=1.526) wafers. The cavity that was formed between the two glass wafers and the micromirror surfaces was filled with a transparent UV curable polymer (Norland Optical Adhesive 65, index of refraction n_2=1.524) that couples the exciting light into the system. The UV curable polymer was an essential component for efficient optical coupling, minimizing the reflectance losses to less than 5%. The top glass wafer served as the functional substrate where TIR takes place, while the bottom one was used to planarize the UV curable polymer. The light beam was weakly focused on the interface, where it totally internally reflected, and created the evanescent field.

X. Fabrication of the Self-aligned Integrated Microfluidic Optical System

Step	Process
1	One micron of low stress silicon nitride (LSN) was deposited on a {100}-oriented, 500 microns thick, double-polished silicon substrate.
2	A silicon nitride film was photolithographically patterned, and the wafer was then immersed in a 2:1 KOH solution to obtain the 54.7° silicon tilted walls. The suspended nitride membrane that remains at the end of the wet etch process was subsequently broken and removed with a blast of compressed air.
3	A 0.3 µm thick layer of chrome/gold was then electron-beam evaporated to achieve the reflective mirror surface.
4	The silicon substrate was inverted and placed upside-down on the top glass substrate. The formed cavity was filled with the UV curable polymer. The bottom glass substrate was placed on top of this assembly, enclosing the cavity. The polymer was fully crosslinked with UV light exposure for 10 min with a 100 W ultraviolet lamp (Spectroline, SB 100P). This step both cured the polymer in the cavity and bonded all three wafers together.

5	The microfluidic network was formed from a PDMS (polydimethylsiloxane) slab patterned from an SU-8 mold. The mold was created by spin casting and patterning a 13 μm layer of SU-8-2010 on a bare silicon wafer. The PDMS pre-polymer mixture was cast over the mold and cured on a hot plate for 15 minutes at 150° C.
6	After curing, the PDMS replica was peeled off from the mold, treated with oxygen plasma (30 s, 30 W at 1 Torr) and irreversibly attached on top of the top glass substrate to seal the chip.
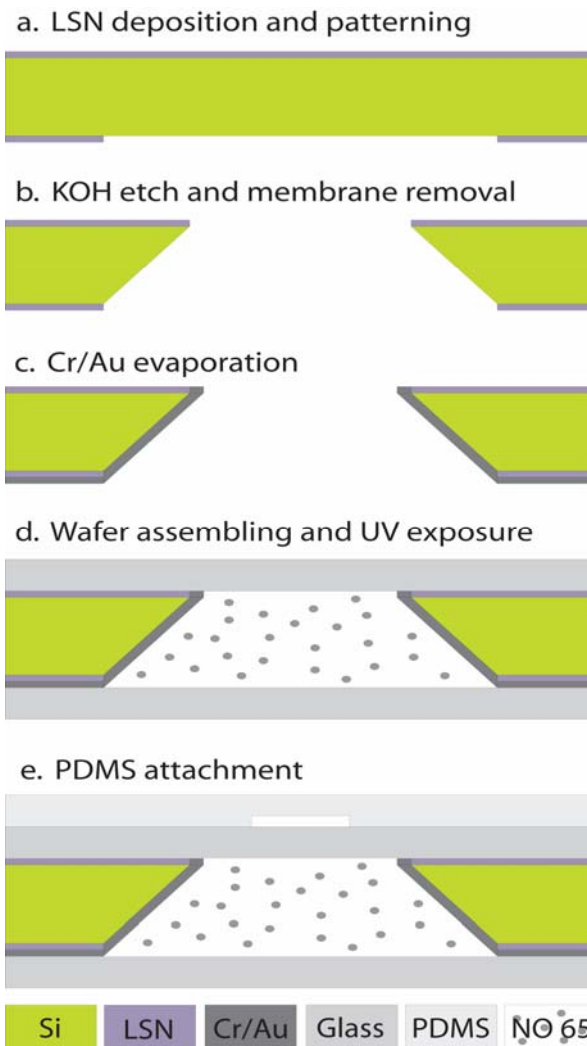
Figure 60. The fabrication process of the biochip (a) Low stress silicon nitride (LSN) deposition and patterning, (b) backside KOH etch and front side silicon nitride removal, (c) chrome/gold deposition, (d) wafer assembly through the UV curable polymer and (e) PDMS attachment.

4.2.4 SELF-ALIGNED INTEGRATED MICROFLUIDIC OPTICAL SYSTEM (SIMOS)

A disposable Self-aligned Integrated Microfluidic Optical System (SiMOS) was realized by integrating microlenses with microfluidic channels for fluorescence amplification as shown in Figure 59. The planar microlenses and the excitation light of the LED resulted in an optical axis parallel to the plane. The excitation light was condensed through the planar microlenses and focused to a detection point in the microfluidic channel. Thus, emitted fluorescence was collected by the detector from the microfluidic channel.
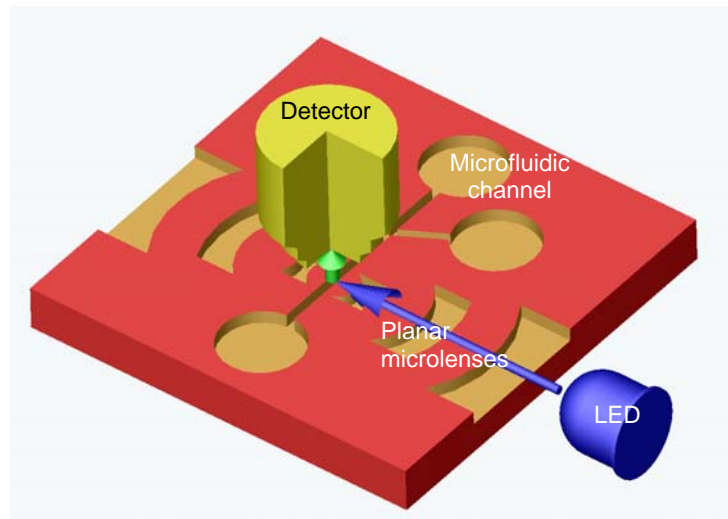
Figure 61. Self-aligned 2-D compound microlenses on a microfluidic channel.

Table XI. Fabrication of SiMOS.

Step	Process
1	A silicon mold was prepared using a deep reactive ion etching (DRIE) method.
2	A 2 μm thickness photoresist layer was coated and patterned for an etching mask layer. The photo-patterned substrate was etched to a depth of 110 μm by DRIE.
3	After the mask layer was removed, the mold was dipped into a silicon etching solution which had an etch rate of 1500 Å/min for single crystal silicon [85]. Rinsing and drying the mold was followed the etching process.
4	After the base and curing agent of PDMS were mixed at a 10:1 volume ratio, the mixture was uniformly coated on the mold. It was cured thermally at 70 °C for one hour.
5	Each device was mechanically detached and treated by an O_2 plasma to render the surfaces hydrophilic
6	The treated devices were bonded to pre-cleaned glass-substrates.

Disposable SiMOS's were fabricated by using the PDMS (Sylgard 184, Dow Corning) molding techniques shown in Figure 60 and described in Table XI. Scanning

electron microscopy (SEM) micrographs of fabricated devices are shown in Figure 61. The orthogonal arrangement of excitation source and detector is schematically illustrated in Figure 59. The excitation source was a blue light emitting diode (LED) (Hosfelt®, peck wavelength 466 nm). The range of the applied voltage was 3.5 to 3.7 V. An objective lens, a charge-coupled-devices (CCD) camera, and a spectrometer were used to analyze the fluorescent signals for the purposes of spectrum analysis and imaging. The excitation by the LED was characterized with a 40 nm fluorescence dye (Flurosphere®, 505 nm excitation/515 nm emission) in s channel which had the dimensions of 200 μm (width) $\times$ 110 μm (depth). The original 5% solid concentration of the fluorescent dye was diluted to 2.5 % and 0.5 % solid concentration with deionized water. All solutions were kept in the dark at 4 °C before being used in the experiments.
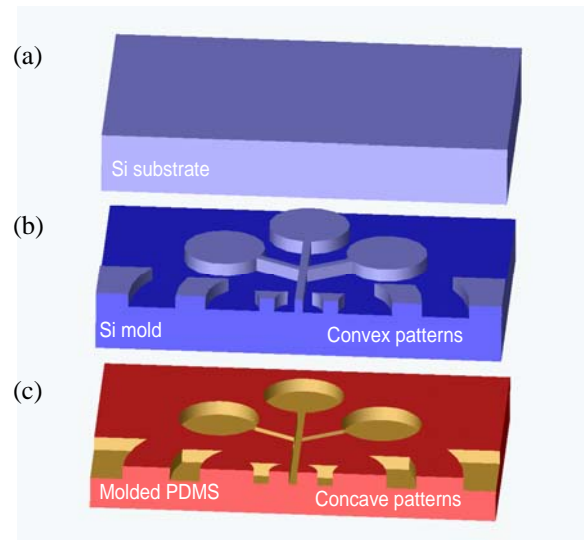
Figure 62. Schematic fabrication process of a disposable integrated microfluidic optical system.

(a) Si substrate, (b) Deep reactive ion etching to make a mold, and (c) PDMS molding.

Since the planar integration of the planar microlenses did not need multi-layer processing, this fabrication process was much simpler than alternative fabrication methods for this type of system.
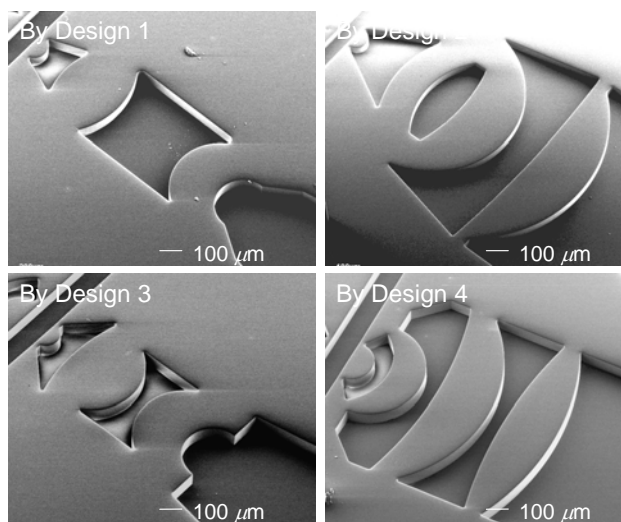
Figure 63. Fabricated high NA planar microlenses using PDMS molding.

5.   RESULTS AND DISCUSSIONS

The results of the system components and the microscaled systems are presented.

5.1 SYSTEM COMPONENTS

The system components that are discussed include the scanners, the variable focus liquid lenses, and the polymer microrobotic system for single cell manipulations.

5.1.1 SCANNERS

The results of the stacked 2-D microlens scanners, the vertical microlens scanners, the Gimbaled 2-D scanners, and the self-aligned vertical comb-drives are presented.

5.1.1.1 STACKED 2-D MICROLENS SCANNERS

The optical characteristics and the mechanical characteristics of stacked 2-D microlens scanners are presented. Also, 1-D and 2-D scans are discussed, as well as fluorescent cellular imaging.

5.1.1.1.1 Optical Characteristics
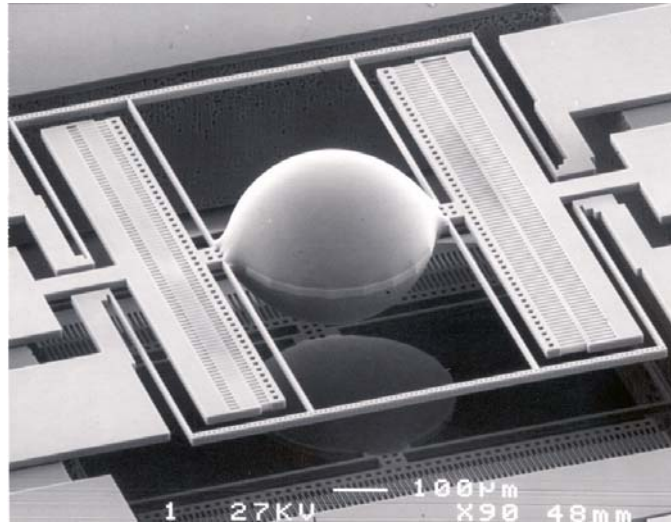
Figure 64. SEM micrograph of a fabricated 2-D microlens scanner.

Two vertically cascaded microlenses that were actuated by electrostatic comb-drive actuators aligned in the orthogonal direction, and which raster-scanned and focused light. Note the outer diameter of the microlens was 400 μm.

The SEM micrograph presented in Figure 64 is a fabricated and assembled stacked microlens scanner. Two 1-D microlens scanners were orthogonally aligned and vertically stacked. The focal length of the polymer microlens was measured using a

motorized stage with a digital readout and a microscope with a charge coupled device (CCD). A collimated He-Ne laser beam was focused by the microlens, and a microscope imaged the focal spot. The axial distance between the surface of the actuator and the minimum focal spot was determined by moving the microlens scanner along the optical axis with a digitized motorized stage. The diameter of the ring shaped lens holder, the injection pressure and the glass capillary diameter were 400 μm, 10 *psi*, and 10 mm, respectively. As injection time increased, the injected volume of the polymer increased, and the focal length of the fabricated microlens decreased. Microlenses with focal lengths from 300 μm to 1mm were easily fabricated on released actuators. The uniformities of the microlenses were 10% for the lenses with small injection time ($<$ 3 seconds) and 4% for the large injection volume ($>$ 4 seconds). From these results, the desired injection time was estimated to make a specific focal length. For stacked microlens scanners, microlenses with focal length of 956 um and 495 um were fabricated within 5 % errors.

The profiles of fabricated biconvex polymer microlenses were measured using a white light interferometer (Wyko^{TM}, Veeco Inc.), as shown in Figure 65 (a). Because the surface tension of the liquid phase polymer induced the surface profile, parabolic surface profiles were achieved on the lens holder. The measured profile of a microlens and its deviation from an ideal sphere are shown in Figure 65(b). The deviation from an ideal circle was less than 1μm inside the pupil of the lens holder. The lens profile outside the pupil had a larger deviation than the center of the lens due to the interaction with the lens holder surface. Because the lens worked as an embedded pupil and blocked the rays at the edge of the lens, as illustrated by the dashed circle in Figure 65(b), this did not affect the actual system performance. The volume of the polymer droplet and the dimensions of the ring shape lens holder determined the focal length. This was estimated before fabrication in the same way shown as shown in [94]. The measured polymer lens was 400 μm wide and 84 μm thick, resulting in a high numerical aperture of 0.39.

(a)

(b)
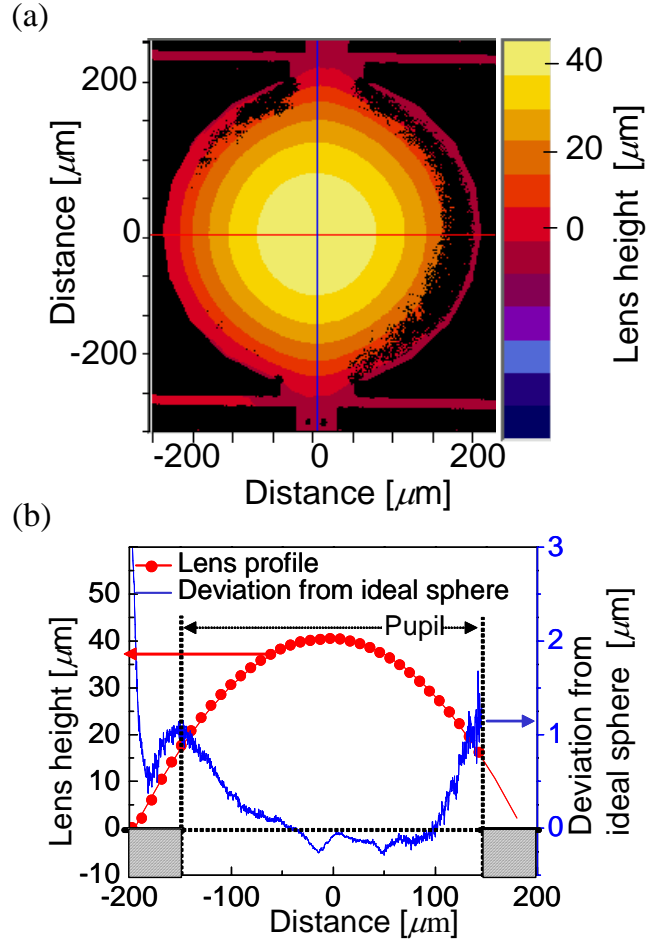
Figure 65. Surface profiles of a polymer microlens (a) Interferometic profile and (b) Profile and deviation from an ideal sphere.

5.1.1.1.2 Mechanical Characteristics

The dynamics of the bottom Y microlens scanner were characterized with a Microvision Stroboscopic Motion Analysis System [95].
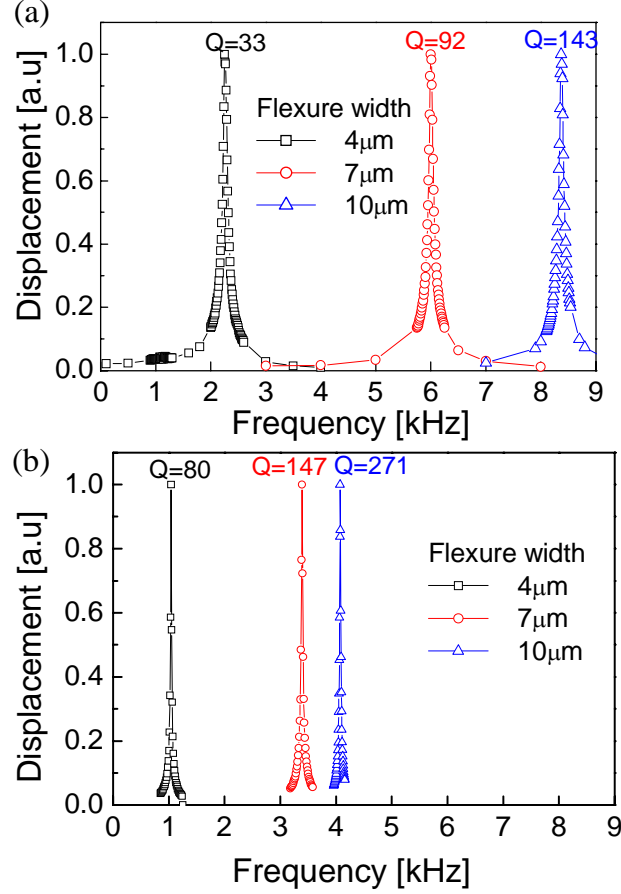
Figure 66. Frequency responses of microlens scanners with different flexure widths: (a) before lens fabrication, and (b) after lens fabrication.

Microlens scanners with three different flexure widths were fabricated to control the resonance frequencies. The lengths of the flexures were 500 μm. Figure 66 shows the frequency responses of the microlens scanners with flexure widths of 4 μm, 8 μm, 12 μm before and after lens fabrication. Resonance frequencies from 2 kHz to 10 kHz were measured. To increase the resonating speed of the Y microlens scanners, smaller lenses with long focal length were required. This was easily accommodated with this optical doublet design.

The quality factor, Q, was defined by the equation $Q = \sqrt{Mk}/c$, where M, k, and c are the mass, the spring constant, and the viscous damping coefficient of the system, respectively. Noticeably, Q increased after lens fabrication because M was increased by the increased mass of the lens. The opened backside optical window, c, was negligible. The optical window reduced the viscous damping so that the microlens scanner achieved high Q's of around 100 in air. The maximum ratio of the resonant frequencies between scanners was about 5, which allowed 5 horizontal lines for a frame rate of 1 kHz using the Lissajous Scanner. The X microlens scanner was operated in the static actuation mode with a large static displacement. Figure 67 shows the measured DC characteristics

of the X and Y microlens scanners with flexure lengths of 800 μm and 500 μm. Maximum displacements longer than 50 μm were achieved for a single side actuation, which resulted in 100 μm ($\pm$50 μm) for double side actuation. The measured data was fitted to an ideal quadratic equation.
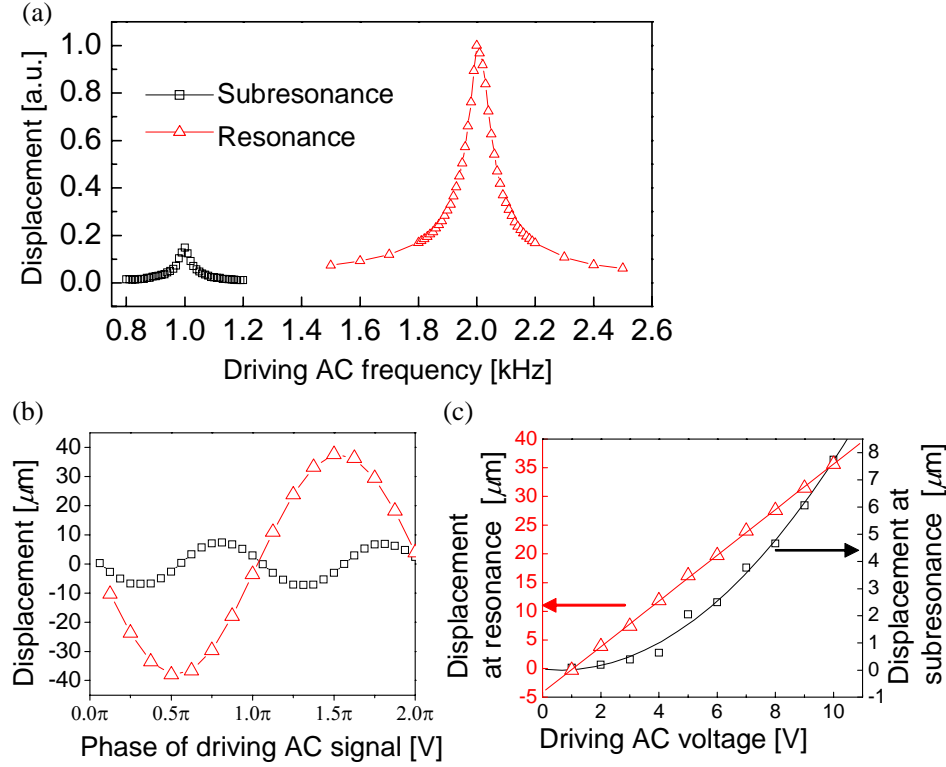
Figure 67. Resonances and sub-resonances verse scanning range control.

(a) Typical frequency response of a microlens scanner, (b) Displacement of the actuator with respect to the driving signal phase, and (c) Amplitude modulation characteristics for sub-resonance and resonance.

The scanning range of the microlens scanner in resonance was linearly controlled by AC amplitude modulation. However, a careful examination of the frequency responses was required. High actuation voltages were needed, since large AC actuations were often required to actuate the silicon-on-insulator (SOI) comb-drives, which had high spring constants. Second harmonics were often the result of large AC voltages, which are thought of as actuator sub-resonances. Figure 67(a) shows a typical frequency response of a microlens scanner with two resonant peaks [96]. The first sub-resonance was at one-half of the natural frequency of the scanner. The large resonance peaks were the natural frequencies of the scanners. For linear scanning range control, proper biasing and amplitude modulation of the driving signal were required. The electrostatic driving force, F, in Equation (19) consisted of two harmonics, where n, d, ε, h, and V denote the number and gap size of comb-teeth, dielectric constant of air, thickness of the SOI device layer, and applied voltage, respectively.

$$F = \frac{n\varepsilon h}{d}V^2 = \frac{n\varepsilon h}{d}(V_{AC}\cos\omega t + V_{DC})^2$$

$$= \frac{n\varepsilon h}{d}(\frac{V_{AC}^2}{2}\cos 2\omega t + 2V_{DC}V_{AC}\cos\omega t + \frac{V_{AC}^2}{2} + V_{DC}^2)$$

(22)

Except when the amplitude of the driving AC voltage (V_{AC}) was negligible, the driving signal contained harmonics at ω and 2ω. The first term is the second harmonic of the driving AC signal. Due to the harmonic, even when the driving AC frequency was zero or one-half of the resonant frequency of the structure, the second harmonic excited the natural frequency of the scanner, resulting in a sub-resonance peak, as shown in Figure 67(a). Because of the first term, the scanner actually moved at twice the driving frequency at sub-resonance, while the scanner moved together with the driving signal frequency at resonance (Figure 67(b)). From the equation, the scanning range was quadratically proportional to V_{AC} at sub-resonance, while it was linearly proportional to V_{AC} at resonance with a fixed DC bias. Figure 67(c) shows the measured linear and quadratic amplitude responses in resonance and sub-resonance, respectively. Considering the linearity of the amplitude response at resonance, the resonance mode with a fixed DC bias (the second term in the equation) was used. Resonance scanning distances of longer than 100 μm were measured.

5.1.1.1.3　　　1-D Line Scanning and 2-D Scanning

1-D line scanning of focused light using a single microlens scanner is shown in Figure 68. A maximum line scanning of the focused laser spot of up to 100 μm was measured in the focal plane at 370 μm from the scanner, which resulted in a corresponding scan angle of 15° when the 1-D microlens scanner was activated with 4.5 kHz AC, a driving voltage of 10 V, and a 20 V DC bias. The estimated number of resolvable pixels for the 1-D microlens scanner, based on the measured spot size of 1.6 μm, was 115 at a wavelength of 633 nm.
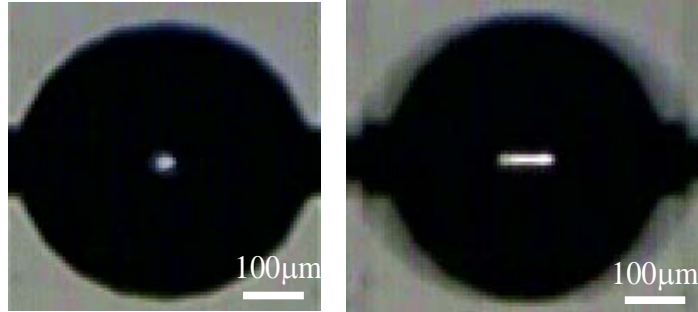
Figure 68. Transmission microscope photograph of a 1-D microlens scanner without actuation (left) and with 1.1 kHz actuation.

Line, raster and Lissajous scanning patterns were demonstrated for the 2-D scanning of a focused laser using the stacked 2-D microlens scanner shown in Figure 69. Scanning patterns were imaged using a microscope in the focal plane of the stacked microlens scanner. The device dimensions were $F_1 = 956\ \mu m$, $F_2 = 550\ \mu m$, $T_1 = 1.5$mm, $T_2 = 0.5$ mm, $WD = 220\ \mu m$, $D_p = 20\ \mu m$, and $D_{1,2} = 400\ \mu m$. Figure 69 shows the focus of the light with no movement (upper left), the Y microlens only resonating (upper right), the Y microlens resonating and X microlens actuated at off-resonance (lower left), and both the X and the Y microlenses scanner resonating. A more than 100 μm by 100 μm scanning range was demonstrated at a working distance of 220 μm and with an effective focal length of 500 μm, which resulted in a larger field of view and optical scanning angles that were greater than 10° by 10°.
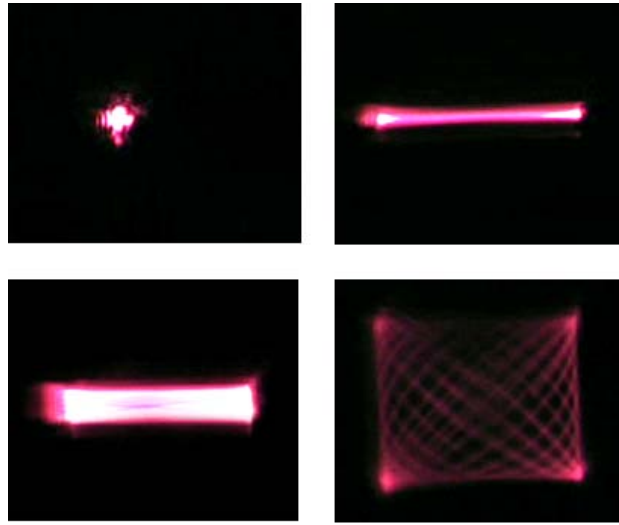
Figure 69. 2-D microlens scanner.

No movement (upper left), resonating Y microlens (upper right), resonating Y microlens and X microlens at off-resonance (lower left), and both X and Y microlenses resonating (bottom right).

5.1.1.1.4 Fluorescent cellular imaging using a 1-D microlens scanner

To demonstrate the bifunctionality of this device as both an imaging objective and as a scanner, a cellular imaging experiment was performed using a 1-D microlens scanner and external optics. The experiment setup is shown in Figure 70. The microlens scanner was placed between the external optics and the cell sample. A *Convallaria majalwas* plant cell was dyed with fluoroscein isothiocyanate /tetramethylrhodamine isothiocyanate (FITC/TRIC) and used as the sample. An Argon laser with a wavelength of 433 nm was used as light source. Because light from an external microscope was refocused by the microlens, which had a smaller numerical aperture, the imaging objective in this setup was the microlens scanner. The imaging resolution was determined by the microlens. The scanning range in this experiment was 15 μm, which was less than 5% of the lens diameter. The results of fluorescent cellular images from this imaging experiment setup are shown in Figure 71.

The cells were scanned by two external scanners though the microlens scanner without device actuation (Figure 71 (a)). In this case, the microlens scanner was an imaging objective lens. The 2µm-thick cellular membrane sample was resolvable using the microlens as an imaging objective lens. Then the external scanner for the Y direction was turned off and the microlens scanner was actuated in Y direction to test the scanning function of the device. Comparisons can be made between the images scanned by external X and Y scanners (Figure 71 (a)) and the second image scanned by external X scanner with the microlens Y scanner (Figure 71 (b)). The periodic image was from the device actuation. The image scanned by microlens scanner can exactly fit into the image acquired with external scanners.
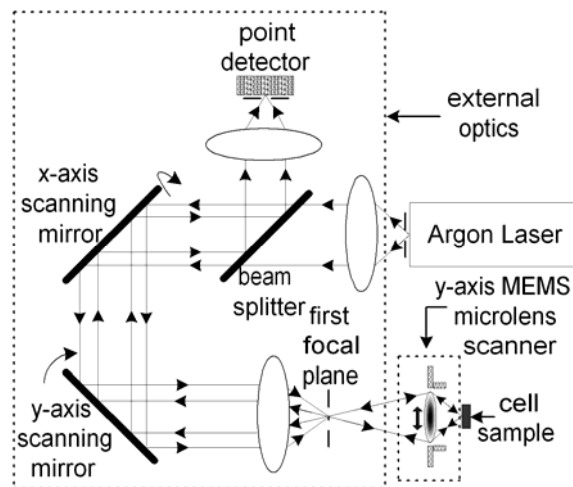
Figure 70. Experimental setup for fluorescent cellular imaging using a 1-D microlens scanner.
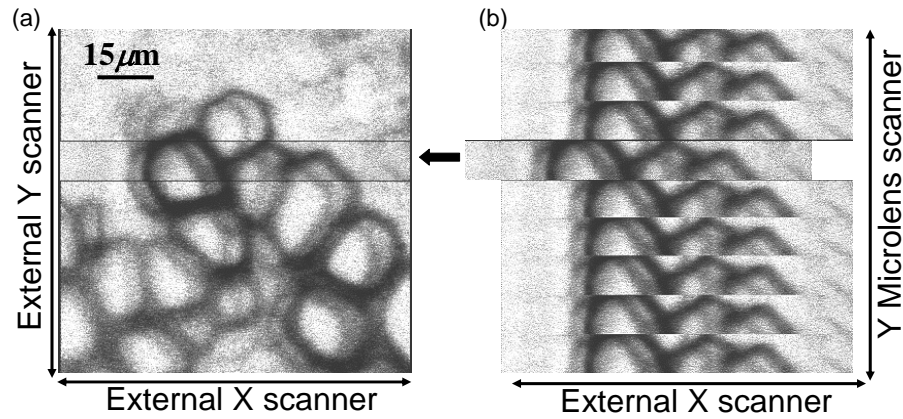
Figure 71. Results of florescent imaging using the microlens scanner.

The microlens scanner was used as an imaging objective lens. (a) Scanning was done by two external scanners. (b) Microlens scanner was as Y scanner instead of an external scanner.

5.1.1.2   VERTICAL MICROLENS SCANNERS

The vertical scanners consisted of three major units: a lens frame, coupled torsion flexures, and isolated comb-banks. Figure 72 shows the left half of the bidirectional device. The lens frame consisted of a ring-shaped lens holder for the microlens integration and a frame for placing flexures and comb-banks. The inner and outer diameters of the ring-shaped lens holder were design parameters related by the required numerical aperture and entrance pupil size.
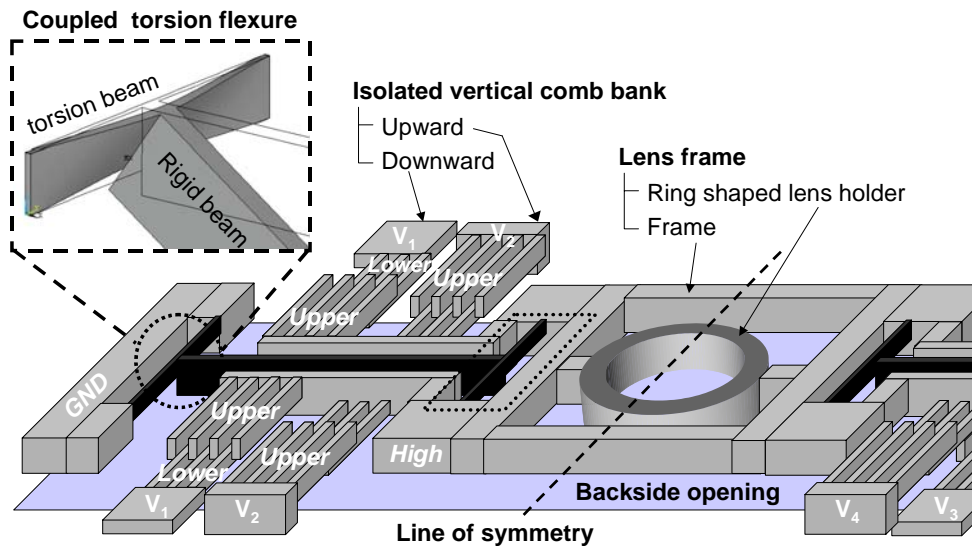
Figure 72. Schematic drawing showing the left half of a high aspect ration vertical actuator based on isolated vertical comb-drives for bi-directional piston motion.

87

Two coupled torsion flexures were connected to both ends of the lens frame. The coupled torsion flexure was a set of two torsion beams in the *Upper* layer connected by a rigid beam in the *High* layer as shaded in Figure 72. When the lens frame was actuated upward and downward by the electrostatic force generated by the vertical comb- drives, four torsion beams in the two coupled torsion flexures were twisted, but not bent, by the rigid connecting beams. In effect, this was a compliant torsion design for the difficult out-of-plane bending of the high aspect ratio thick beams. This attractive flexure design maximized the vertical compliance at low voltage actuations. According to simulations, the coupled torsion flexure was 80 times more compliant than double folded flexures [97] of the same length. In addition, the small lateral bending of the upper torsion beams provided the elongation needed in the vertical displacement to prevent nonlinear increases in vertical spring constant.

The isolated comb-drive bank was a set of upper and lower comb-fingers defined in the *Lower* and the *Upper* layers with 10 µm of pre-engagement, initial overlap between the upper and lower comb-fingers. Because both comb-fingers were fabricated in the SOI device layer, isolation between comb-banks was achieved monolithically, which allowed independent actuation between the comb-fingers for bidirectional motion and tilting compensation. Figure 72 shows the schematic of the four isolated comb-drive sets with control voltages V_1 though V_4. The right side of the line of symmetry had comb-banks controlled by V_3 and V_4. The device was grounded through flexures. Normal upward motion was powered by V_2 and V_4, while downward motion was powered by V_1 and V_3. The unidirectional device was the same as the bidirectional device, except that its comb-banks were only used downward motion and there were twice as many. Tilt compensation for extreme accuracy was possible with the independent control of V_1 - V_4. Applying an additional DC voltage to the other side of the line of symmetry compensated for the tilt in that line of symmetry axis. To get large displacements at low driving voltages, the area of comb-banks at a given device size was increased, which also minimized the in-plane rotational instability. This in-plane instability, which was determined by the ratio of the vertical stiffness to the in-plane rotational stiffness, limited the maximum extension of the comb-banks. Therefore, comb-banks were placed close to the coupled torsion flexures by placing the torsion beam inside the frame, as shown as the dashed box in Figure 72.

5.1.1.2.1 Static and Dynamic Characteristics

Static and dynamic characteristics of the vertical microlens actuator were measured using a Laser Doppler Vibrometer. Figure 73 shows the static vertical displacement for both the unidirectional and bidirectional vertical microlens scanners.
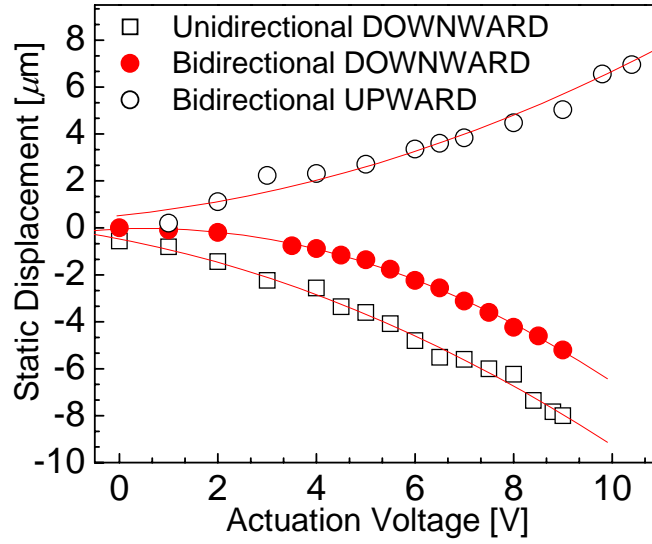
Figure 73. Vertical displacements of the unidirectional and bidirectional vertical microlens scanners.

The devices had large vertical displacements of up to ±10 μm at sub-10 V driving voltages. This featured low voltage actuation was due to compliant coupled torsion flexures, pre-engagement of vertical comb- fingers, and high density comb- banks enabled by the buried design of the coupled flexure, which allowed more area for comb-drives. Bidirectional actuation enabled by the isolated comb- banks doubled the maximum possible displacement compared with the unidirectional actuation. At its resonance near 400 Hz, the maximum displacement was 55 μm, and the scanning range control using linear amplitude modulation was measured (Figure 74). The frequency responses for before and after lens fabrication, along with the DC bias effect, were measured using a laser vibrometer and a lock-in amplifier, as shown in Figure 75. The resonant frequency after microlens integration was measured to be 10 % lower due to the added mass of the lens. When comparing the frequency response for 10V and 8V DC bias, the DC bias effect on resonance frequency was less than 5%.
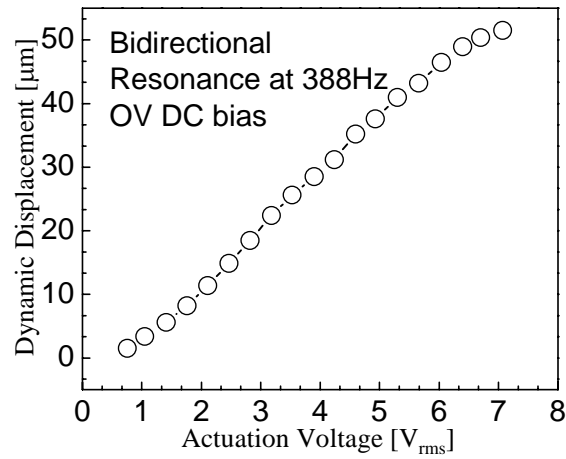
Figure 74. Vertical displacement controlled by amplitude modulation of the actuation voltage.
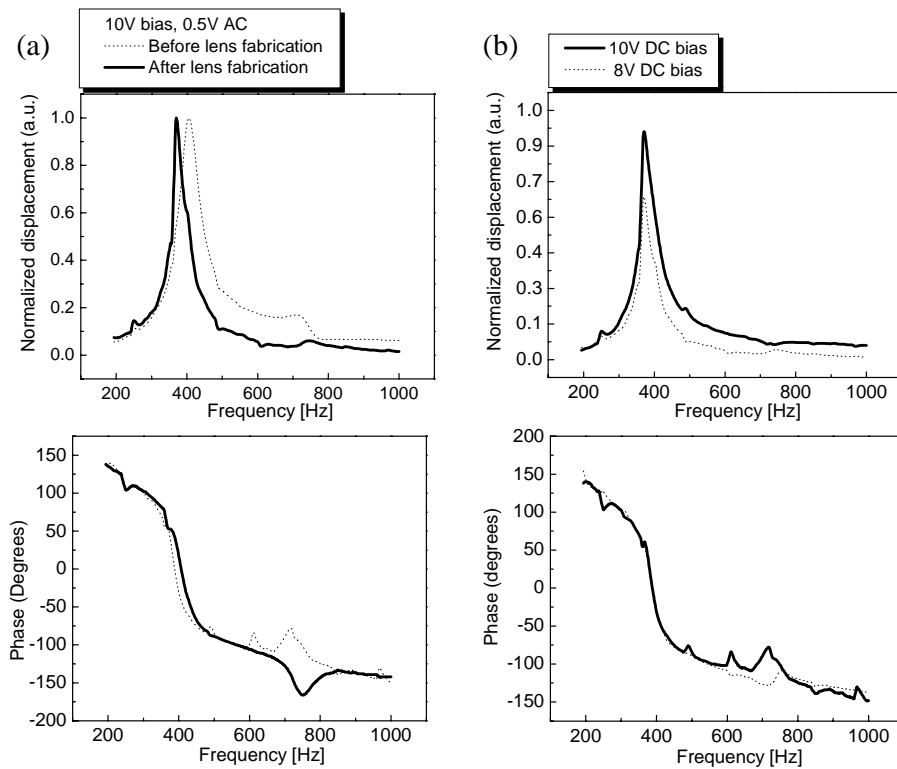
Figure 75. Frequency response of the vertical microlens actuators.

(a) Before and after lens fabrication, and (b) DC bias effect on resonance frequency.

5.1.1.2.2 Tilt Compensation

Any imperfections and asymmetries in the fabrication could result in undesired tilting of the lens plate during actuation. This aspect of the devices was measured using an interferometric profiler. The measured tilting of the frame with respect to static actuation voltage was shown in Figure 76 (a). The maximum measured tilting during piston motion in the X-X' axis was only 0.034° at 10 V. One-tenth of that tilt was in the Y-Y' axis. Pure piston motion with this negligible tilting angle was enough for most applications. However, compensation to zero tilt was also possible for applications requiring extreme accuracy by using asymmetric driving using these featured isolated comb-banks. To demonstrate the compensation capability of these isolated comb-banks, the X-X' axis tilting was determined by applying an asymmetric voltage (V_1, and V_2) to either side of the line of symmetry. The compensation result, which was the profile along the X-X' axis, was shown in Figure 76 (b). The rectangular-marked profile represented the symmetric actuation with 10 V, and the tilt of the lens frame was determined to be 0.034°. The tilt was compensated to 0.0013° by applying asymmetric actuation voltages of 10 V and 11.456 V to the electrodes V1 and V2, respectively. Theoretically, perfect dynamic tilting compensation was possible using this technique.
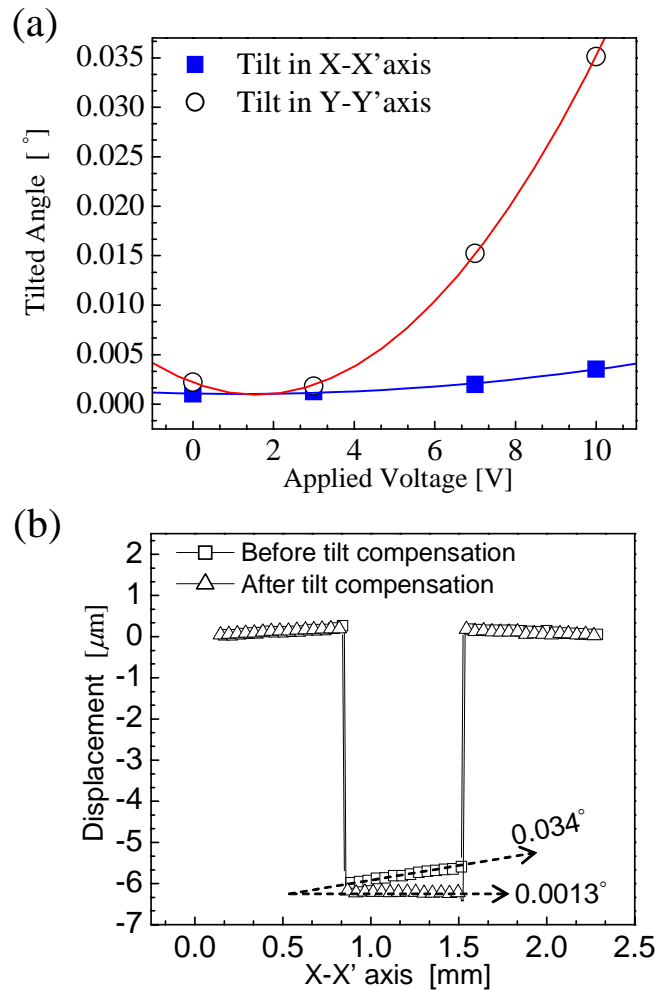
Figure 76. (a) Measurements of the tilt of the frame and (b) Tilt compensation by asymmetric driving voltage.

Tilt was reduced from $0.034°$ to $0.0013°$ after compensation.

5.1.1.3 GIMBALED 2-D SCANNER USING A BACKSIDE ISLAND

5.1.1.3.1 Two-Axis Gimbaled Mirror

SEM micrographs of the fabricated device are shown in Figure 77. The mirror, gimbal, and vertical comb- drives are shown in Figure 77 (a). The configuration of vertical comb-banks allowed bidirectional rotation of the gimbal and unidirectional rotation of the mirror. The dashed rectangle is the location of the backside island, which is hidden beneath the gimbal. Figure 77 (b) is a SEM micrograph of the backside island taken from below. The backside island was attached underneath the gimbal, and the mirror was anchored to the backside island. The buried oxide was sandwiched between the mirror and the backside island, allowing the mirror to be electrically isolated. Also, the mirror and gimbal were isolated by trenches around the mirror. In this way, different

92

actuation voltages can be applied. The vertical comb-banks and the torsion beam of gimbal from a similar device are shown in Figure 77 (c). The *Up-combs* and *Down-combs* pulled up and pushed down the gimbal, respectively, resulting in a counter clockwise rotation.
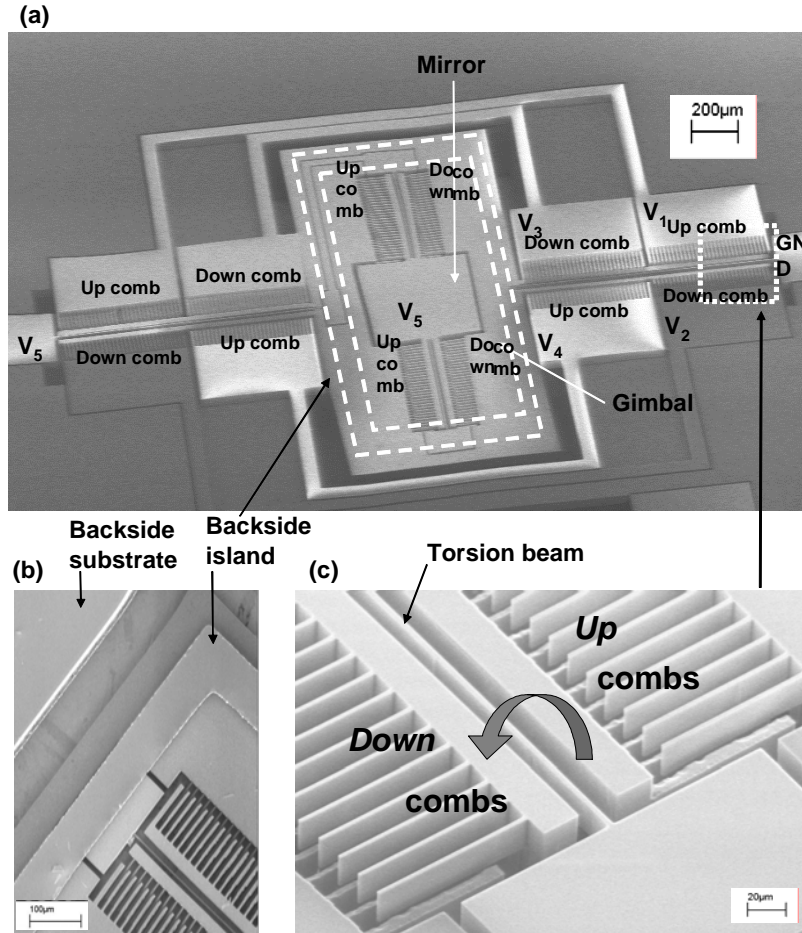
Figure 77.   SEM micrographs of 2-DoF gimbaled micromirror.

(a) Using SOI (top view), (b) Backside island (bottom view) and (c) Vertical comb-drives and torsion beam

5.1.1.3.2 Two-Axis Gimbaled Mirror with Piston Motion

Another micromirror with reduced gimbal area and piston motion capability was shown in Figure 78. Instead of using electrodes for the bi-directional actuation of the outer gimbal, electrodes for piston motion were added to the device. Piston actuation (pure vertical actuation) ranging from -7 μm to +7 μm was demonstrated with a voltage smaller than 100V. The isolation trench that isolated the mirror and gimbal was clearly shown in the figure. The mirror potential (V_5) was applied through one of the gimbal's torsion flexures.
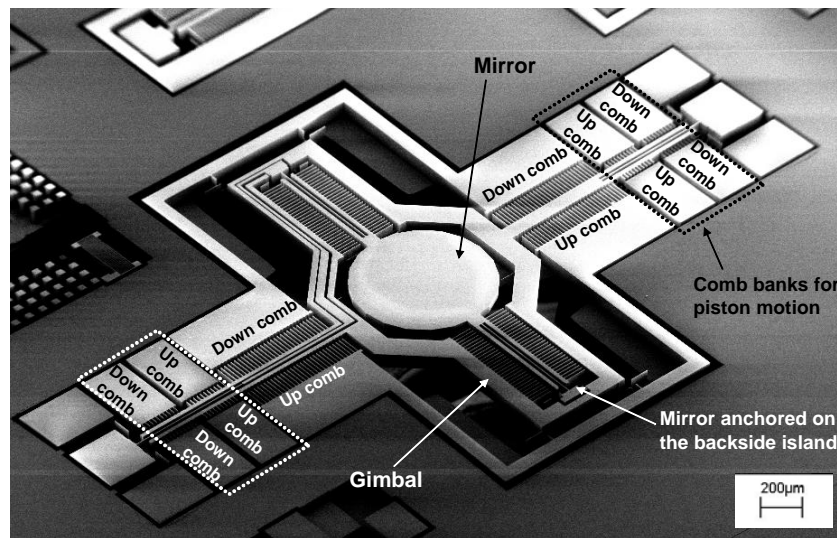
Figure 78.   SEM micrograph of the second version of the 2-D gimbaled micromirror.

The gimbal was minimized and electrodes for piston motion of the micromirror were added.

5.1.1.3.3 Bidirectional Static Rotation and Resonant Frequencies

Figure 79 shows typical experimental DC deflection characteristics for the gimbal and mirror. The gimbal was rotated from -23° to 23°, resulting in a maximum optical static scan angle of 46°. Both clockwise (CW) and counter clockwise (CCW) rotation were demonstrated. Activation of electrode V_1 and V_2 resulted in CW rotation of the gimbal, and activation of V_3 and V_4 rotated the gimbal in CCW direction. The maximum static scan angle for the mirror was 15°, as shown in Figure 79. This bi-directional actuation capability resulted from the isolated vertical comb-banks. Because the number of torsion flexures of the gimbal was limited, mirror rotation was limited to unidirectional static actuation. The typical mirror mechanical characteristics are shown in Table XII. The penalty of using backside island isolation was the increased mass of the gimbal, but was still useful for raster scanning applications since the gimbal was usually actuated at an off-resonant frequency.

(Voltage sign*)(Voltage squared) [V²]
* Voltage sign is positive for the voltage applied to electrode V_1 and V_2, and is negative for the voltage applied to electrode V_3 and V_4.
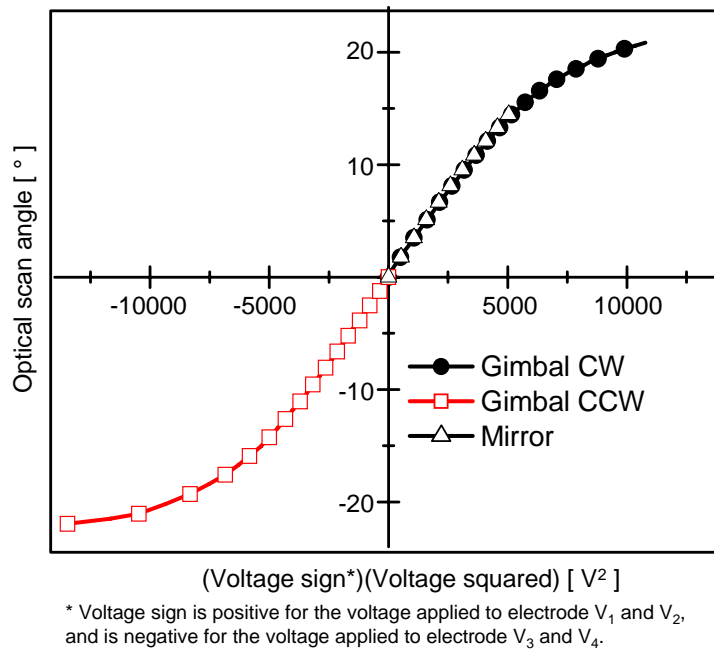
Figure 79.   The static actuation characterwastic of the gimbaled micromirror.

The gimbal was actuated in both CW and CCW directions.

Table XII. Summary of actuation characteristics of a gimbaled mirror

Mirror elements	Resonant Frequency [Hz]	Q	Maximum static optical scanning angle [°]	Actuation direction
Mirror	2248	58	15	Uni-direction
Gimbal	182	28	46	Bi-direction

5.1.1.3.4 Two-Dimensional Static Beam Pointing and Raster Scanning

The results of the demonstration of laser beam scanning are shown in Figure 80. In this experiment, the mirror and gimbal deflected the laser beam in the horizontal and vertical directions, respectively. The spots in Figure 80 (a) were from DC static actuation. The rectangular beam scanning pattern in Figure 80 (b) was from raster scanning that was generated from resonating the mirror at 2.2 kHz with an off-resonance gimbal actuation at 30Hz.
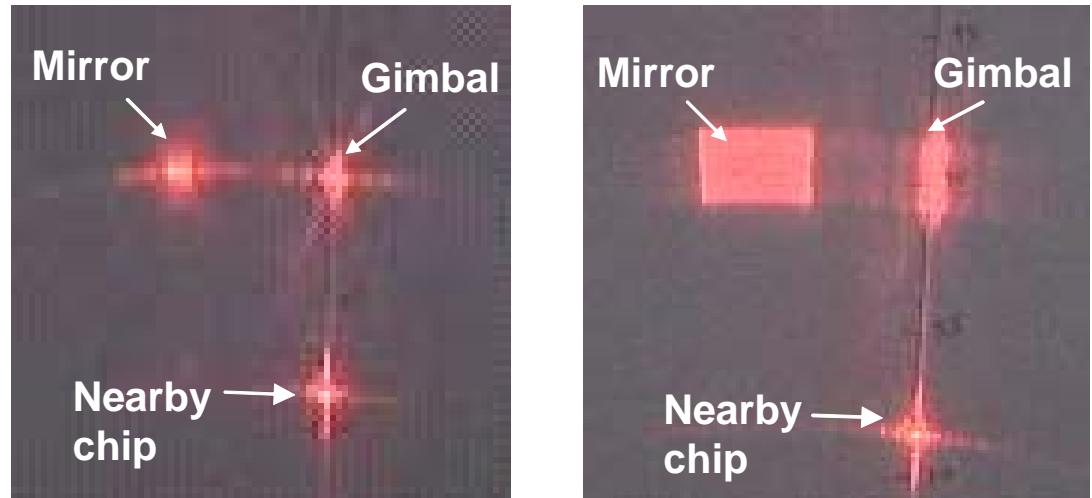
Figure 80. Demonstration of static 2-D steering (left) and raster scanning (right) of the laser beam.

The label denotes the structures that each laser beam was reflected from.

5.1.1.4   SELF-ALIGNED VERTICAL COMB-DRIVES

The mechanism of vertical offset between fixed comb and movable comb was based on residual stress. As illustrated in Figure 81, the fixed combs were anchored to bimorph-cantilevers made of two materials with dissimilar thermal coefficient of expansion (TCE), i.e., silicon dioxide and single crystal silicon. The deflection of a cantilever provided the vertical offset between fixed and movable combs, which was

caused by the residual stress generated within the TCE mismatched layers during the cooling down process from the oxidation temperature to room temperature.
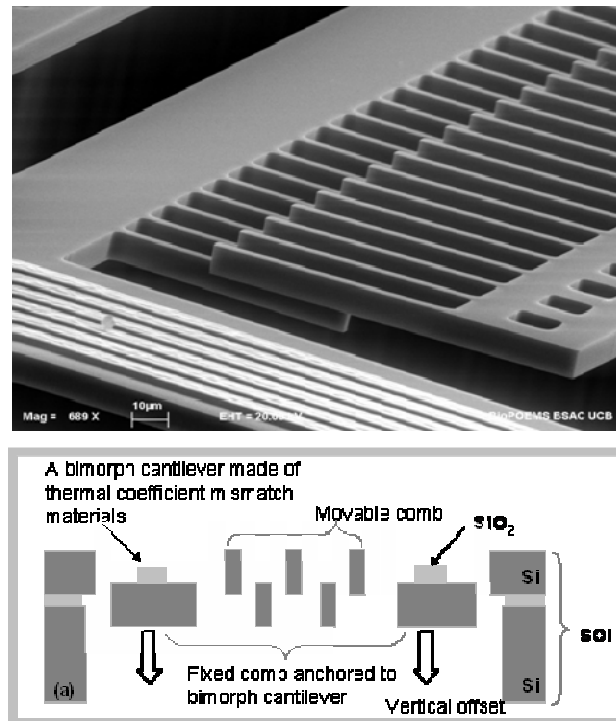
Figure 81. An SEM micrograph and a schematic diagram of a self-aligned vertical comb-drive fabricated from a single SOI wafer.

The mechanism of vertical offset between fixed and movable comb was based on residual stress.

The vertical comb-drive consisted of one movable comb above the two anchored combs on either side, as shown in Figure 82 (a). The movable comb structure incorporated a micromirror, a pinhole, a microlens holder, and a diffraction grating, as shown in Figures 82 (c) and (d). The device consisted of three electrodes connected to each comb structure, which was operated by either torsional or piston motion by generating an electrostatic force between the upper movable comb and one of the lower fixed combs (V1 and VGND) or between the upper movable comb and two lower fixed combs (V1, V2 and VGND). The design of this self-aligned vertical comb required an estimation of the deflection of a bimorph cantilever, which provided the initial engagement between a movable comb and the fixed combs. Even though residual stress arose from either the intrinsically or extrinsically stress-causing factors, the deflection was calculated using the analyses presented in previous work [96], with the assumption that the TCE mismatch was the dominant contributor to the deflection of the bimorph cantilever.
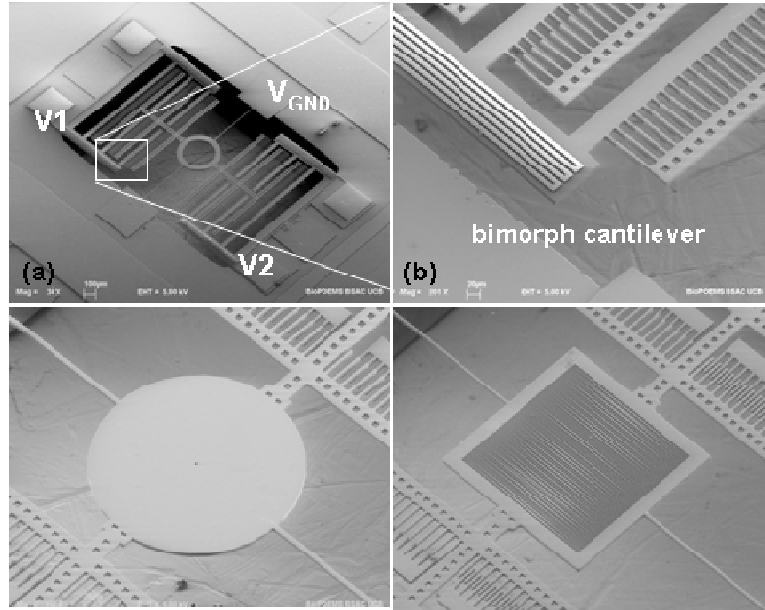
Figure 82. SEM micrographs of a self-aligned vertical comb-drive.

(a) A self-aligned vertical comb-drive with a microlens holder, (b) A bimorph cantilever anchoring fixed combs, (c) A tunable pinhole of 5 *μm*, and (d) A reconfigurable diffraction grating with 4 *μm* slit width.

5.1.2 VARIABLE FOCUS LIQUID LENSES

5.1.2.1 DYNAMIC CONTACT ANGLE MEASUREMENT

The droplet deformations of the fabricated lenses were characterized by dynamic contact angle measurements. Dynamic optical intensity measurements, magnification measurements, and static focal length measurement were also made. Dynamic contact angle measurements of μPELL were obtained with a Kruss™ system that used a high voltage waveform generator. A 0.5 Hz sinusoidal wave with a bias voltage of $400V_{PP}$ was applied to the patterned electrodes for the characterizations. A side view of a droplet was first recorded, and the contact angle of each frame was automatically extracted from the image. Figure 83 demonstrates the dynamic contact angle control of a droplet.
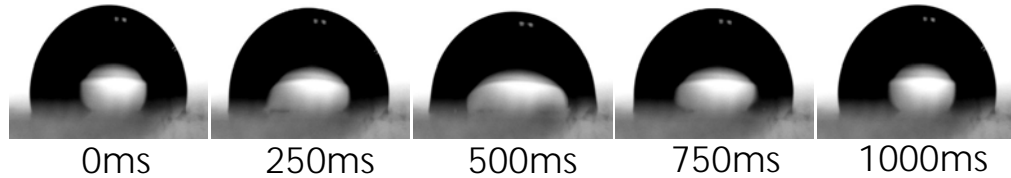
Figure 83. Demonstration of the dynamic contact angle control of a droplet.

The contact angle of a droplet changed from 80 to 100 degrees. (a) t = 0 ms, (b) t = 250 ms, (c) t = 500 ms, (d) t = 750 ms, and (e) t = 1000 ms.

Figure 84 shows a measured contact angle versus applied voltages. The early saturation of contact angle around 78° and 200 V was in accordance with the droplet model. Hysteresis of the contact angle was observed with respect to the applied voltage. Trapped surface charges, possible surface contamination, and the effect of gravity all can contribute to this effect. This phenomenon was not studied in detail.
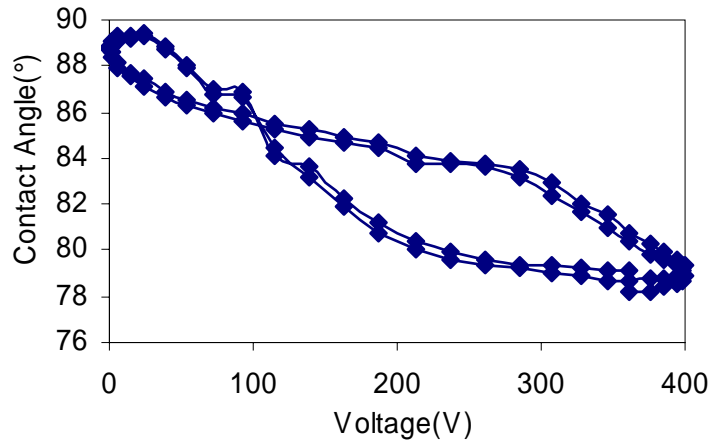
Figure 84. Measured contact angle with respect to applied voltage.

Saturation at high voltages agreed with the model.

5.1.2.2 DYNAMIC VARIABLE FOCUS MEASUREMENTS

Besides the dynamic contact angle measurements, light intensity through the lens was measured using a blue light emitting diode (LED) and a photodiode to characterize the dynamics of focal length change. The blue light was collimated using several lenses and was aligned with the liquid lens and photodiode on an optical bench. A custom-made high voltage source, detector and commercial AD board (National Instrument, USA) were used to acquire the intensity data, as presented in Figure 85. Because the photodiode was placed beyond the focal length of the liquid lens, and because the receptor field of the diode was smaller than the beam span of the liquid lens, the intensity change was interpreted as a focal length change. Intensity and contact angle profiles of the device were plotted together with applied voltage in Figure 86. Reproducible changes in contact angle were observed. The change of focal length due to the contact angle change was also shown. This result matched the results of the simulated inverse focal length versus the contact angles. In addition, about 100 ms of response time was observed, which can be improved by using smaller volumes of liquid.
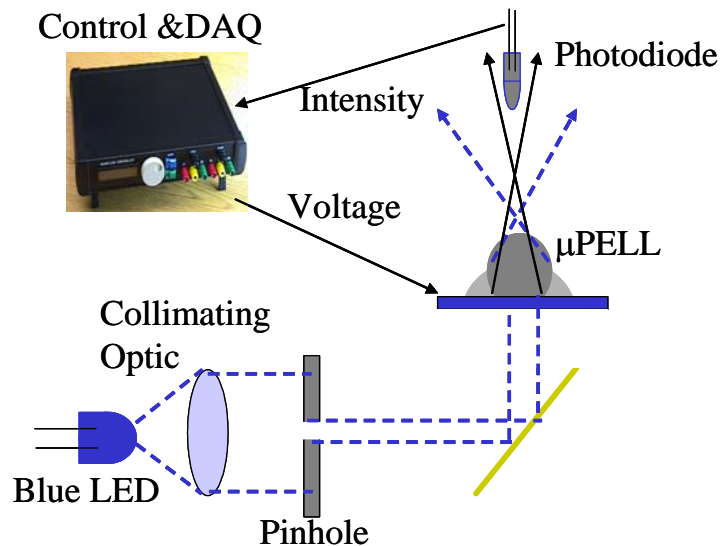
Figure 85. Experimental setup for dynamic measurements of the focal length change.
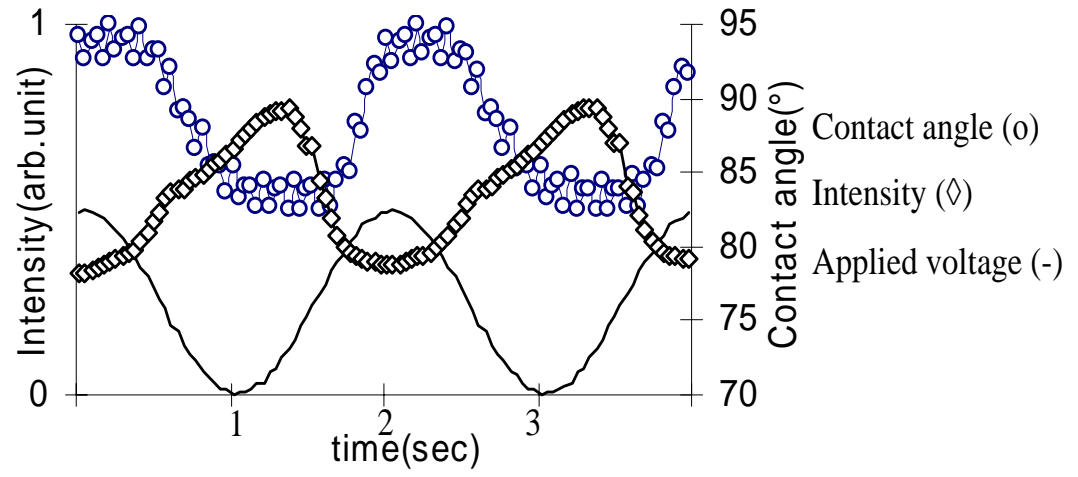
Figure 86. Dynamic measurements of the contact angle and the illumination of a lens vs. the applied voltages.

Varying intensity due to a varying focal length was measured using a photodiode.

5.1.2.3 MAGNIFICATION CONTROL USING A VARIABLE FOCUS DROPLET
LENS

Magnification changes due to droplet deformations are presented in Figure 87. Grid photographic images show the high optical power of the lens and the significant magnification variability that was measured by a change in the external voltage. An approximate measurement of focal length of a 1 μl water droplet determined by a screen test was 2 mm. This high magnification power will be useful in many on-chip optical systems.
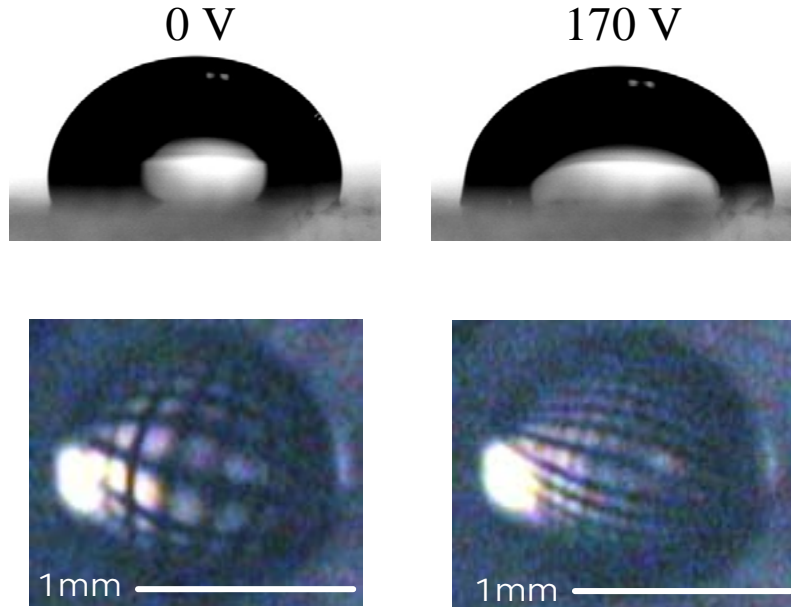
Figure 87. Magnification change due to the droplet formation.

(a) 0 V, (b) 170 V

5.1.2.4 LIQUID LENS ARRAYS

An improved droplet-dampening method was developed to prevent the evaporation of the liquid lenses. The micro-wells were fabricated with side walls that were activated by electrowetting. The improved packaging method, illustrated in Figure 88, shows the concept of a variable focus liquid lens array with micro-wells that was fabricated using highly doped silicon. The highly doped silicon was etched through to make conductive electrocapillaries. Then the sidewalls were coated with the hydrophobic insulator Parylene. After mounting the etched wells on the Indium Tin Oxide (ITO) coated glass, the array of wells was immersed in the electrolyte solution to fill the micro-wells. Time controlled evaporation of the liquid followed by cover glass sealing solved the dampening and evaporation problem. Applying voltage between the doped silicon and the bottom ITO coated glass changed the contact angle of the electrolyte on the side wall, resulting in controlled lens focusing.
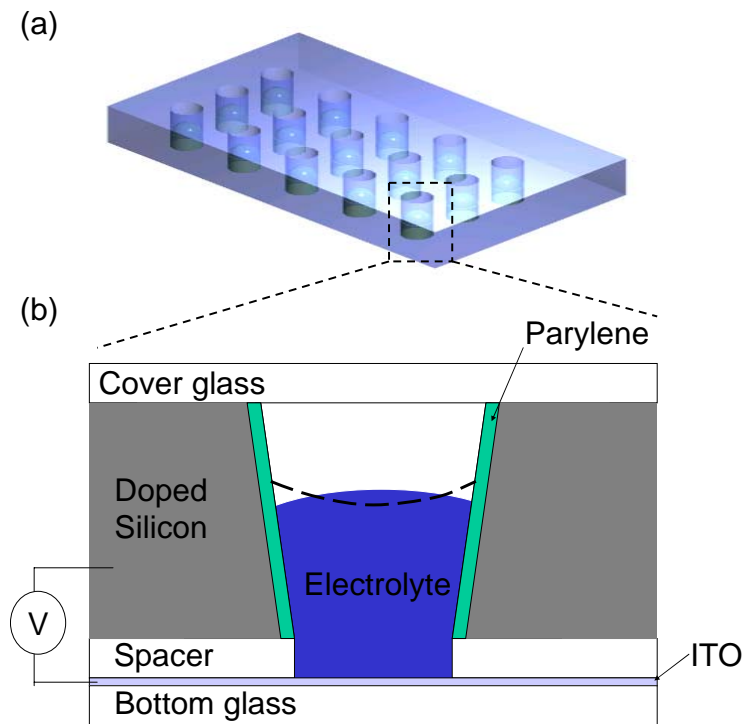
Figure 88. Concept of the micro-welled liquid lens array.

(a) Variable focus liquid lens array by micro-wells with electrowetting active side-wall and (b) Cross sectional concept diagram of a variable focus liquid lens.

5.1.3 POLYMER MICROROBITIC SYSTEM FOR SINGLE CELL MANIPULATION

The microfabricated workstation-platform was capable of positioning single cells by exerting mechanical forces on them. The platform consisted of microrobotic arm with three degrees of freedom and a pushing beam with a sharp tip at its end to mechanically stimulate the target cell (Figure 89). The microrobotic platform extended into two long gripper arms and formed a circular 10 µm in diameter cell holder. Two types of SU-8 actuators – chevron (I, II and IV) and hot-and-cold-arm (III) - were employed in the current design to open and move in two dimensions the gripper of the microrobotic platform. A third actuators allowed the movement of the pushing beam.
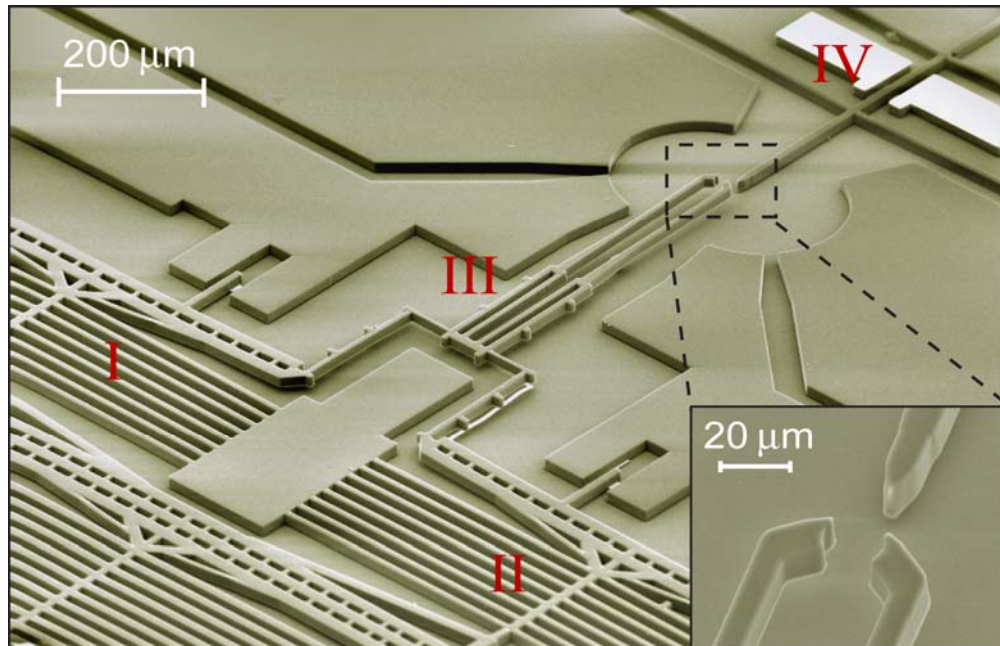
Figure 89. SEM micrograph of a released Microrobotic System.

A set of two hot-and-cold actuators (III) was employed to open the gripper arms. Two sets of chevron actuators (I & II) were used to position the cell holder in plane, while a third actuator (IV) was attached to the pushing beam. A close-up view of the cell test area was shown in the insert.

5.1.3.1 SU-8-BASED HOT-AND-COLD-ARM AND CHEVRON ACTUATORS

Before describing the mechanics of the microrobotic platform, a detail description of the two SU-8 based actuators incorporated in the design was necessary. The SU-8 hot-and-cold-arm actuator was activated by passing a current through a metal resistor-heater located at the bottom of the suspended SU-8 layer. In a conventional hot-and-cold-arm actuator, the current enters the hot arm and exits at the cold arm side. In an SU-8 hot-and-cold-arm actuator, the metal resistor was defined in a separate lithographic step, and

thus its dimensions can be different than the dimensions of the SU-8 structure. That feature was extremely important for achieving high performance hot-and-cold-arm actuators. It allowed the patterning of a U-shape heating element on the hot arm (Figure 90). The electric current entered and exited the hot arm, and thus no heat was generated in the cold arm and the flexure. The temperature difference between the hot arm and the cold arm was thus maximized. That concept was used to design the actuators of the microrobotic platform gripper (Figure 91).
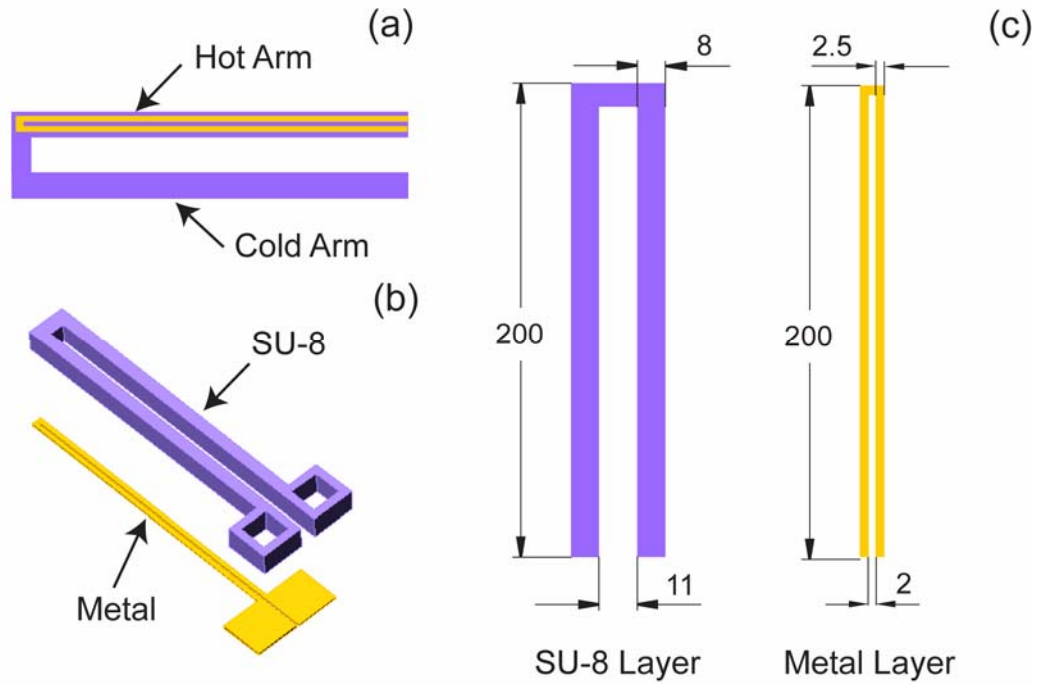
Figure 90. Hot-and-cold-arm actuator.

(a) Top view of the actuator where the metal resistor was patterned only on one side, (b) Three-dimensional view showing the two-layer structure, and (c) Typical dimensions of each layer (in µm).
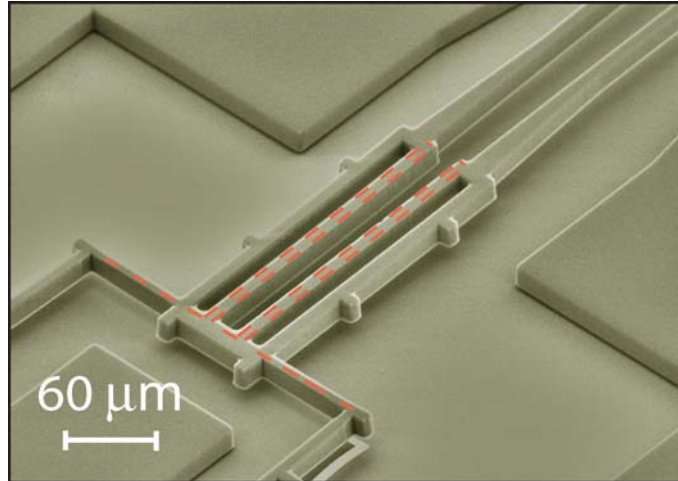
Figure 91. SEM micrograph of a gripper.

The red dashed line indicates that the Au/Cr layer was at the bottom of the SU-8 structure.

Additionally, the microrobotic platform had two independently controlled sets of SU-8 chevron actuators (Figures 92 and 93) that were mechanically coupled to the gripper and were responsible for the in-plane positioning of the gripper. An Au/Cr veneer was incorporated in the design to assist the experimental characterizations of the actuator. The SU-8 chevron actuators were 8 µ*m* wide V-shaped beams with a bending angle of 1 degree and a total end to end length of 790 µ*m,* resulting in a total length of 798 µm. The two ends were anchored to the substrate, which allowed the apex to expand outwards during the expansion of the polymer. Identical actuators were linked in series to increase the maximum output force.
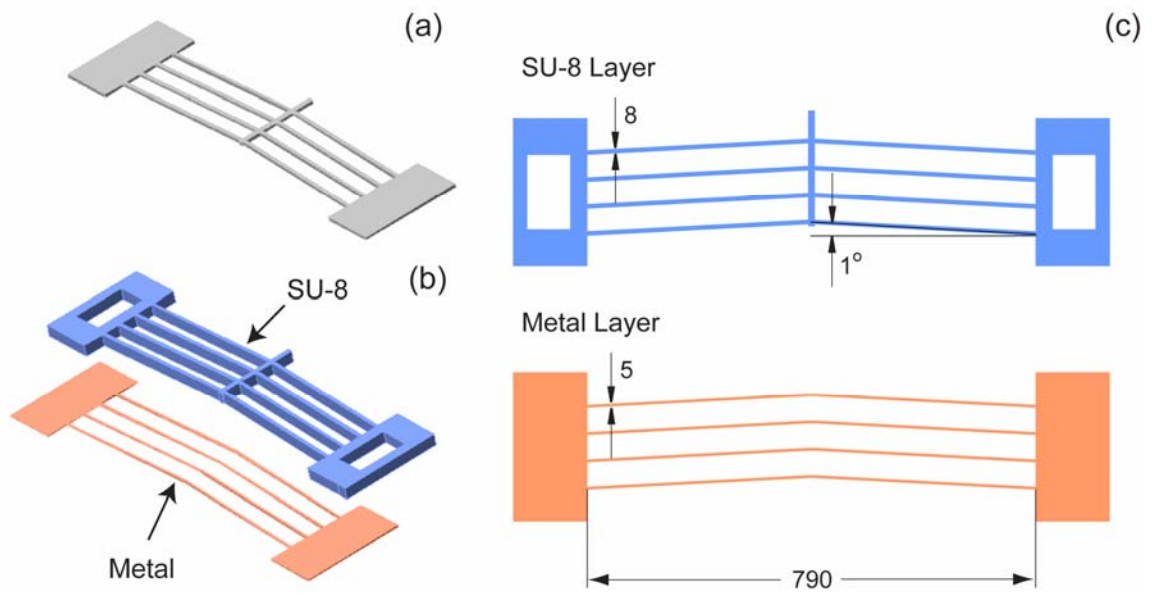
Figure 92. Chevron actuators.

(a) A conventional one-layer chevron actuator, (b) The SU-8 based actuator consisting of two layers, and (c) Typical dimensions of each layer (in µm).
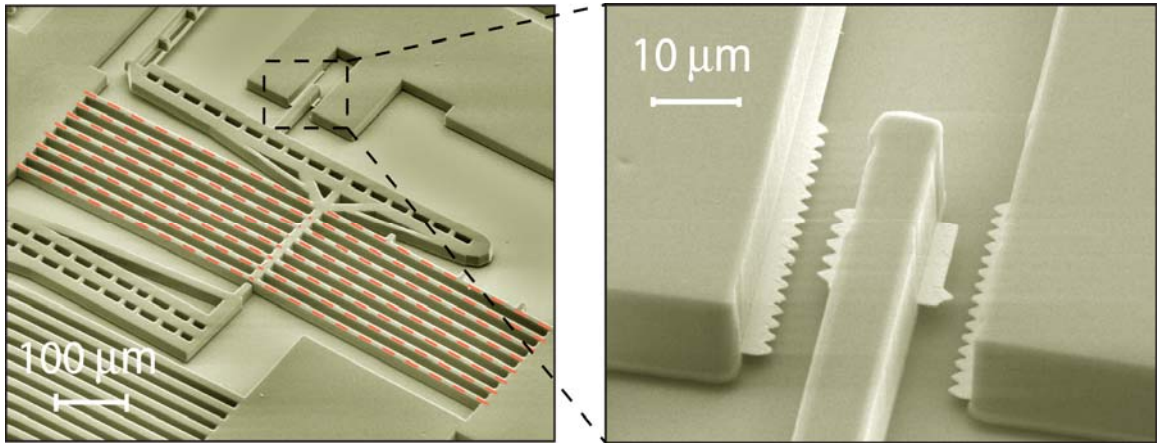
Figure 93. SEM micrograph of a released chevron actuator.

The red dashed lines indicated that the Au/Cr layer was at the bottom of the SU-8 structure. A close view of the Au/Cr veneer was shown on the right.

5.1.3.2 MECHANICS OF THE WORKSTATION

The microrobotic gripper had three degrees of freedom (Figure 94). When either the left or right chevron actuator was activated, the gripper moved in an arching motion towards the opposite side (A & B). The gripper moved forward when both chevron actuators were equally powered (C), and could be positioned at other locations in the plane when the chevron actuators were unequally powered. The gripper opened and closed when the two hot-and-cold-arm actuators were activated (D).
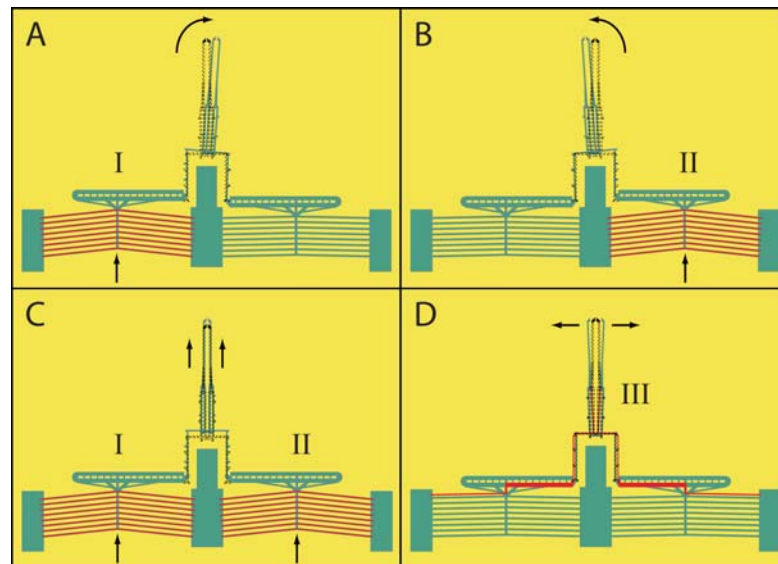
Figure 94. Two chevron actuators.

108

An important aspect of this design was the displacement amplification of the gripper holder compared to the linear displacement of the other chevron actuators. An ANSYS, Inc. Finite Element Analysis model of the microrobotic arm was constructed to illustrate the amplification mechanism (Figure 95). The total displacement of the cell holder was 12.51 µm when one of the chevron actuators was displaced by 6 µm. The arm rotated with respect to a virtually fixed point (almost zero displacement) and the corresponding displacement amplification of the cell holder was 2.1 times the displacement of the chevron actuator.
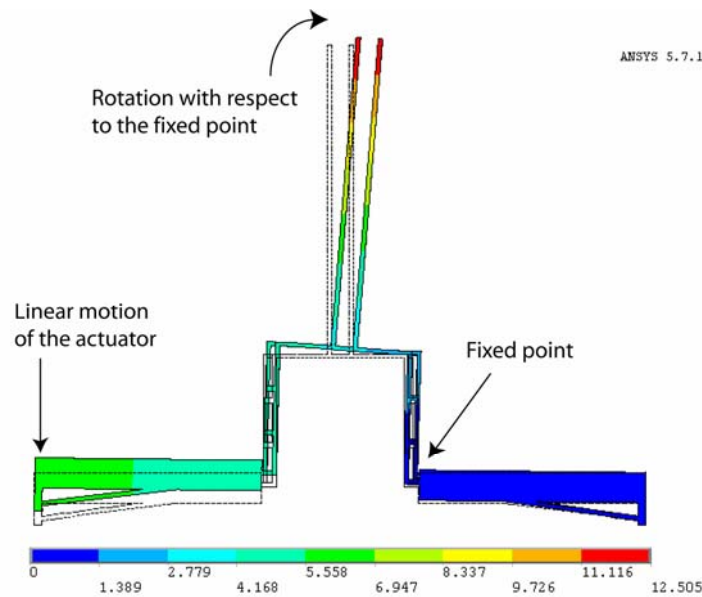
Figure 95. Mechanics of a microrobotic arm.

The total displacement of the cell holder was 2.1 times higher than the linear displacement of the chevron actuator (not modeled for simplicity).

The deflection of a bimorph cantilever and the vertical offset were measured with a Wyko NT3300 optical profiler. A depth profile of the device part was displayed in the Figure 96 (a) contour plot. Deflection was not observed for the movable comb-structure. The calculated and measured deflections of the cantilever beam along the AA´ line are plotted in Figure 96 (b). The beam deflection and the vertical offset increased along the length of the beam. The measurements were performed for the five cantilevers located at different sites over the wafer. At the end of the 680 μm long cantilever, the average maximum deflection was 16.9 μm, and the standard deviation was 0.86 μm. The vertical offset between the combs was 18.3 μm on the first comb, 9.2 μm on the second comb, and 3 μm on the third comb, as shown in Figure 96 (c). Since single crystal silicon was a stress free material and the thermal oxidation process was well established, the precise control of the deflection of the bimorph cantilever was possible.
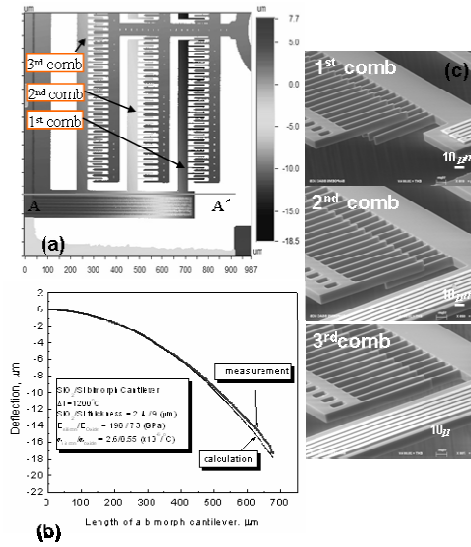
Figure 96. Biomorph cantilever.

The deflection of the bimorph cantilever was measured with an optical profiler: (a) Contour of depth profile on a part of the vertical comb-drive, (b) Comparison between the measured and the calculated cantilever deflections, and (c) SEM micrographs of the vertical offset being gradually increased according to the deflection of a bimorph cantilever.

The frequency and phase responses of the vertical comb-drive were characterized for both torsional and piston motion with a Polytech Laser Vibrometer, which had a minimum beam spot size of 3 μm and a vertical resolution of 2 nm. The resonant frequencies at each motion were measured by applying a 5.5 V DC bias and 10 V AC, as shown in Figure 97. In piston motion, the vertical amplitude was 30 μm at the resonant frequency of 3.5 kHz. In torsional motion, the optical angle of the deflection at the resonance of 830 Hz was up to 6.5°. The phase angles at both resonances were shifted by 90°. Q-factors were 24.2 in piston motion and 7.6 in torsional motion. Because the mechanical spring in the piston motion was designed to have a higher stiffness than in torsional motion, the piston motion resonant frequency was higher. The Q-factor also

increased, and the spring constants that provided the damping coefficients were comparable in both motion. For comparison, the model analysis that was performed by a
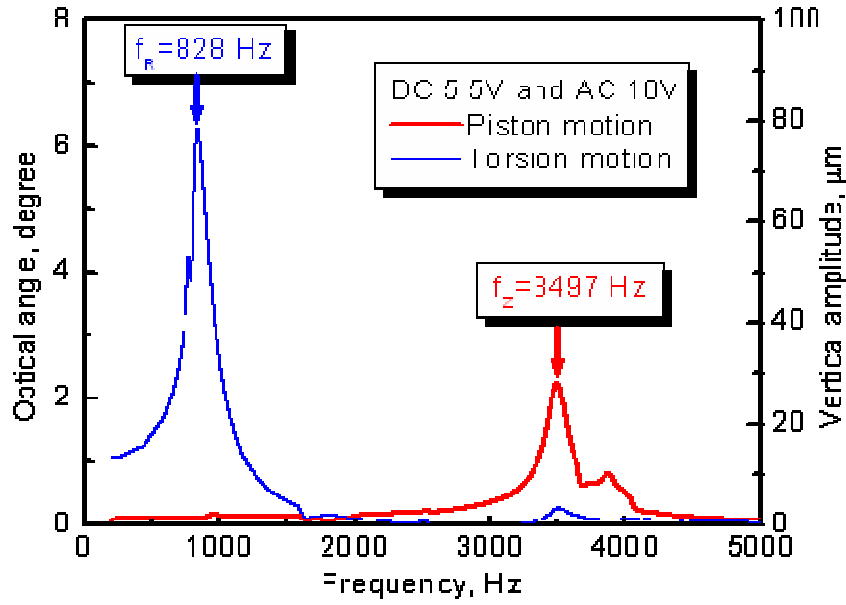
Figure 97. Vertical comb-drive in torsional and piston motion.

The frequency and phase responses of the vertical comb-drive were characterized in both torsional and piston motion with a Polytech Laser Vibrometer. The minimum beam spot size was 3 *μm* and vertical resolution was 2 *nm*.

Finite Element Method using ANSYS ver.5.7 had simulated resonances at 3388 Hz in piston motion and at 910 Hz in torsional motion, which corresponded to the measured results within 10 %.

The DC modulation of the device at resonance was plotted in Figure 98. For a vertical comb-drive with a microlens holder, the vertical amplitudes and optical angles of the deflection at resonance under a constant AC voltage (10 V) increased linearly with the applied DC bias voltages between 3 V to 5.5 V. The resonant transmissibility, defined by the ratio of output amplitude to the input DC voltage at resonance, was 4.7663 μm per unit DC bias voltage for the piston motion and 0.4467° per unit DC bias voltage for torsional motion. The pull-in of the device occurred at DC bias 9.5 V for the piston motion and 8.5 V for the torsional motion. The voltage for the torsional motion was less, because the electrostatic force was applied to only one side electrode (V1). The force caused in-plane motion then made it unstable, while the electrostatic force in piston motion was attracted by both side electrodes (V1 and V2). In future designs, the moment of inertia relative to the principle axis of torsional motion should be minimized to increase the stability and optical scanning angle in torsional motion.
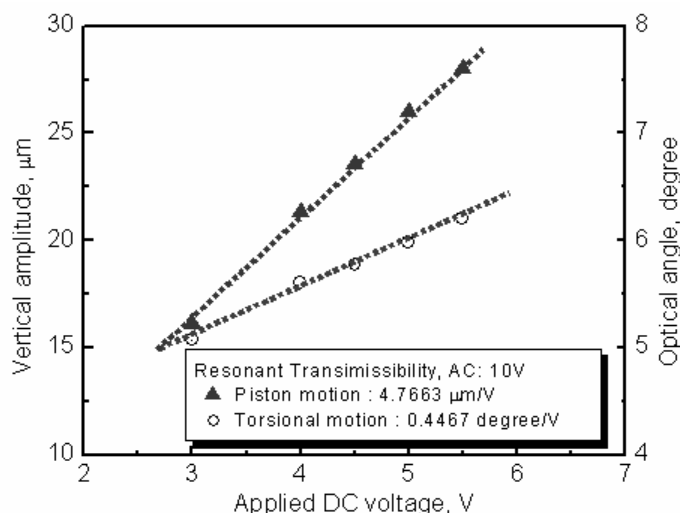
Figure 98. DC modulation of a bimorph cantilever.

The vertical amplitude and the optical angle at resonance were linearly proportional to the applied DC voltage.

5.1.3.3 ELECTROMECHANICAL CHARACTERIZATION

To determine the mechanical performance of the device, DC voltages were applied at the chevron actuator and at the two hot-and-cold-arm actuators of the microrobotic arm, and the corresponding displacement response in air and in Dulbecco's Phosphate Buffered Saline (D-PBS) environments were measured with a light microscope (Figure 99 and 100). As mentioned earlier, the chevron actuators were manually stretched using a probe tip at 0.25% strain and 1 Volt (80 mA) that was applied for 20 min to induce additional polymerization at the stretched state, which partially relieved the residual stress. Special treatment was not needed for the hot-and-cold arm actuators since there was no residual stress. DC driving voltages facilitated the characterization procedure. The opening of the gripper required less than 2 V for a maximum displacement of 8 µm in the D-PBS, while the chevron actuator was driven by slightly higher voltages (2.6 V at 14.5 µm total displacement of the cell holder). Larger displacements were restricted by severe electrolysis. As pointed out earlier, electrolysis would have been eliminated if only AC voltages were used.

113
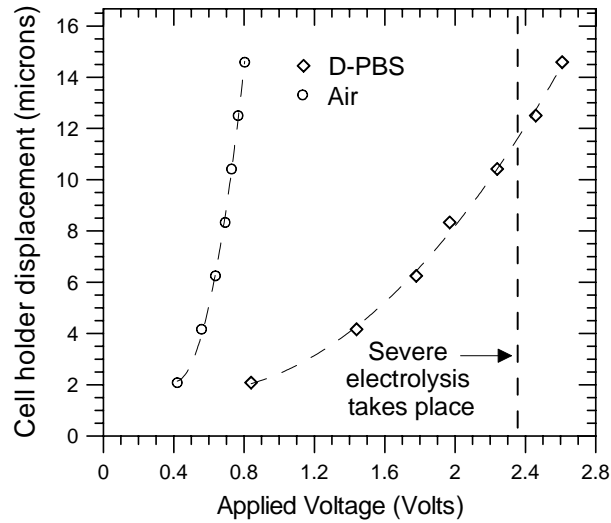
Figure 99. Electromechanical characterization of a microrobotic arm.

Voltage was applied to one of the chevron actuators. The cell holder displacement refers to the total displacement from its initial position (it moved in an arc).
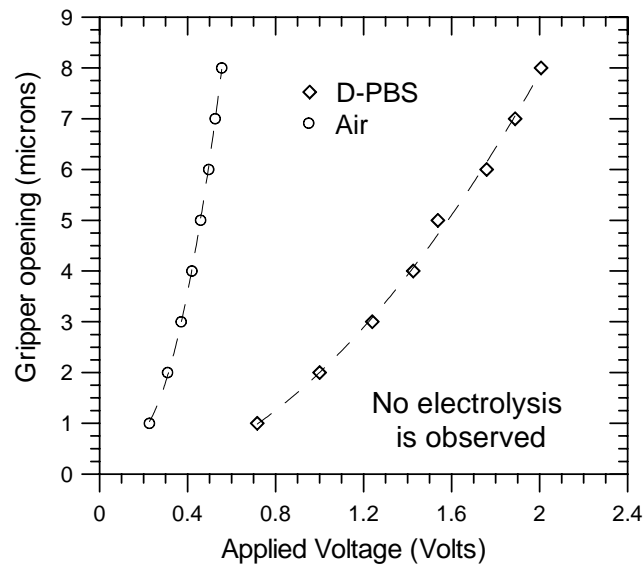
Figure 100. Gripper opening verses applied voltage.

A displacement of 8 µm required only 2 Volts.

5.1.3.4 TEMPERATURE FIELD

To experimentally verify that the design had a minimum thermal effect on the target sample while maintaining acceptable displacements, the temperature distribution was visualized using an infrared CCD camera (Figures 101 and 102). The device was immersed in the D-PBS environment and the chevron and hot-and-cold-arm actuators were activated independently at 2.6 V and 2 V, respectively (corresponding to 14.6 µm and 8 µm of displacement). The temperature near the cell holder was increased by 15-16

114

°C degrees and 1-2 °C above room temperature (19.3 °C) when the chevron and hot-and-cold-arm actuators were powered, respectively. The actual temperature of the cell holder was expected to be slightly higher, since the infrared camera captured the radiation emitted from the bulk of the D-PBS solution (50-100 µm thick), averaging the temperature gradient that existed in the vertical direction.
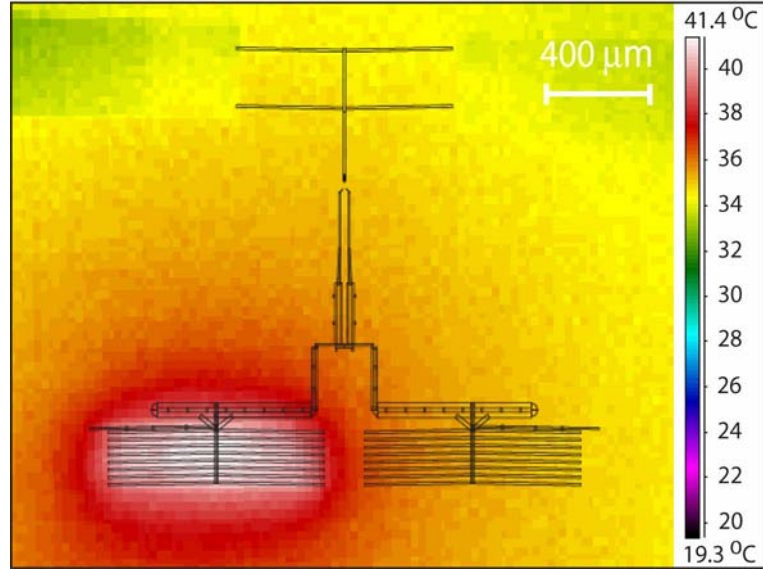
Figure 101. Temperature field as visualized using an infrared camera.

The system was immersed in a liquid and the right chevron actuator was activated at its maximum displacement (14.6 µm displacement of the cell holder at 2.6 V).
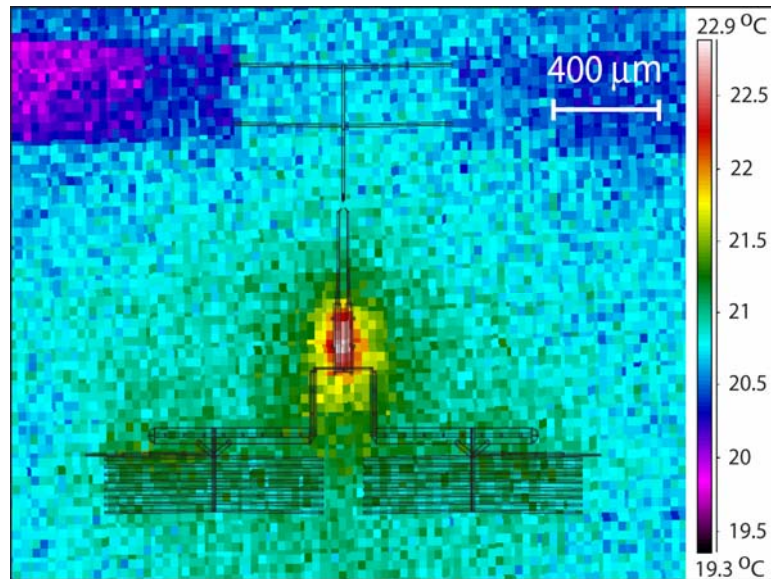
Figure 102. Temperature field of a gripper.

Activated at its maximum displacement (8 µm at 2 Volts).

Additionally, the average temperatures obtained by the infrared CCD camera were verified by correlating the resistivity changes to the temperature changes. The average increase in temperature of the chevron actuator was estimated from the change in resistance of the Cr/Au resistors:

$$\Delta T_{ave} = \frac{R(T_{ave}) - R(T_0)}{R(T_0)} \frac{1}{\alpha_{Cr/Au}} \tag{23}$$

where $\alpha_{Cr/Au}$ was the temperature coefficient of resistance (TCR) of the Cr/Au film. The TCR was experimentally found to be equal to 3.36 ppm/^{o}C. Figure 103 illustrates the dependence of the average temperature change of the chevron actuator versus its displacement (measured using the Au/Cr veneer). The average temperature change ($\sim$20°C at 2.6 Volts) was comparable to the temperature obtained using the infrared camera (Figure 101).
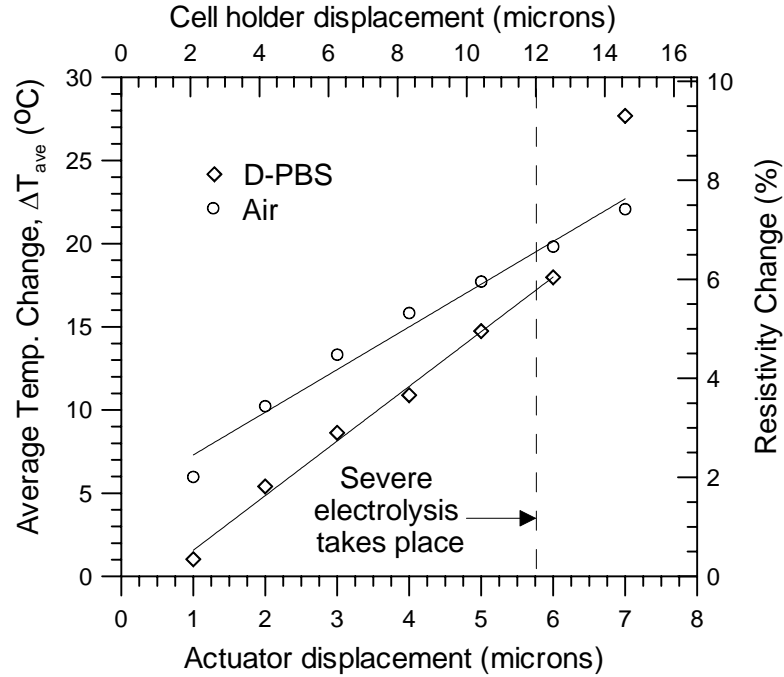
Figure 103. Average temperature change versus chevron actuator displacement.

The corresponding cell holder displacement was shown on the top x-axis. Immersed in D-PBS, the holder moved 10 μm at ΔT_{ave} = 14-15 ^{o}C. Operation in D-PBS required q lower ΔT_{ave}.

5.1.3.5 MANIPULATING CELLS IN SOLUTION

The SU-8 based, microfabricated single cell workstation described in the following paragraphs had two types of electrothermally activated, in plane, SU-8 actuators. Actuation was provided by thermal expansion of the SU-8 structures through resistive heating of a thin Cr/Au layer selectively attached at the bottom of the suspended

polymer structure. The SU-8 microactuators were activated in physiological media at low voltages (1.5-2.5 V) and small temperature increases ($\sim 22^{\circ}$C). Furthermore, the ability to activate the SU-8 actuators using alternating current (AC) instead of direct current (DC) ensured that electrolysis and electrophoretic forces were absent.
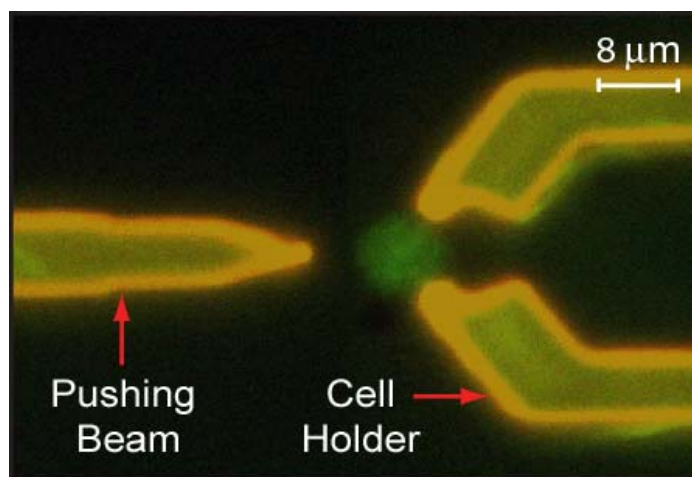
Figure 104. Manipulation of a Hela cell in solution using the polymer microrobotic workstation.

To demonstrate the ability of the microrobotic workstation to operate with real biological samples, a suspension of Hela cells was pipetted (cultured in Dubelco's Modified Edge Medium and diluted in D-PBS), and cells were successfully manipulated. Figure 104 shows a gripped and positioned single Hela cell in front of the tip of the pushing beam.

Figure 105 presents a more complete description of the demonstration. After the gripper had trapped the cell and returned to its initial position, the pushing beam moved forward and slightly squeezes the cell. Sinusoidal driving voltages of a frequency of 20 KHz were used to avoid electrolysis. It was observed that freshly the pipetted cells were being dragged away by the fluid flow caused by the motion of the gripper arm, indicating that viscous forces were dominant in such microscale flows. That problem was overcome by incubating the cells on the silicon dioxide surface for an hour at room temperature. The incubation period allowed bonds to form with the glass surface, which then counterbalanced the hydrodynamic forces.
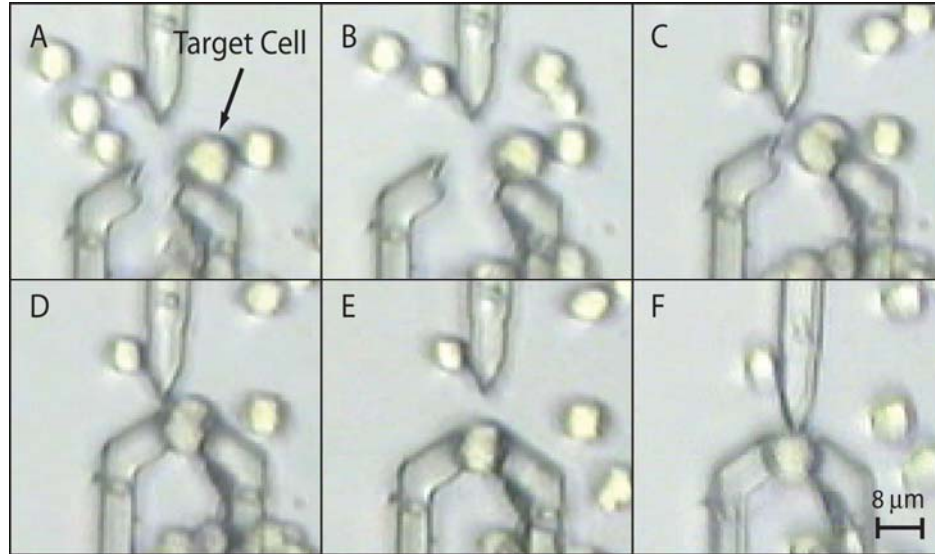
Figure 105. Manipulation of a Hela cell in solution.

(a) The cell was initially located near the right side of the cell holder and the gripper was in its initial closed position, (b) The gripper was open, (c) The two chevron actuators were activated aligning the cell holder to the cell, (d) The gripper closed, trapping the cell, and returned to its initial position, and (e) The pushing beam was moving forward, touching and slightly deforming the trapped cell.

5.2 MICROSCALED SYSTEMS

5.2.1 MICROMACHINED CONFOCAL LINE SCANNER

5.2.1.1 SYSTEM RESOLUTION AND SPECIFICATIONS

The transverse resolution of the micromachined confocal line scanner system was determined by measuring the edge responses. The axial response of the system was measured from reflected intensity variations by moving a plane mirror sample in the vertical direction. Figure 106 shows the lateral and axial resolution of the system. A line spread function (LSF) with a Full-Width Half-Maximum (FWHM) of 1.6 µm (measured from 20 %-80 % edge response of 1.5 µm) and axial resolution of 34 µm with a single microlens objective lens were measured. Other details of system specification are summarized in Table XIII.

Table XIII. Summary of the characteristics of the gimbaled mirror system

Specification	Value
Transverse resolution	1.6 µm
Axial resolution	34 µm
Scanning speed	1.16 kHz
Scanning range	100 µm
Working distance	340 µm
Wavelength	633 nm & 535 nm
Objective NA	0.4
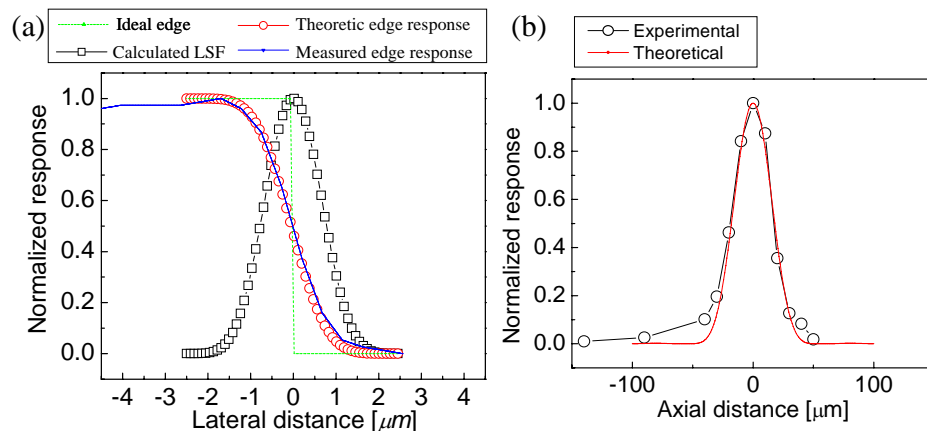
Figure 106. Measurement of the system resolution.

(a) Estimated lateral resolution from measured edge response, and (b) Axial resolution.

5.2.1.2 IMAGING OF 1-D GRATING

As a demonstration of the densely packed, multi-microfluidic channel scanning capability, a reflectance grating pattern (Al on quartz) with 5 µm wide grates and 5 µm spacings was imaged. Figure 107 shows a reconstructed reflectance profile of the grating. A notable point was that the peaks did not have the same intensities. The reflected intensity peak decreased at the edges due to the off-axis scanning mechanism, since at the edges less reflected light was focused at the pinhole. This intensity variation over the scanning range was calibrated using the plane reflector image. However, this was not a serious problem for the fluorescent detection since fluorescent light was emitted omni-directionally and was focused back to the pinhole.
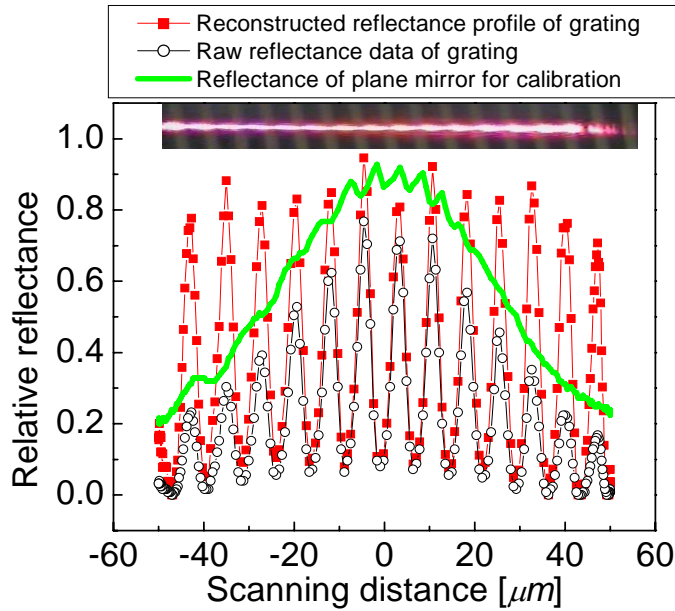
Figure 107. 1-D confocal reflectance imaging demonstration of a 5 µm grating.

Reflectance profile of the grating (shown at the top) was reconstructed by confocal line scanning over the grating in the reflectance mode. The raw data was calibrated using a plane reflector signal.

5.2.1.3 MULTIPLEXED DETECTION OF MICROFLUIDICS

The results of scanning the reflection grating confirmed that microfluidic channels were 5 µm wide with 5 µm spacing. As a proof-of-concept, the fluorescent intensity detection of PDMS microfluidic channels (five-5 µm wide channels and two-15 µm wide channels) filled with 1 µM Nile Red fluorescent beads were scanned using a 532 nm green diode laser, as shown in Figure 108. The system was changed to the fluorescent mode by introducing an emission filter in front of the photodiode.
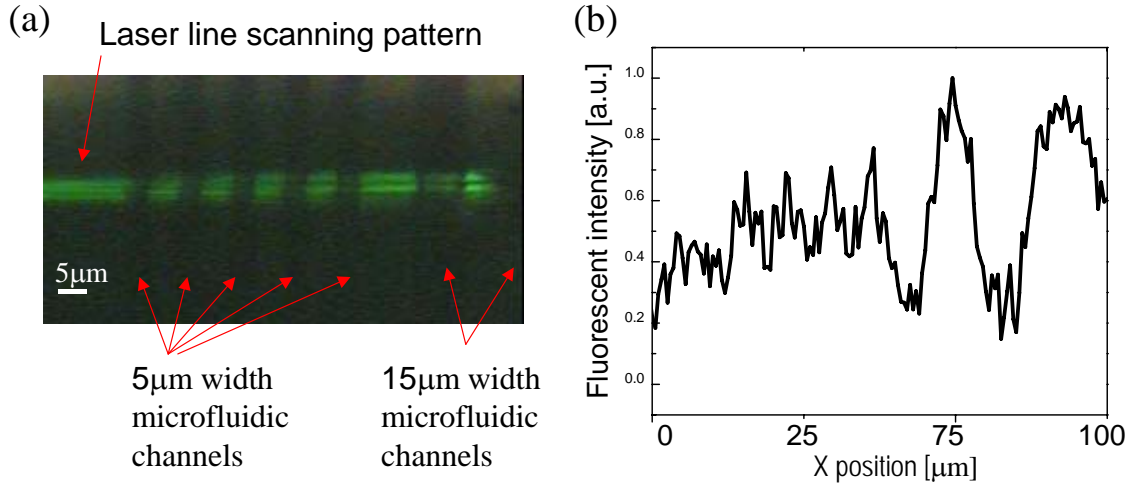
Figure 108. Fluorescent detection from microfluidic channels filled with fluorescent [1 µM] beads. (a) Light microscope photograph of a laser line scanning of five-5 µm channels and two-15 µm channels, and (b) Corresponding reconstructed fluorescent intensity profile.

120

5.2.2 MINIATURIZED CONFOCAL OPTICAL SCANNING MICROSCOPE

In this section, a palm-sized laser scanning confocal microscope is described that was based on the micromachined transmissive confocal scanning head described in the previous sections. A confocal reflectance imaging experiment was performed to demonstrate this micro-system. Determined system performances and limitations are also described.

5.2.2.1 MINIATURIZED MICROSCOPE SYSTEM

The miniaturized transmissive scanning confocal head enabled a dramatic size reduction of the four major components of a confocal microscope: the objective lens, the scanners, the pinhole, and the pupil. By simply adding a light source and a detector, a prototype of a miniaturized confocal microscope system has been completed, as shown in Figure 109. The illumination and detection paths were as follows. A collimated laser beam (633 nm, 1 mW) from a diode laser was reflected by a beam splitter. The beam was focused onto the transmissive scanning confocal head's pinhole by a pinhole lens. After passing though the pupil of the aperture chip, the beam was focused by the X and Y microlens scanner. The sample was placed at the image plane of the microlens, 200 µm above the X microlens. The detection path was the inverse order of the illumination path up to the beam splitter. The reflected light from the sample passed through the microlens scanners, the pupil, the pinhole, and the pinhole lens. Then the beam was split by the beam splitter, and was then focused on the silicon photodiode by a collector lens. The reflected light intensity was converted to an electric signal at the photodiode and acquired by a digital oscilloscope connected to the photodiode. The focus on the sample was scanned in 2-D by the X and Y microlens scanners. A 2-D confocal image of a sample was reconstructed from the time profile of reflected light intensity.

Microfabricated Transmissive Scanning Confocal Head

Sample

Pinhole Lens

Diode Laser (633nm)

Beam Splitter

Si Photodiode

Collector Lens
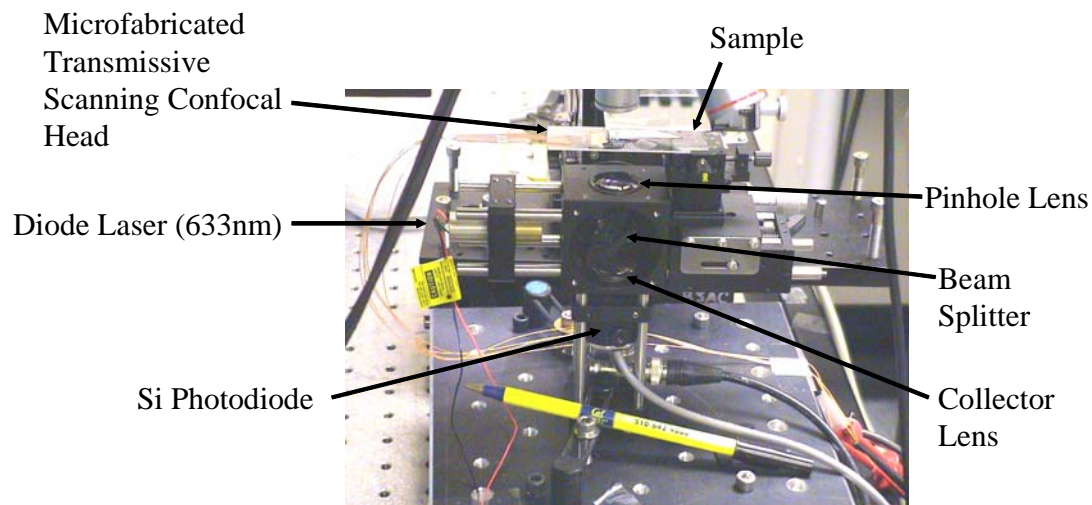
Figure 109. Photograph of the miniaturized laser scanning confocal microscope.

A palm-top sized laser scanning confocal microscope was implemented utilizing a microfabricated transmissive scanning confocal head, a solid state off-the-shelf laser diode and a photodiode.

5.2.2.2 CONFOCAL REFLECTANCE IMAGING

Preliminary images have been made with the miniaturized confocal optical scanning microscope. Figure 110 (a) shows an aluminum test pattern on a glass substrate and the line-scanning pattern of the laser beam. The laser beam from the pinhole was focused onto the test pattern by the microlens scanners, and then the test pattern was scanned. The image was reconstructed by measuring the time profile of the reflected light intensity using the system's photodiode. Figure 100 (b) shows the reconstructed image of the test sample. The field of view of the image was 100 μm by 50 μm and features smaller than 5 μm were clearly resolvable. Images of another test pattern are shown in Figure 111. The thick rectangular pattern in Figure 111 (a) was from the raster scanning of the focused laser.
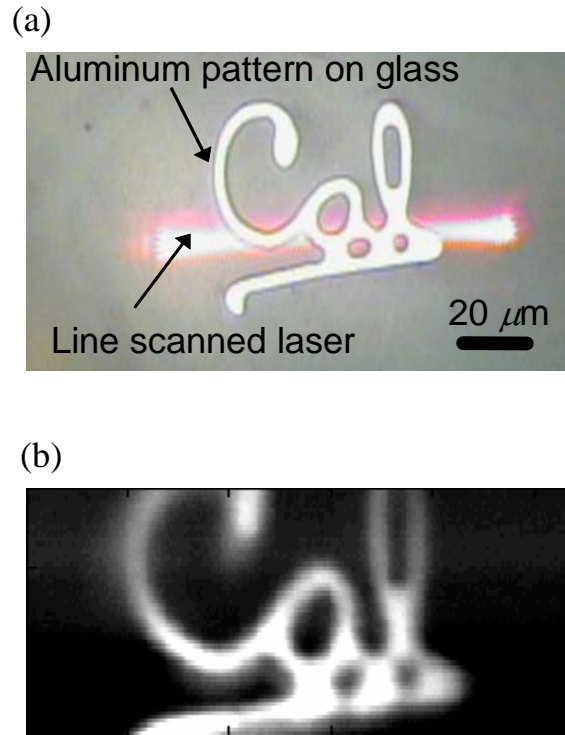
Figure 110. Light microscope photographs of the Cal test pattern.

(a) An Aluminum test pattern on a glass substrate and the line scanning pattern generated by the micromachined transmissive scanning confocal microscope, and (b) Reconstructed image of the test pattern. The field of view was 100 μm by 50 μm.
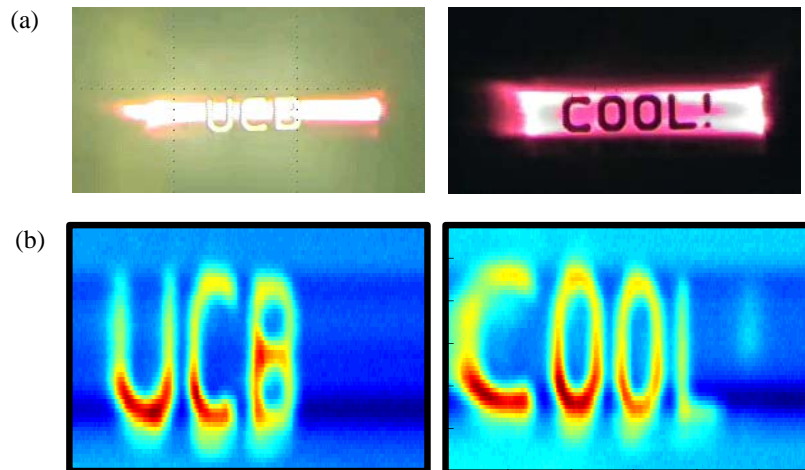
Figure 111. Light microscope photographs of other test patterns.

(a) The raster scanning pattern of the focused laser beam on glass substrate, and (b) Reconstructed images of the test patterns. The field of view was 100 μm by 50 μm.

5.2.2.2 TRANSVERSE AND AXIAL RESOLUTION

The miniaturized confocal optical scanning microscope system's resolution was determined by imaging edges. Figure 112 (a) shows the measured response of the microscope to an aluminum edge on a glass substrate located at the center of the field of view, taken in the x direction. The line spread function of the system was determined by taking a spatial derivative of the edge response. The dashed line was the calculated line spread function from the measured edge response. A 20-80% edge width of 1.7 µm and a FWHM transverse resolution of 3 µm were determined.   The axial response of the microscope was measured by scanning a plane reflector along the beam axis, as shown in Figure 112 (b). The measured FWHM axial resolution of the microscope was 37 µm. Those resolutions were achieved with microlens doublets with an inner pupil diameter of 300 µm. We believe that sub-micrometer resolution can be achieved by optimizing the pinhole size and the lens design. Images of gratings with different widths are shown in Figure 113.
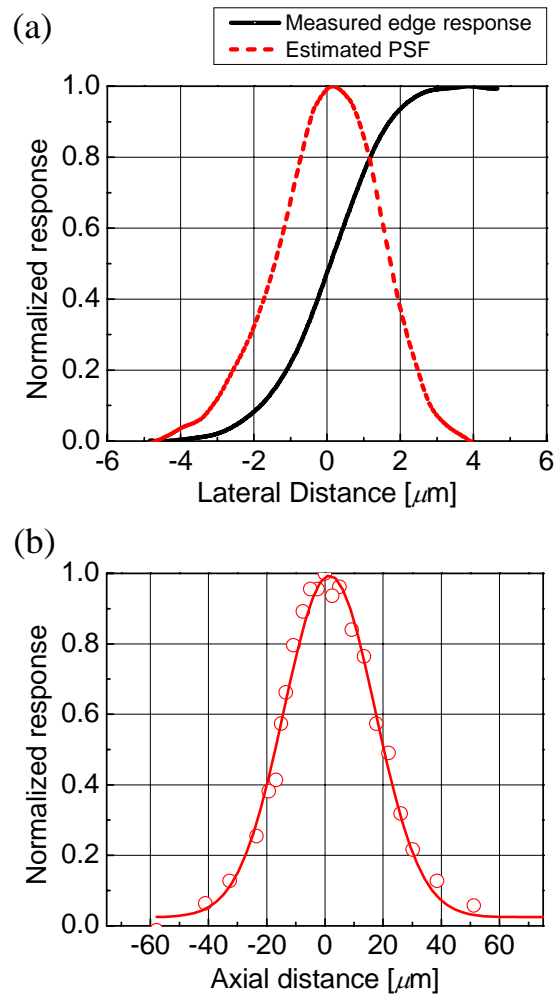
Figure 112. An Aluminum edge test pattern.

(a) Experimental x-direction edge response (solid curve). The corresponding theoretical line-spread function was plotted with a dashed curve. (b) Measured axial response.
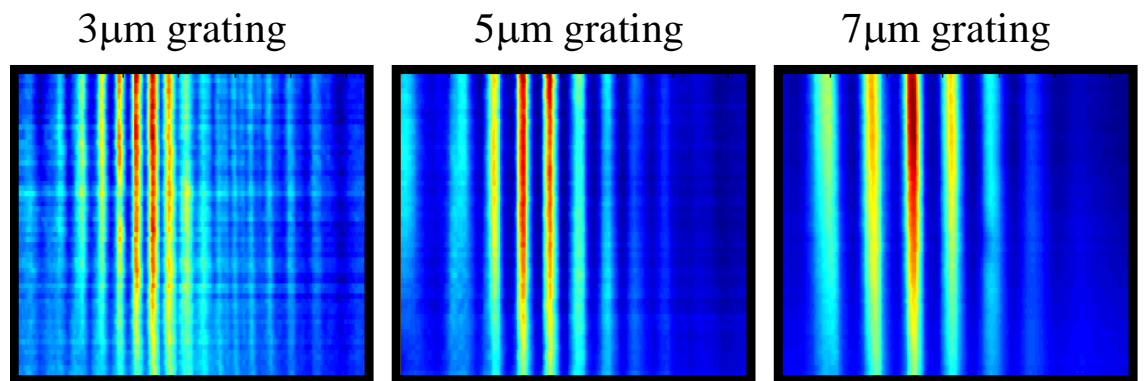
Figure 113. Photographs of reflection gratings with different widths.

5.2.2.3 POST PROCESSING OF IMAGES

The integration and assembly of a miniaturized confocal optical scanning microscope was simplified by this design. However, as shown, there were degradations in the image quality and brightness at the edges of the field-of-view due to off-axis aberrations. Figure 114 (a) is a raw image of a reflection grating with a 10 μm period. The microlenses' axis was centered at the bottom side of the image. The upper and right sides of the image were darker and had less contrast than the bottom edge. To normalize for this non-uniformity in brightness, the image of a plane reflector was used for calibration. The calibrated image of the grating had a better contrast over the field of view since the reflected intensity of the raw image was normalized with respect to that of the plane mirror surface.

(a)   (b)
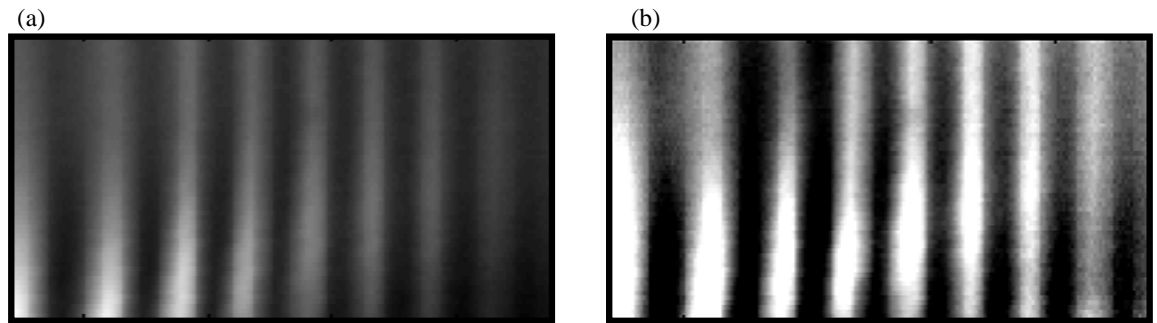
Figure 114. Photographs of reflection gratings.

(a) Image of reflection gratings with 10 μm period, 80 μm by 50 μm field of view before calibration, and (b) Calibrated image of (a) using an image of a plane reflector.

5.2.3 MINIATURIZED TOTAL INTERNAL REFLECTION (MTIR) FLUORESCENT MICROSCOPE

A prototype miniaturized TIR-based biochip platform (Figure 115) was fabricated and tested. The ability of this system to detect real time events has recently drawn the interest of researchers for studying the dynamics of various biological systems [98]. The ability of this system to perform similar functions was experimentally demonstrated by detecting the Brownian motion of fluorescent microspheres.
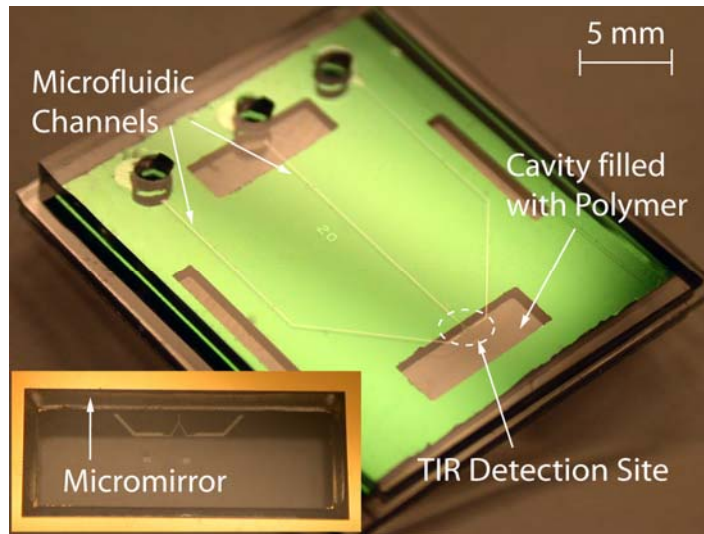
Figure 115. The TIR-based biochip with integrated microfluidic channels forming a Y configuration.

Four cavities are shown with one that was active (where the channels cross). The backside of the chip is shown in the inset.

5.2.3.1 INTEGRATED PORTABLE OPTICAL SYSTEM

A green laser diode (model VLM-532-43LCB from Quarton Inc., optical power output ~5 mW) was used as a fluorescent excitation source. The output light beam was 2 mm in diameter, was linearly polarized and had a half divergence angle of < 0.3 mrad. The green laser diodes were semiconductor light sources similar to the ones used in green laser pointers with a peak wavelength of 532 nm. They were inexpensive, compact and provide enough optical power to excite fluorescence. A web CCD camera (QuickCam Pro 4000) was used as a real-time imaging detector. The resolution was limited to 640x480 pixels at an adjustable exposure time range of 250 ms to 0.1 ms. The web camera was disassembled from its original package and attached to a plastic frame. The recorded images were directly transferred to a computer through a Universal Serial Bus (USB) port. Although low-cost CCD cameras were intended for internet videoconferencing, their sensitivity and resolution proved to be adequate for imaging fluorescence.
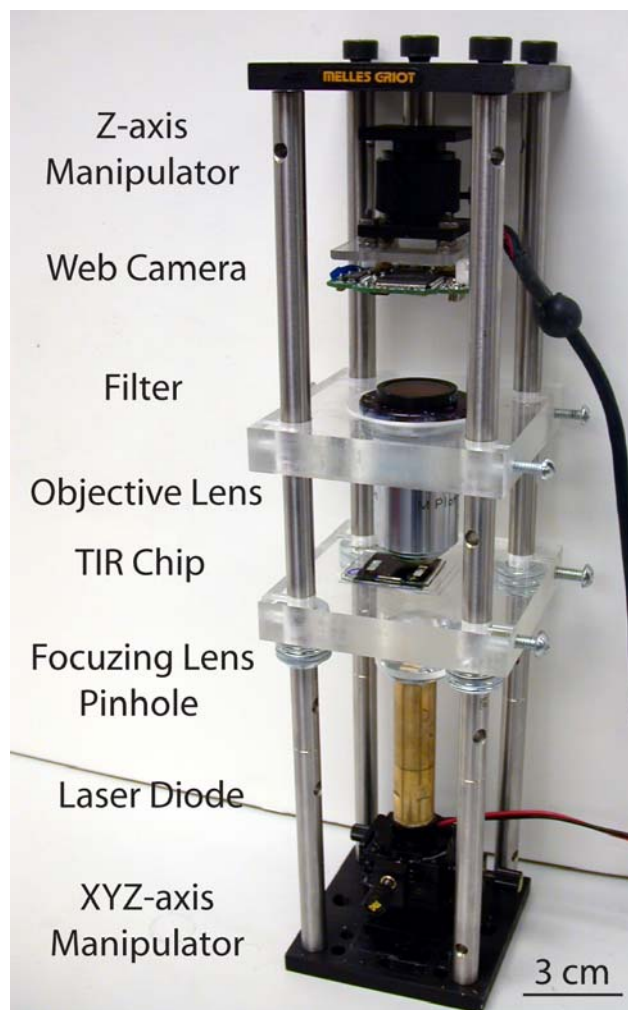
Figure 116. The integrated optical system.

All the optical components were vertically integrated resulting in a compact system 28 cm in height.

The custom-made optical system (Figure 116) was completed with the addition of a fluorescence filter to suppress the excitation laser light from being detected though the CCD camera and a microscope objective lens. The microscope objective (MicroPlan 40x, Nikon) was separated by 3 cm from the camera. A 1 mm pinhole was mounted on the laser-head to achieve a more uniform illumination. A 25 mm diameter plano-convex lens with a focal length of 25 mm was also attached to the laser-pointer head to weakly focus the beam on the chip surface. The purpose of the focusing lens was to concentrate the laser illumination in much the same manner as an objective during epitaxial illumination, but to also narrow the beam width so that it matched the size of the tilted micromirror surface. The chip was placed on a custom made Plexiglas frame and was positioned 25 mm above the lens-laser setup. The web CCD camera was mounted on a Z-axis manipulator to facilitate focusing. The laser diode was attached on a XYZ-axis manipulator to assist alignment. The complete optical setup extended 28 cm in height.

5.2.3.2 TOTAL INTERNAL REFLECTION WITHIN THE BIOCHIP

5.2.3.2.1 Incident angle of illumination and optical coupling efficiency

The incident angle of illumination, θ, in conjunction with the critical angle, θ_C, strongly influenced the properties of the evanescent wave, and was the most important variables when designing TIRFM configurations. The incident angle was established by drawing a ray diagram of the light beam as it passed through the biochip. If the beam was not collimated, the incident angle would have continuously changed along the focused spot. The inner and outer rays of the beam reached the interface at incident angles of 69.6˚ and 71.1˚ respectively, when a glass substrate was used and the light was coupled with an ultraviolet (UV) curable polymer with a similar index of refraction (e.g. Norland 65). Both values were above the critical angle (θ_C=64.8˚, for the worst case scenario of n_2=1.38), so that the entire beam was totally internally reflected. As previously described, the initially collimated beam was focused through a lens with a focal length of 25 mm. The distance between the chip and the lens only altered the size of the focused spot and not the incident angle. Depending on the application, larger spots were obtained if the distance between the lens and the chip was decreased. Such designs can be advantageous for the simultaneous excitation of multiple microchannels.

Replacing the Norland 65 polymer with a polymer of different index of refraction (e.g. Norland 63 or PDMS with index of refraction equal to 1.56 and 1.41, respectively) modified the incident angle of illumination at the interface without having had to adjust the position of the laser beam. Accounting for all changes in indices of refraction (air to bottom glass substrate to polymer to top glass substrate), the inner and outer rays of the beam reached the glass/liquid interface at incident angles ranging from 61˚ to 85˚ by simply changing the index of refraction of the polymer from 1.41 to 1.61 (Figure 117). The change in the incident angle of illumination by employing a polymer with a different index of refraction demonstrated the flexibility of the employed design to adapt to the needs of a specific application.
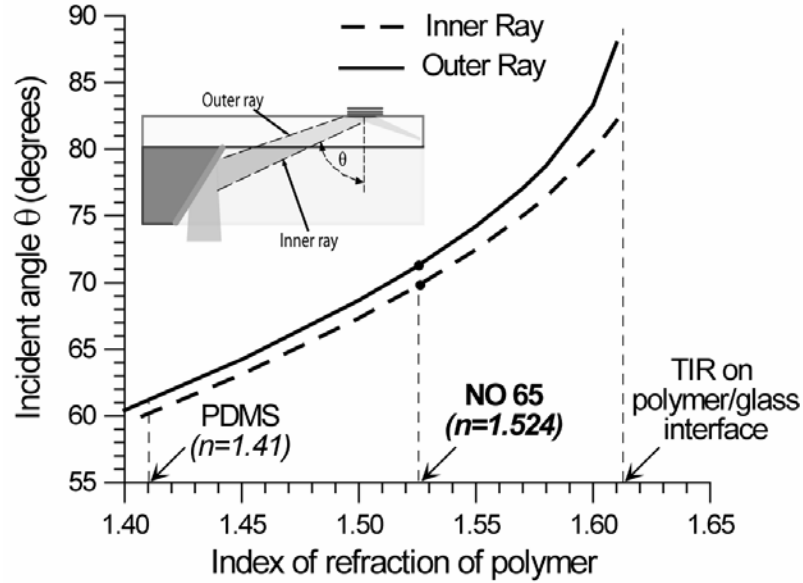
Figure 117. Dependence of the incident angle of illumination on the index of reflection of the UV curable polymer.

Optical adhesive Norland 65 (NO 65) resulted in an incident angle of ~70 degrees. PDMS decreased the incident angle to ~61 degrees.

Utilization of the UV curable polymer provided high optical coupling efficiency, since it significantly minimized the light losses. When a polymer was not incorporated, there was a substantial percentage of light reflected at the air/top glass interface. The parallel (to the plane of incident) and perpendicular components of the reflectivity losses as a function of incident angle at the bottom of the top glass substrate are depicted in Figure 118. The use of Norland 65 reduced the reflectance light losses to 5% of the incident light. If no coupling material was implemented (air/glass interface), the light losses were as high as 35%.
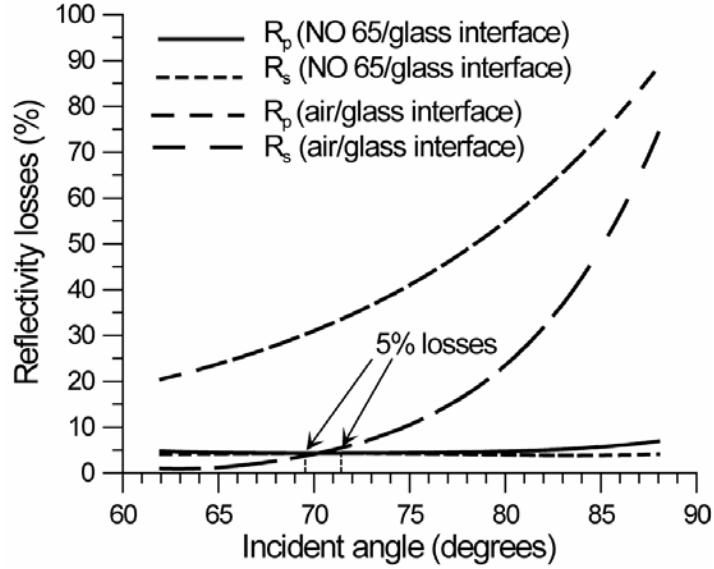
Figure 118. Reflection losses at the air/glass and Norland 65/glass interface.

The subscripts p and s denote components parallel and perpendicular to the plane of incidence, respectively.

5.2.3.2.2 Evanescent Field

A quantitative analysis of the properties of the evanescent field created by the four-layered chip was important in evaluating the range of operation, as well as the limitations of such a configuration, since the emitted fluorescence intensity depended greatly on the s-polarized and p-polarized components of the intensity of the evanescent wave [89]. Figure 119 graphically depicts the dependence of $I_P(0)$ and WAS(0) on the incident angle of illumination for the implemented geometry and materials (Norland AF-65, $n_2=1.38$, $\theta_C=64.81°$). For simplicity the s-polarized and p-polarized incident amplitudes (A_S and A_P) at the interface were assumed to be unity. Large incident angles significantly reduced the evanescent intensities, $I_P(0)$ and WAS(0), and decreased the probability of energy absorption by a fluorophore. The shadowed area corresponded to all the rays with incident angles between the inner and outer rays. The intensity along the focused spot was therefore exponentially decreasing due to the continuous change of the incident angle.
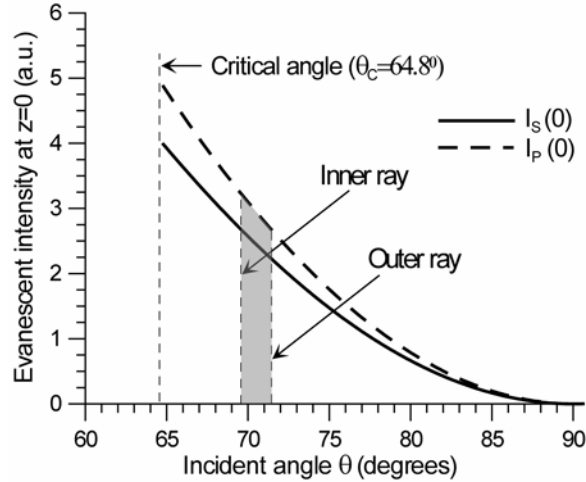
Figure 119. Intensity of the evanescent wave at the interface versus the incident angle.

The chip operated at a range of incident angles within 5-7 degrees of the critical angle.

For supercritical angles within 10 degrees of the θ_C, the evanescent intensity was generally equal to or greater than the incident light intensity [60]. Because the operation range of incident angles ($69.6° < \theta < 71.1°$) of this chip was within 10 degrees of the critical angle, the intensity evanescent wave was enhanced at the interface by 3 times that of the incident light. When it was desired to have uniform illumination, the beam was collimated so a fixed incident angle was obtained. The above results illustrated that the proposed chip design functioned at a range close to the critical angle, which was necessary to produce an evanescent field strong enough to excite fluorescence.

The movement of 1 μm diameter red fluorescent carboxylate-modified microspheres (Molecular Probes Inc.) were observed. These microspheres, which were suspended in deionized (DI) water at room temperature, had an emission maximum at 575 nm when excited by green light (absorption maximum at 535 nm). An interference filter (Optical Omega, XF3021) was used to block green fringing light from the laser source. After a droplet of the suspension was pipetted on the chip, a few seconds were needed for the spheres to settle to the glass surface. Microspheres that were permanently adsorbed to the chip fluoresced continuously, while active microspheres that entered and left the evanescent field due to random Brownian motion imaged as blinking spots. The continuous Brownian motion of free particles was verified by observing them with a light microscope.

Figure 120 shows a sequence of video frames of the motion of a single microsphere (exposure time was set to 33 ms). The sphere was observed to slowly move away and separate (b) from a neighbouring sphere that was attached to the substrate. After separation, the microsphere started moving out of plane, gradually leaving the evanescent field (c). A reduced intensity was observed, and when it finally exited the field, no fluorescence signal was observed (d). Several microspheres stuck together and adsorbed to the chip surface, and were visualized as a fluorescent spot of larger dimensions.
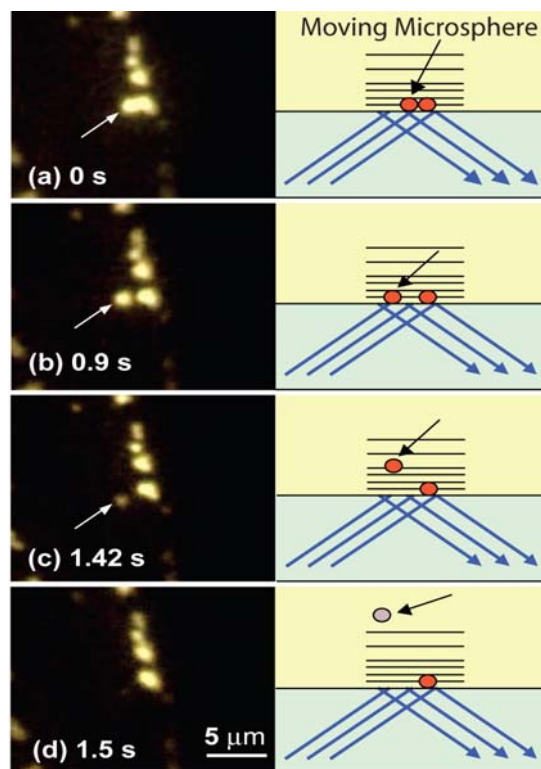
Figure 120. Recording the Brownian motion of a single 1 μm fluorescent microsphere.

A two dimensional intensity profile of the TIR region was imaged by depositing Rhodamine 6G (R6G) inside the microfluidic network (Figure 121). Positively charged Rhodamine molecules were precipitated on the negatively charged glass surfaces of the microfluidic channel during the evaporation of 10 μL of 10 pM concentration of R6G in methanol.
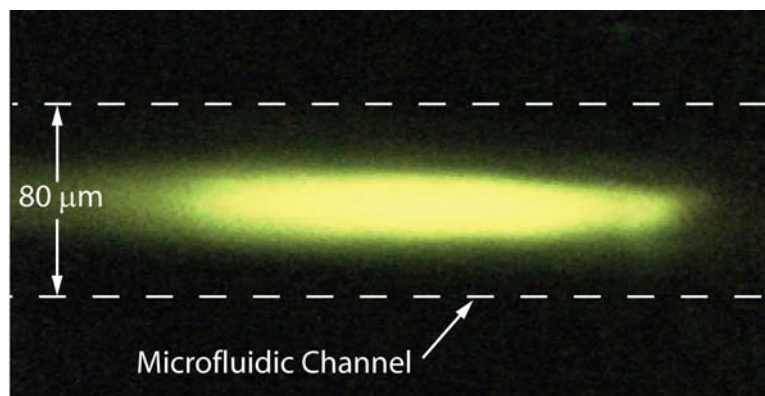
Figure 121. Photograph of the intensity profile of the TIR region in air.

Visualized upon coating the bottom of the microfluidic channel with Rhodamine 6G.

133

In a similar experiment, 10 µL of 10 fM and 500 fM concentrations of R6G were used. After complete evaporation (typically after 1-2 minutes), the Rhodamine fluorescence intensity was recorded. All the experiments were performed in a dark room. The output optical power of the laser was 2.6 mW (measured with an optical power meter, Newport 1830-C). The normalized fluorescent intensity curves for 10 fM and 500 fM concentrations (Figure 3.85) were consistent, yielding a photo-bleaching rate constant in air of 0.22 s^{-1} and 0.18 s^{-1} respectively. To measure the fluorescent intensity, image processing software (Scion Image) was used to determine the average intensity (per pixel) of a 25x15 pixel region within the TIR spot. The background was measured similarly on a 25x15 pixel region outside the TIR spot, and was then subtracted from the average fluorescent intensity. Typical signal to background ratios (SBRs) at t=0 were 13.4 and 7.9 for 500 fM and 10 fM, respectively. The exposure time was 67 ms. Due to the limited dynamic range of the web camera, it was not possible to quantify higher concentrations due to signal saturation.

Methanol evaporation began at the inlet and outlet of the microfluidic network. Consequently, the bulk of Rhodamine molecules in solution were carried towards the TIR region during evaporation (the TIR region was located in the middle of the microfluidic network). For this reason a large fraction of the original number of molecules in solution were deposited close to the TIR region.
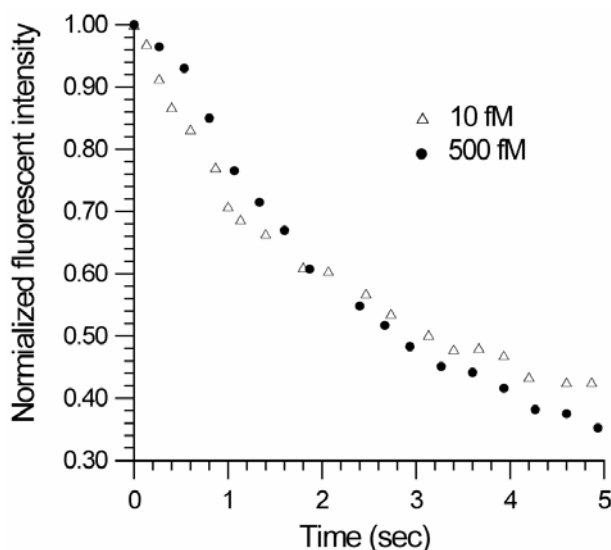
Figure 122. Normalized photo-bleaching curves for Rhodamine 6G.

After 5 s the signal was reduced to 35% of the initial value. The exposure time was 67 ms.

Because of the uncertainty of the number of molecules deposited in the TIR region, an estimate of the actual number of molecules that were detected was not possible. In filled microchannels, Rhodamine molecules accumulated over time on the glass surface, while previously precipitated ones were being photo-bleached. The

fluorescent intensity was determined in a dry environment where the number of molecules adsorbed on the surface was known.

5.2.3.3 DESIGN MODIFICATIONS FOR SINGLE MOLECULE DETECTION

The portable TIR system that is described above had a single TIR detection site and was able to detect femto-molar concentrations. To achieve single molecule detection, the sensitivity of the overall system needed to be improved and the background noise needed to be reduced. To achieve a higher sensitivity, the web camera was the first component that needed to be replaced. Intensified video cameras and back-illuminated CCD sensors were the best option, providing excellent quantum efficiency ($C_{CCD} \approx 95\%$) for a back-illuminated camera, but were 2000 times more expensive than a web CCD camera. Those cameras combined with conventional TIR setups were capable of reaching the ultimate sensitivity limit necessary for detecting single molecules.

The optical efficiency of the system also depended on the numerical aperture (NA) of the lens as well as the quality of the filter (lenses with higher NA collect more photons than lenses with a lower NA). The overall optical efficiency of the system C_{total} was calculated from the following expression:

$$C_{total} = \frac{\#Photoelectrons\ \ Detected}{\#Photons\ \ Emmited} = C_{filter}C_{objective}C_{CCD} \qquad (24)$$

where $C_{filter} = \int F(\lambda)T_{filter}(\lambda)d\lambda$ is the filter efficiency. $T_{filter}(\lambda)$ is the transmission function of the filter, and $F(\lambda)$ is the intensity spectrum of the fluorophore.

$$C_{objective} = \frac{1}{2}\left[1 - \left(\sqrt{1 - \left(\frac{NA}{n}\right)^2}\right)\right] \qquad (25)$$

is the objective efficiency. The index of refraction of the lens material is n.

$$C_{CCD} = \int F(\lambda)T_{CCD}(\lambda)d\lambda \qquad (26)$$

is the CCD efficiency. Figure 123 illustrates the detection spectrum of the fluorescence emitted by the Rhodamine 6G molecules that were detected by a state-of-the-art back-illuminated camera through a 40x/0.6NA objective using a high quality filter (Optical Omega, XR3002). Those modifications were easily incorporated in the current TIR system to achieve single molecule detection capabilities.
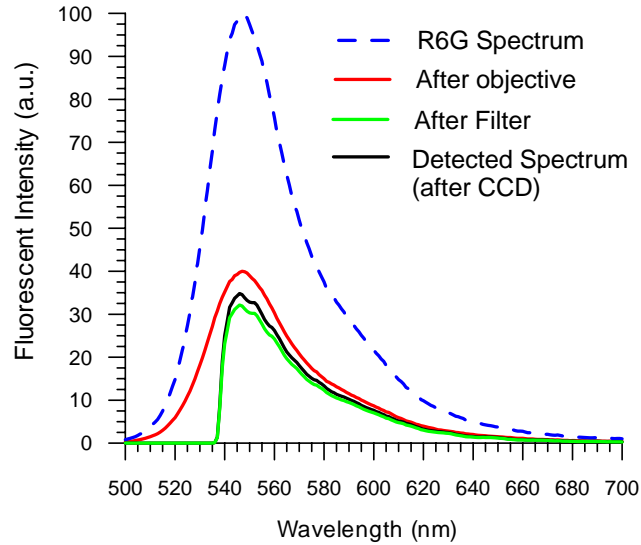
Figure 123. Detected fluorescent spectrum emitted by R6G passing through the various optical components.

The overall optical efficiency of the system was $C_{total} = 6.5\%$. The objective was the limiting factor.

Special care was taken for minimizing the auto-fluorescence of the glass substrate. Quartz has the lowest level of fluorescent impurities and was therefore the material of choice (AF-75 glass was used in the TIR chip). Background auto-fluorescence from the UV curable polymer also decreased the signal to noise ratio. For example, Norland 65 adhesive has a higher auto-fluorescence when excited with a green (535 nm) laser compared to PDMS (Figure 61). The selection of the lower fluorescent polymer that matched the index of refraction of the top glass substrate was therefore critical for reducing the background noise.
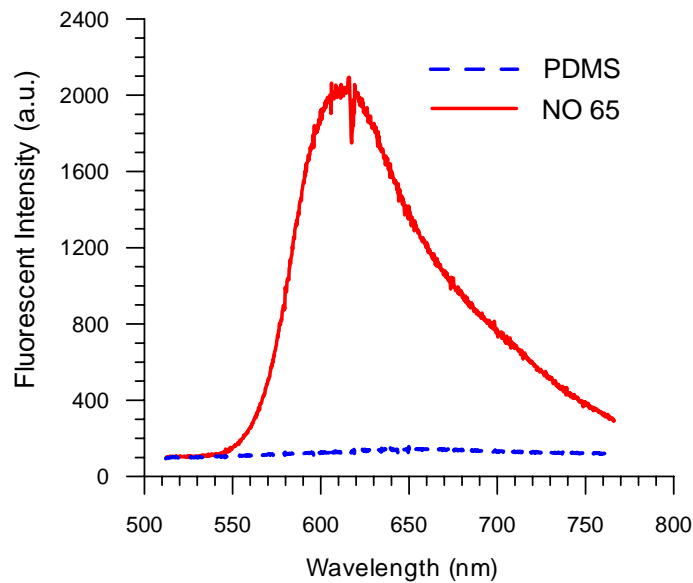
Figure 124. Fluorescence spectrum of Norland 65 (NO 65) and PDMS.

Excitation was with a green laser (535 nm) and an Acton Research SpectraPro 300i Spectrometer.

Having made those two modifications in the chip design (replaced NO65 with PDMS and use of a quartz wafer), a state of the art CCD detector (Cascade 512B, back-illuminated CCD from Roper Scientific) was used to detect single Rhodamine molecules in a flowing stream. That camera had a sensitivity of more than 90% in the visible range, and can record up to 400 frames per second. The microfluidic design was modified so that the evanescent field propagated perpendicular to the flow. The new microfluidic design incorporated a 1.5 micron thick and 7 microns wide PDMS channel. The TIR site was 10 microns wide, so that the total excitation volume was 7 attoliters (the evanescent field was 0.1 microns thick). The chip and laser diode were mounted on an inverted microscope using custom made Plexiglas frames.

A syringe pump was used to induce flow of the Rhodamine molecules at a rate of 1 microliter per hour. The concentration used was 1 pM of Rhodamine in methanol. Figure 125 shows a photograph taken over a10 msec exposure time of the flowing stream using a 40x objective. After subtraction of the background noise and setting up a cut-off threshold of 1.3 times of the background noise, single molecules were observed in the flowing stream. Because the Signal/Noise ratio was quite low (~1.5-2), it was concluded that the blinking pixels corresponded to single molecules, since the blinking pixels did not appear in subsequent frames. Molecules that were rapidly moving due to translation or molecular diffusion occupied two pixels (one pixel corresponds to 0.5 microns).

Before background subtraction

Flow direction

After background subtraction

Two adjunct pixels denote
molecular diffusion

7 µm
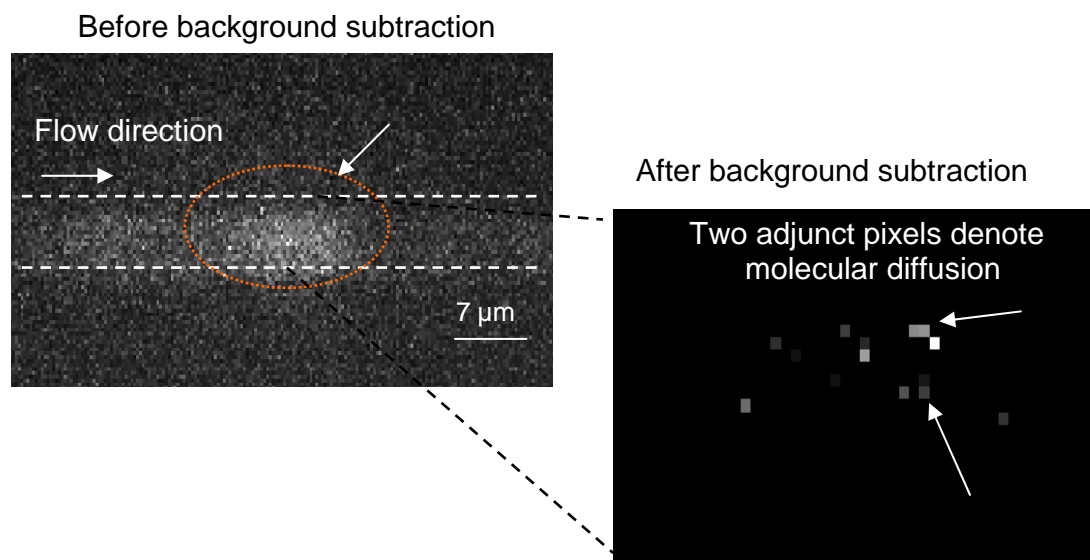
Figure 125. Single Molecule Detection in a flowing stream using the TIR excitation scheme.

5.2.4 SELF-ALIGNED INTEGRATED MICROFLUIDIC OPTICAL SYSTEMS (SIMOS)

Figure 126 (a) shows the sidewall of the mold after deep reactive ion etching (DRIE). The DRIE method resulted in the scallops on the sidewall [86]. These scalloped surfaces were not desirable since there was light scattering on the replicated PDMS surface from the mold. Anisotropic potassium hydroxide (KOH) and isopropyl alcohol (IPA) wet etching [87] and oxidation/wet-etching [99] have been shown to make smooth surfaces of etched sidewalls. This isotropic wet etching method was used here since the curved surfaces of the planar microlenses that did not follow the crystal orientation. Figure 126 (b) shows the effect of the 5 min silicon wet etching, following DRIE. The scallops on the sidewall were smoothed. Before the silicon wet etching, the height of the rough surface was 100 nm. But after the 5 min silicon wet etching, it decreased to less than 20 nm, as shown in the SEM micrographs. Reflection measurements of a sidewall are shown in Figure 127. Average reflectances verses etch time are also presented in Table XIV. As the roughness of the sidewall decreased by the silicon wet etching, the reflectance increased. Refinements are in progress to further improve the quality of these types of surfaces.
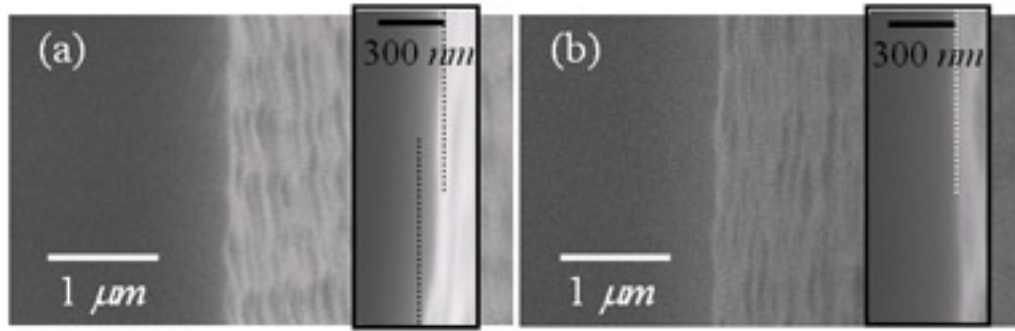
Figure 126. The etched sidewall surface of the mold.

(a) After DRIE, and (b) After DRIE and 5 min in silicon wet etching solution.
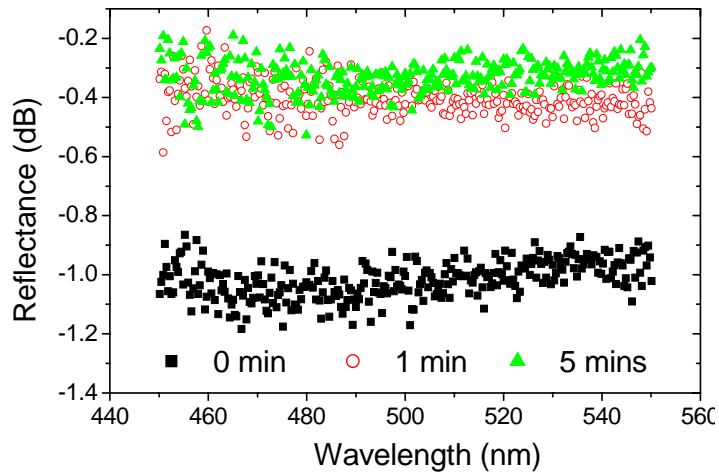
Figure 127. Reflectance of the etched sidewall surface of the mold according to the silicon wet etching conditions.

Table XIV. Average reflectance verses etch time

	0 min	1 min	5 min
Average reflectance (dB)	-1.02	-0.40	-0.33
Average reflectance (%)	(79.1 %)	(91.1%)	(92.7%)

Four other designs were fabricated and tested, and the measured amplification and NA of these designs are summarized in Table XV.   Figure 128 shows the spectrum analysis of the emission from these designs. The applied voltage to the LED was 3.7V and the concentration of the fluorescent solution was 0.5% solid concentration. Each spectrum included two major peaks at 466nm and 515 nm.   The relatively smaller peak at 466nm came from the light emitting diode (LED), which had a wide bandwidth and a main peak at 466 nm. The larger peaks at 515 nm were fluorescent emissions from the fluorescent dye. With the same excitation conditions and concentrations of fluorescent dye, Design 4 had the highest fluorescence intensity. Even though the excitation light did not reach the detector in the orthogonal directions along the optical paths, the peaks around 466 nm of came from the scattered excitation light due to imperfections in the PDMS surfaces.

Table XV. Fluorescence amplification and numerical aperture

	2-D NA of the planar microlenses	Fluorescence amplification (%)
Design 1	0.53	260
Design 2	0.66	427
Design 3	0.69	549
Design 4	0.91	2840
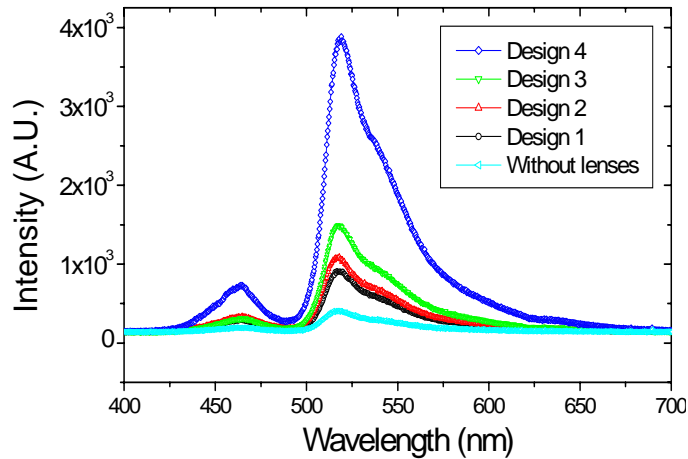
Figure 128. Spectrum of fluorescent emission.

The applied voltage to the LED was 3.7 V. The distance between the LED and the microfluidic device was 40 mm. The channel was filled with 0.5 % fluorescent dye and water. The equivalent fluorescent molar concentration was $7.98 \times 10\text{-}5$ M.

Figure 128 shows the CCD images of the fluorescent emissions of these designs. With the different designs of the high NA planar microlenses, different configurations of fluorescent emission were obtained, as shown by the respective condensed beam profiles of the excitation light. The brightest emission was at the focus point of the planar microlenses of Design 4. The measured NA in Design 4 was 0.91, which was smaller than expected. It was determined that the non-collimated exciting source of LED contributed to the smaller NA. The shorter optical path length in the microfluidic channel and the high NA contributed to the higher amplification in Design 4. Higher NA planar lenses correlated with the higher amplification of the fluorescent signals. Figure 128 also shows the amplification of the fluorescent intensity of a design without planar microlenses. The fluorescence intensity was 28 times higher than without any microlenses.
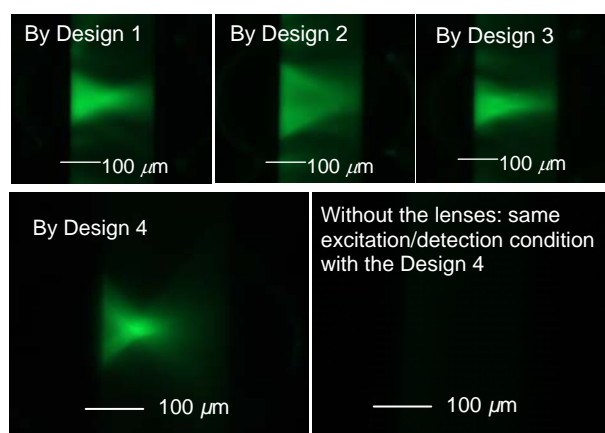
Figure 129. Fluorescent excitation by the various high NA planar microlenses and without the planar microlenses.

The applied voltage to LED was 3.7V. The distance between the LED and the microfluidic device was 20 mm. The channel was filled with 2.5 % fluorescent dye. The images of fluorescence emission were captured by 30× objective lenses and a charge coupled device (CCD). The times for exposure were 200, 100, 200 and 300 msec for Design 1, 2, 3 and 4, respectively.

5.2.5 INTEGRATED MICROFLUIDIC OPTICAL SYSTEMS (SIMOS) FOR SINGLE MOLECULE DETECTION

A portable system for single molecule detection using optical components and an avalanche photodiode, as shown in Figure 130, was also fabricated to test the capability of detecting single molecules. The integrated planar microlenses in this design decreased the excitation volume to a few hundred picoliters (pl). In addition, the excitation volume was decreased to a few hundred of femtoliters (fl) when coupled with hydrodynamic focusing of fluidic channels. This decreased excitation volume maximized the possibility of detecting single molecules. Also, by using integrated planar microlenses, the optical fiber couplings for excitation were eliminated. The excitation source (635 nm laser diode) was directly coupled with the integrated planar microlenses and focused on the center of microfluidic channel. The orthogonal excitation and detection increased the

signal-to-noise ratio in this portable system. Because the beam paths between excitation and emission were not in parallel, the reflections from each optical component did not contribute to the signal as with previous configurations.
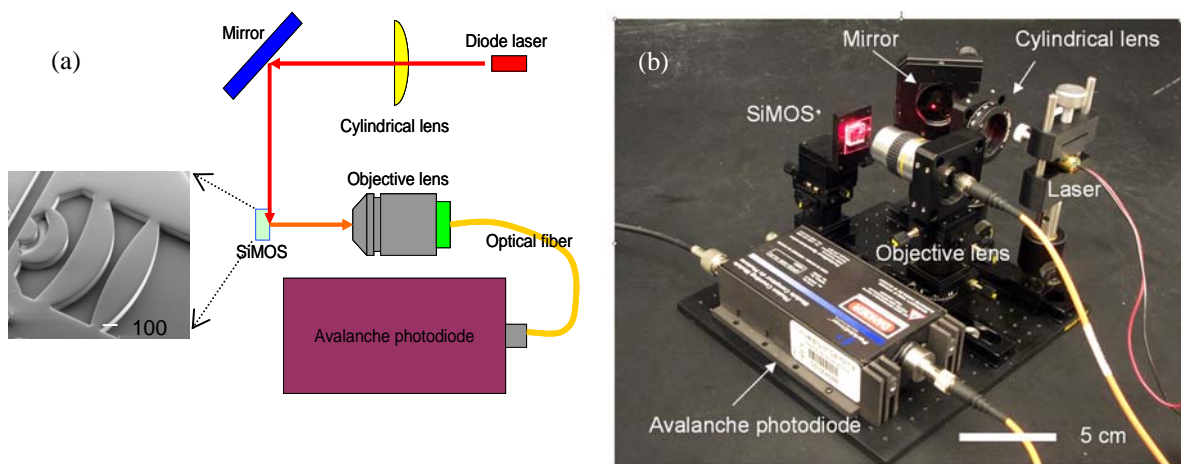
Figure 130. The portable SiMOS system for single molecule detection.

(a) Schematic drawing of the excitation and detection design, and (b) Portable set-up.

For the preliminary tests, the microfluidic channel was filled with 5 nM of Alexa Fluorophore™ 647 (647/667 nm). The fluorescence was detected with the avalanche photodiode with 635 nm laser diode excitation. The fluorescence was filtered with a 660 nm long pass filter. The fluorescence detections by photon counting are shown in Figure 131, and were compared with water in the microfluidic channel. Based on the excitation volume (350 pl) and concentration (5nM), the amount of Alexa Fluorophore™ 647 detected was less than 2 attomoles (1.8×10^{-18} mol).
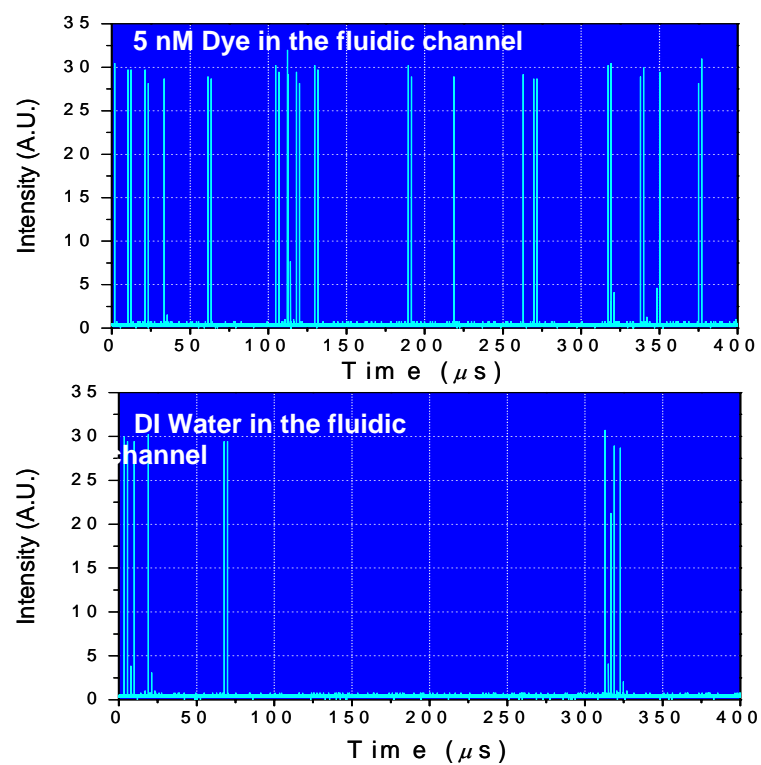
Figure 131. The raw TTL signals from the avalanche photo diode generated by the photon bursts of fluorescence emission in SiMOS.
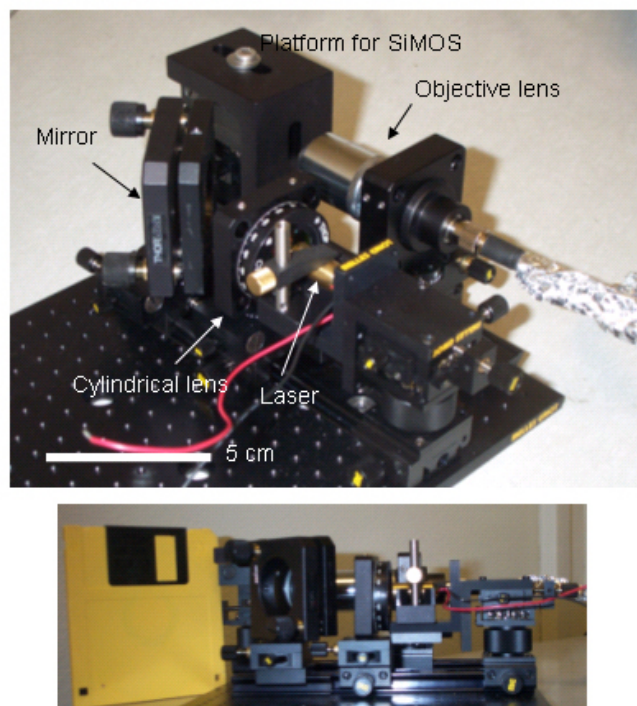
Figure 132. Portable SiMOS system including the excitation source (the avalanche diode is not shown).

After the evaluation module of single molecule detection for SiMOS was tested, an improved portable module was suggested and built based on the evaluation module. To improve the portability, a mirror, an excitation source, a lens, an objective lens and a platform for SiMOS were tightly packed within a volume of 15 cm (length) × 10 cm (width) × 7 cm (height) (not including an avalanche photo diode). If the size of the XYZ stages that were only needed to initially align the components were excluded, the volume of the module would have been 10 cm (length) × 10 cm (width) × 3 cm (height). This is the smallest volume that a micro-system has been built in that detected such a small volume of material. However, even in this configuration, there is still the possibility for improvement, because the adapted commercial optical components were large, compared with the SiMOS. If every component can be replaced with integrated MEMS components such as the mirrors, the excitation source and the detector, then the size of the detection system will decrease even more.
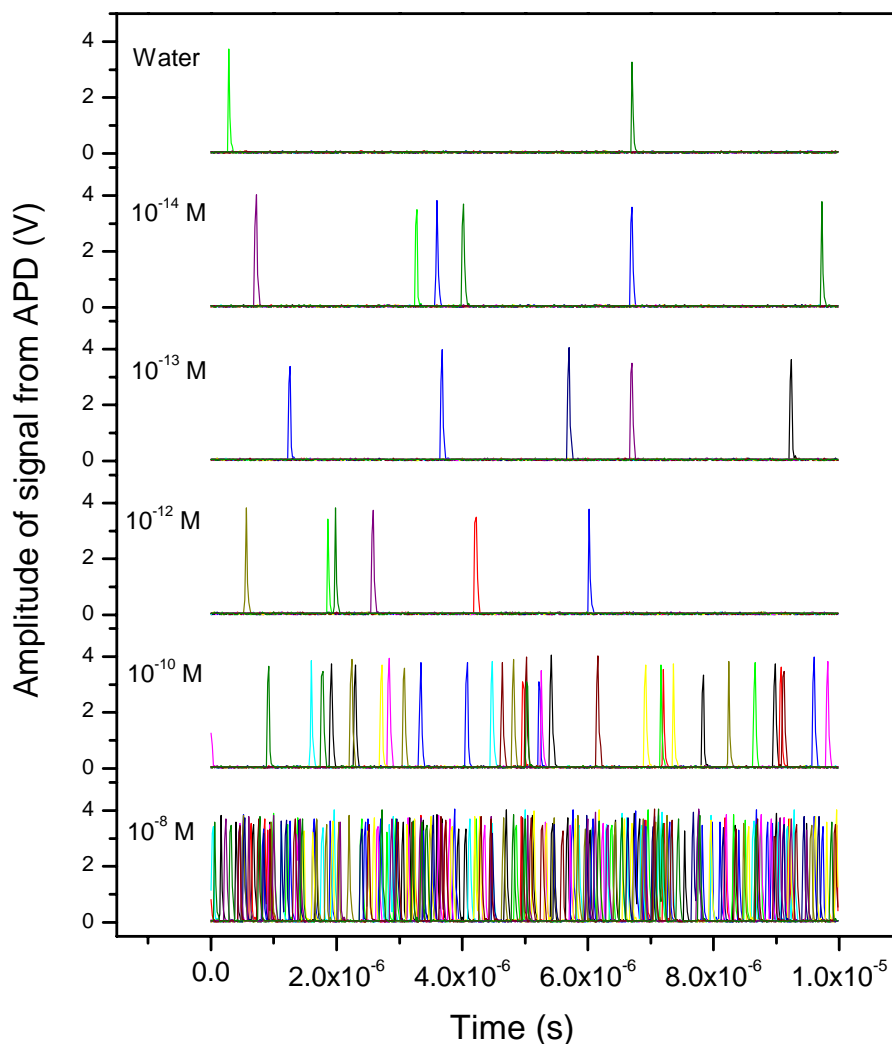
Figure 133. The raw TTL signals.

Photon bursts of fluorescence emission in SiMOS verses different concentrations (average of 12 measurements).

As a demonstration of single molecule detection with SiMOS, a microfluidic channel was filled with six different concentrations from 10^{-8} M to 10^{-14} M of Alexa Fluorophore™ 647 (647/667 nm) and deionized water. The fluorescence was achieved with a 635 nm laser diode excitation, was filtered with a 660 nm long pass filter, and was detected with the avalanche photodiode. The fluorescence detections by photon counting are shown in Figure 133. Based on the collected raw signals from the avalanche photo diode, the minimum detectable concentration was 1 pM. With an excitation volume of 750 pl and a concentration of 1 pM, the detection concentration was 750×10^{-24} mol (yoctomoles). One molecule is equal to 1.6×10^{-24} mol, so that the detection limit was

470 molecules. Adapting data acquisition with a counting computer card and integrating the acquisition time to milliseconds is expected to improve the detection capability even further.

6. CONCLUSIONS

6.1 SYSTEM COMPONENTS

6.1.1 DISPLACEMENT VERITCAL ACUATORS

Low voltage and large static displacement vertical actuators were fabricated and demonstrated with integrated microlenses on high aspect ratio silicon-on-insulators (SOI's). Because of the buried coupled torsion flexure and the isolated vertical comb banks with pre-engagement, the vertical piston motions of microlenses were demonstrated to have large displacement distances when activated by low driving voltages. These devices were not only a key part of the continuing effort to develop μCIA, but this architecture is also attractive for other photonic devices.

6.1.2 2-D GIMBALED MIRRORS

A backside island isolation method for SOI MEMS technologies was developed and demonstrated for vertical comb-drive based 2-D gimbaled micromirrors with large static rotation. The backside island isolation provided electrical isolation and mechanical coupling of SOI structures without additional dielectric backfill and planarization. This architecture also provided an additional structural layer by utilizing an etched handle wafer as a hidden device layer. Incorporation of the backside island isolation method into a vertical comb drive was also demonstrated.

A two-axis micromirror was used as a scanning mirror for the laser scanning confocal microscope and laser scanning displays. Moreover, the backside isolation method was applied to other micro-optical components. A single layered 2-D microlens scanner was implemented as a substitute of the stacked 2-D microlens scanner by designing nested, isolated lateral comb-drives. Convex microlenses were molded by using the backside island as the bottom of ring shaped lens holder.

6.1.3 MICROBARICATED ROBOTIC WORKSTATION

A microfabricated, robotic workstation was constructed for single cell manipulation. The microrobotic platform consisted of electro-thermal SU-8 actuators, and was capable of handling and mechanically stimulating single cells in physiological media. The key element in the actuator design was the use of a high coefficient of thermal expansion polymer (SU-8) as a structural material that provided the desired motion and force at low voltages (1.5-2.5 V) and low temperatures (22 $^{\circ}$C). Hundreds of such microrobotic workstations fabricated on a single chip could potentially replace conventional, expensive, low-throughput single cell analysis setups.

6.1.4 SELF-ALIGNED VERTICAL COMB -DRIVE

A novel fabrication method for fabricating self-aligned vertical comb-drives was demonstrated. The vertical offset was determined by the residual stress in a bimorph cantilever anchoring fixed comb. The vertical amplitude of the piston motion at the resonant frequency of 3.5 kHz was 30 μm. In torsional motion, the angle of optical deflection at the resonance of 830 Hz was changed by 6.5°. The measured resonant frequencies corresponded to the results from a finite element analysis within 10%. The optimal design of the mechanical suspension improved the stability of the device as well as the static DC control, which had compromised the vertical offset variation. This method for fabricating micro-optical components with out-of-plane motion on a SOI wafer is suitable for providing high speed and precise position control at low cost with high optical performance for many optical and biophotonic MEMS applications.

6.2 MICROSCALED SYSTEMS

6.2.1 CONFOCAL LINE SCANNING SYSTEM

A MEMS confocal line scanning system was demonstrated, which will dramatically reduce the size and cost of lab-on-a-chip systems by using micromachined optical components. The miniaturized confocal line scanning system will be especially beneficial to multichannel microfluidic chips, i.e. multiplexed genomic and 2-D protein chips.

6.2.2 MINATURIZED SCANNING CONFOCAL MICROSCOPE

A miniature scanning confocal microscope was developed using micromachining (Figure 134). Electrostatically actuated microlenses provided the focusing and scanning. By stacking objective lenses, scanners, a pupil, and a pinhole, the confocal microscope was microfabricated and integrated in a volume smaller than 2 mm^3. Objective lenses consisted of two vertically cascaded polymer microlenses integrated with micromachined comb-actuators. Raster scanning was implemented by electrostatically actuating each microlens in orthogonal directions. Reflection confocal imaging was demonstrated with a 3 μm transverse resolution over a 100 μm field of view and a 0.38 mm working distance at λ= 633 nm. This MEMS microscope can be batch manufactured, arrayed and combined with microfluidics for advanced lab-on-a-chip systems.
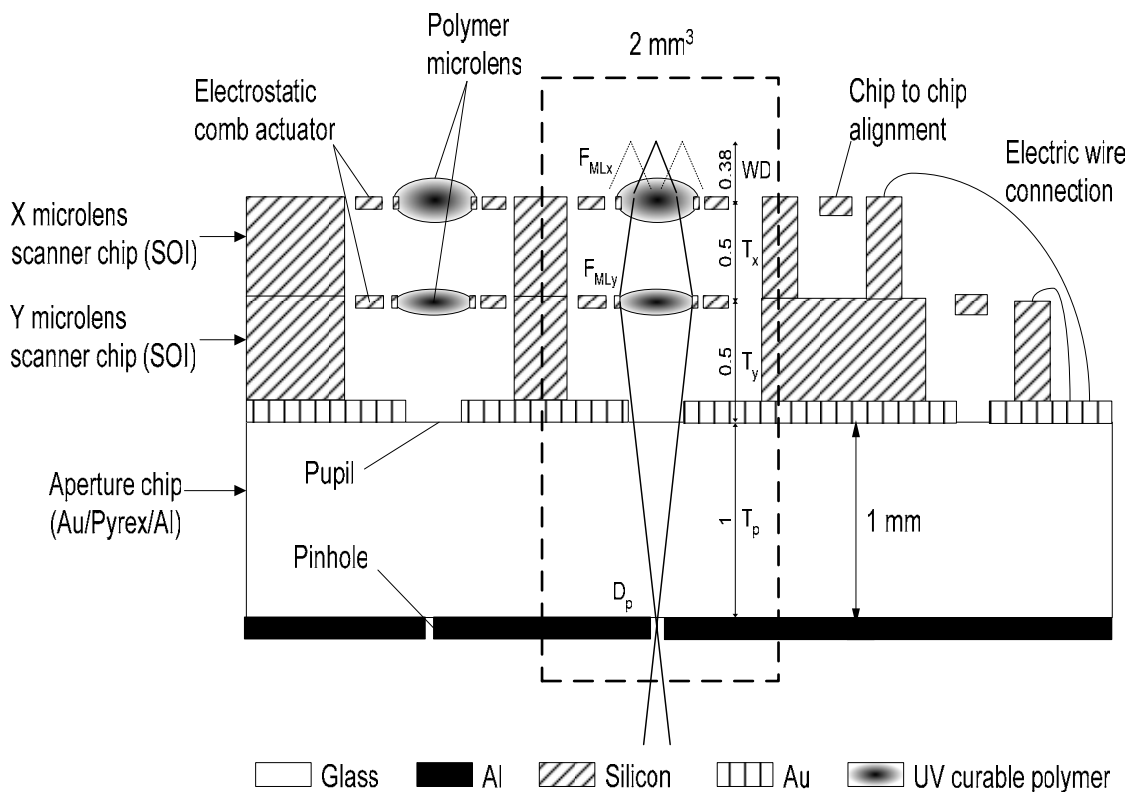
Figure 134. A side view of the device architecture of the micromachined transmissive scanning confocal microscope.

The objective lens, scanners, pupils, and pinholes are vertically integrated.

6.2.3 RAMAN SCATTERING SYSTEM

Nanoscale metallic structures on silicon and PDMS chips were fabricated and tested. In comparison with the on-chip SERS substrate made by E-beam lithography [52,53], the present fabrication technique was compatible with standard microfabrication technology, which enabled the monolithic large-scale integration of SERS substrates on silicon and with polymer-based biochips. The Raman spectrums of R6G and adenine molecules were detected on these SERS substrates. The Raman scattering intensities were determined to be more than 10^3 times more intense compared to that of similar samples on smooth silver substrates. The direct integration of such substrates with the micro- or nano-fluidics to implement sample delivery and manipulation is depicted in Figure 135. Packaging of the SERS substrate with the scanning microlens will be a major part of future work. The precise control of the optical path and light coupling to the detector are two key packaging issues that need to be addressed.
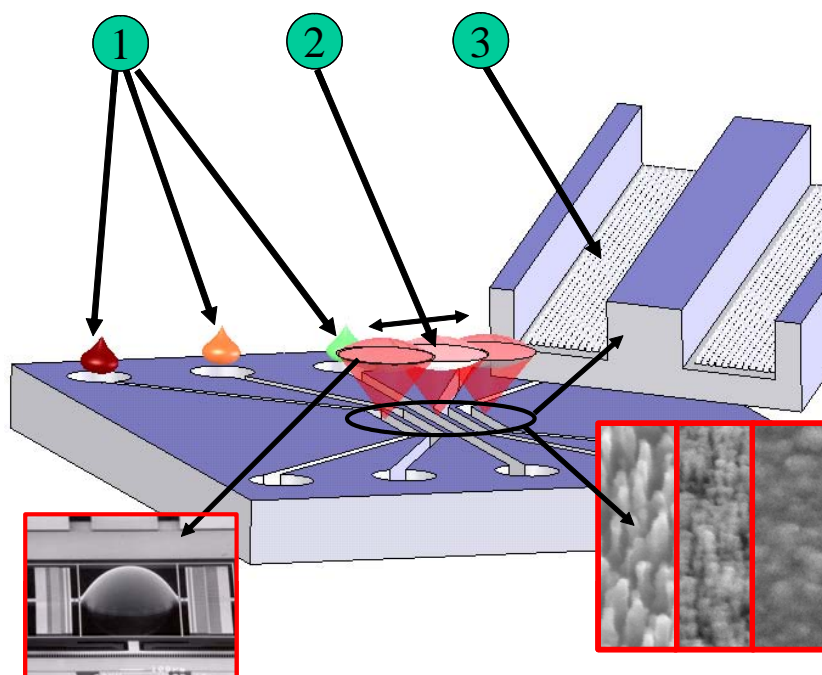
Figure 135. Illustrations of the future works on the SERS-on-a-chip system for multiplexing single molecule detection.

6.2.4 MINIATURIZED TOTAL INTERNAL REFLECTION (*M*TIR) ANALYSIS SYSTEM

One of the advantages of the TIR design was the vertical assembly of the laser source with the micromirror. That design allowed the integration of a VSCEL (vertically surface cavity emitted laser) array directly beneath the TIR chip with no need of any external optics (Figure 136). The single-site TIR chip was thus transformed to a 2-dimensional multiplexed TIR array with an integrated light source for high-throughput applications.
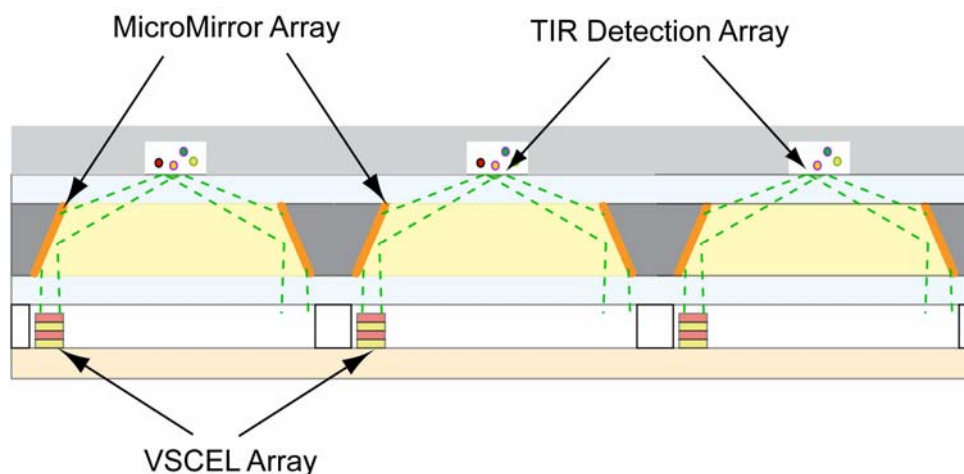
Figure 136. A total internal reflection array for multiplex bioassay.

6.2.5 SELF-ALIGNED INTEGRATED MICROFLUIDIC OPTICAL SYSTEM (SI-MOS)

Disposable SiMOS's with high NA planar microlenses were successfully demonstrated for cost effective lab-on-a-chip design and fluorescence amplification. The planar compound microlenses were self-aligned with microfluidic channels for biochip applications. The SiMOS's had several advantages such as disposability, controllability of optical characteristics, self-alignment, simplified fabrication processing and increased Signal/Noise ratio. The fluorescent emission was amplified 28 times more than without the planar compound microlenses. The portable single molecule detection module utilizing SiMOS was also demonstrated with a detection limit of several hundreds of yoctomoles. The versatile designs of the disposable SiMOS will provide a new paradigm of integrating self-aligned optical systems and detecting fluorescent signals for biochemical analysis systems.

6.3 FUTURE DIRECTIONS

Although the confocal imaging of a MEMS microscope has been demonstrated, the full array operation of confocal microscopes has not yet been demonstrated. That's mainly due to the need for the development of an integrated array of diode lasers and photodiodes. Future research directions include the ultimate integration of these components, as proposed in Figure 137.
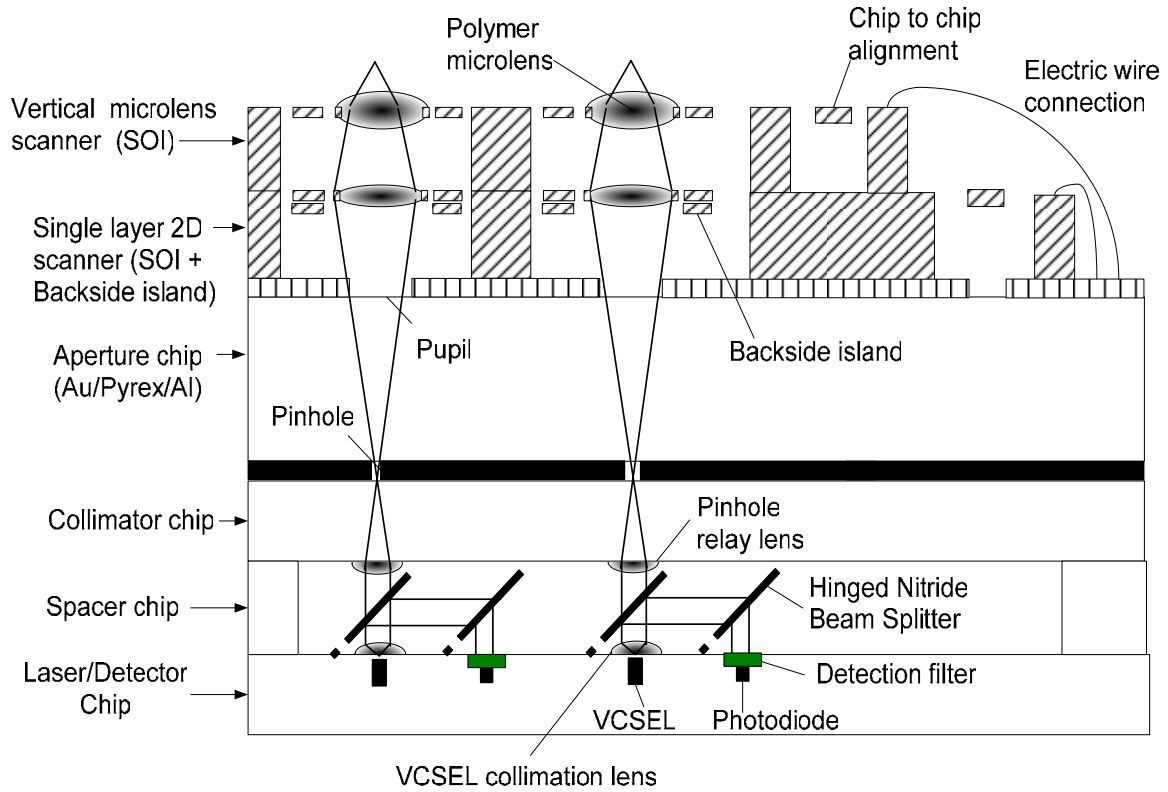
Figure 137. Conceptual design of future integration of micromachined transmissive scanning confocal microscope.

New components include single layer 2-D microlens scanner by backside island, vertical microlens scanner, hinged nitride beam splitter, detection filter, collimation lenses, VCSELs, and photodiodes.

There are several new components and ideas that also need to be investigated. First, vertical cavity surface emitting lasers (VCSELs), hinged nitride beam splitters, and photodiodes could be added at the bottom layer, replacing the off-the-shelf components that are currently being used. The hinged beam splitter would be fabricated as a nitride membrane framed by hinge structures, enabling a full 45 degrees tilt of the beam splitter. Second, the stacked 2-D microlens scanner could be replaced with a single layer 2-D microlens scanner with a backside island. On top of the single layer 2-D scanner, the vertical microlens scanner would be stacked. In this way, complete 3-D raster scanning with an integrated light source and detector would be possible.

Once a full operating array is completed, the research direction should be applying the MEMS confocal microscope array to various parallel imaging applications. For example, combination of the array with a single cell patch clamp array would be useful to various drug screening based on the phenotype change of cells. The illumination optics, with some small modifications, would be directly applied to scanning display applications. Conventional laser scanning confocal microscopes that are widely used in biological imaging and metrology are bulky bench-top instruments requiring samples to be placed in the microscope. Size reduction and portability are desired for applications such as *in vivo* imaging, planetary investigation, and handheld micro total analysis systems.

7. REFERENCES

[1] G.F. Marshall, *Optical Scanning*, New York: Marcel Dekker, Inc., 1991.

[2] H. Urey, "Torsional MEMS scanner design for high-resolution scanning display systems," *Proc. SPIE - Optical Scanning 2002*, 27-37 (2002).

[3] R.A. Conant, P.M. Hagelin, U. Krishnamoorthy, M. Hart, O. Solgaard, K.Y. Lau, and R.S. Muller, "A raster-scanning full-motion video display using polysilicon micromachined mirrors," *Sensors & Actuators A (Physical)*, 83, 291-296 (2000).

[4] D.L. Dickensheets and G.S. Kino, "Silicon-micromachined scanning confocal optical microscope," *J. Microelectromechanical Systems*, 7, 38-47 (1998).

[5] W. Piyawattanametha, P. R. Patterson, G.D.J. Su, H. Toshiyoshi, and M.C. Wu, "A MEMS non-interferometric differential confocal scanning optical microscope," *Proc. 11th International Conference on Solid State Sensors and Actuators*, 590-593 (2001).

[6] B. Warneke, M. Last, B. Liebowitz, and K.S.J. Pister, "Smart Dust: communicating with a cubic-millimeter computer," *Computer*, 34, 44-51 (2001).

[7] M.C. Wu, L.-Y. Lin, S.-S. Lee, and K.S.J. Pister, "Micromachined free-space integrated micro-optics," *Sensors and Actuators A (Physical)*, 50, 127-134 (1995).

[8] H. Dooyoung, S. Huang, N. Hung, C. Hsin, M. C. Wu, and H. Toshiyoshi, "A low voltage, large scan angle MEMS micromirror array with hidden vertical comb-drive actuators for WDM routers," *Optical Fiber Communications Conference (OFC)*, 92-93 (2002).

[9] U. Krishnamoorthy, L. Daesung, and O. Solgaard, "Self-aligned vertical electrostatic combdrives for micromirror actuation," *Journal of Microelectromechanical Systems*, 12, 458-64 (2003).

[10] P.M. Hagelin and O. Solgaard, "Optical raster-scanning displays based on surfacemicromachined polysilicon mirrors," *IEEE Journal of Selected Topics in Quantum Electronics*, 5, 67-74 (1999).

[11] G.D.J. Su, H. Toshiyoshi, and M.C. Wu, "Surface-micromachined 2-D optical scanners with high-performance single-crystalline silicon micromirrors," *IEEE Photonics Technology Letters*, 13, 606-608 (2001).

[12] H. Schenk, P. Durr, D. Kunze, H. Lakner, and H. Kuck, "A resonantly excited 2D-micro-scanning-mirror with large deflection," *Sensors & Actuators A(Physical)*, 89, 104-111 (2001).

[13]   S. Kwon, V. Milanovic, and L. P. Lee, "A High Aspect Ratio 2D Gimbaled Microscanner with Large Static Rotation," *Conference Digest. 2002 IEEE/LEOS International Conference on Optical MEMS*, 149 -150 (2002).

[14]   S. Decal, Y. Ching, and M. Rosa, "Scanning microlens shuttles fabricated using silicon-on-insulator wafers," *Proc. IEEE Solid-State Sensor and Actuator Workshop,* 259-262 (2000).

[15]   A. Tuantranont, V. M. Bright, J. Zhang, W. Zhang, J. Neff, and Y. C. Lee, "MEMS-controllable microlens array for beam steering and precision alignment in optical interconnect systems," *Proc. IEEE Solid-State Sensor and Actuator Workshop,*101-104 (2000).

[16]   H. Toshiyoshi, G. D. Su, J. LaCosse, and M. C. Wu, "A surface micromachined optical scanner array using photoresist lenses fabricated by a thermal reflow process," *Journal of Lightwave Technology*, <u>21</u>,1700-1708 (2003).

[17]   R. Klug and K. H. Brenner, "Implementation of multilens micro-optical systems with large numerical aperture by stacking of microlenses," *Applied Optics*, <u>38</u>, 7002-7008 (1999).

[18]   S. Kwon and L. P. Lee, "Stacked two dimensional micro-lens scanner for micro confocal imaging array," *Proc. Fifteenth IEEE International Conference on Micro Electro Mechanical Systems*, 483-486 (2002).

[19]   R. Conant, J. Nee, K. Lau, and R. Muller, "A flat high-frequency scanning micromirror," *Proc. Solid-State Sensor and Actuator Workshop*, 6-9 (2000).

[20]   Y. Kawata, "Three-dimensional memory," *Proc. of the SPIE - The International Society for Optical Engineering,* <u>4081</u>, 76-85 (2000).

[21]   A.P. Lee, C.F. McConaghy, P.A. Krulevitch, E.W. Campbell, G.E. Sommargren, J.C. Trevino, "Electrostatic comb drive for vertical actuation," *Proc. of the SPIE - The International Society for Optical Engineering,* <u>3224</u>, 109-119 (1997).

[22]   J.-L.A. Yeh, C.-Y. Hui, and N.C. Tien, "Electrostatic model for an asymmetric vertical combdrive," *Journal of Microelectromechanical systems,* 9(1), 126-135 (2000).

[23]   U. Krishnamoorthy, and O. Solgaard, "Self-Aligned vertical comb-drive actuators for optical scanning micromirrors," *Optical MEMS'01*, 41-42 (2001).

[24]   J. Lee, Y. Ko, B. Choi, J. Kim, D. Jeon, "Linear actuation of silicon scanning mirror for laser display," *Optical MEMS'01*, 101-102 (2001).

[25]   S. Blackstone and T. Brosnihan, "SOI MEMS technologies for Optical Switching," *IEEE/LEOS International Conference on Optical MEMS*, 35-36 (2001).

[26]   S. Kwon, V. Milanovic, and L. P. Lee, "Vertical microlens scanner for 3D Imaging," *Proc. Solid-State Sensor and Actuator Workshop*, 227-230 (2002).

[27]   G. D. J. Su, H. Toshiyoshi, and M. C. Wu, "Surface-micromachined 2-D optical scanners with high-performance single-crystalline silicon micromirrors," *IEEE Photonics Technology Letters*, 13, 606-608 (2001).

[28]   H. Schenk, P. Durr, D. Kunze, H. Lakner, and H. Kuck, "A resonantly excited 2D-micro-scanning-mirror with large deflection," *Sensors & Actuators A(Physical)*, 89, 104-111 (2001).

[29]   S. Kwon, and L.P. Lee, "Stacked two dimensional microlens scanner for Micro Confocal Imaging Array," *15th Annual IEEE International MEMS 2002 Conference*, 483-486 (2002).

[30]   S. Kwon, V. Milanovic, and L. P. Lee, "Large-Displacement Vertical Microlens Scanner with Low Driving Voltage," *IEEE Photonics Technology Letters*, 14, 1572-1574 (2002).

[31]   P. R. Patterson, D. Hah, H. Nguyen, H. Toshiyoshi, R. Chao, and M. C. Wu, "A Scanning Micromirror with Angular Comb Drive Actuation", MEMS '02, 192-195 (2002).

[32]   W. Welters and L. Fokkink, "Fast electrically switchable capillary effect," *Langmuir*, 14, 1535-1538 (1998).

[33]   J. Lee and C. J. Kim, "Surface tension driven microactuation based on continuous electrowetting," *JMEMS,* 9(2), 171-80 (2000).

[34]   M. Washizu, "Electrostatic actuation of liquid droplets for micro-reactor applications," *IEEE Trans. on Industry Appli.*, 34(4), 732-737 (1998).

[35]   S. Ahn and Y. Kim, "Proposal of human eye's crystalline lens-like variable focusing lens," *Sensors and Actuators A*, A78(1), 48-53 (1999).

[36]   L. G. Commander, S. E. Day, and D. R. Selviah, "Variable focal length microlenses," *Optics Communications*, 177, 157-170 (1999).

[37]   B. Berge and J. Peseux, "Variable focal lens controlled by an external voltage: An application of electrowetting," *Eur. Phys. J. E*, 3, 159-163 (2000).

[38]   C. B. Gorman, H. Biebuyck, and G. Whitesides, "Control of the shape of liquid lenses on a midified gold surface using an applied electrical potential across a self-assembled monolayer," *Langmuir*, 11, 2242-2246 (1995).

[39]   C. V. Raman, and K. S. Krishnan, "A New Type of Secondary Radiation," *Nature*, 121(3048), 501 (1928).

[40]   S. Nie and S. R. Emory, "Probing Single Molecules and Single Nanoparticles by Surface-Enhanced Raman," *Science*, 275, 1102-1106 (1997).

[41]   K. Kneipp, H. Kneipp, R. Manoharan, E. Hanlon, I. Itzkan, R. R. Dasari, M. S. Feld, "Extremely large enhancement factors in surface-enhanced Raman scattering for molecules on colloidal gold aggregates, *Appl. Spec.*, 52, 1493-1497 (1998).

[42]   K. Kneipp, A.S. Haka, H. Kneipp, K. Badizadegan, N. Yoshizawa, C. Boone, K.E. Shafer-Peltier, J.T. Motz, R.R. Dasari, and M.S. Feld, "Surface-Enhanced Raman Spectroscopy in Single Living Cells Using Gold Nanoparticles," *Appl. Spec.*, 56, 150-154 (2002).

[43]   Z.J. Zhang, S.F. Hou, Z.H. Zhu, and Z.F. Liu, "Preparation and Characterization of a Porphyrin Self-Assembled Monolayer with a Controlled Orientation on Gold," *Langmuir*, 16, 537-540. **(2000).**

[44]   W.C. Tang, T.-C.H. Nguyen, and R.T. Howe, "Laterally Driven Polysilicon Resonant Microstructures," *Sensors and Actuators*, <u>20(1-2)</u>, 25-32 (1989).

[45]   J.H. Comtois, V.M. Bright, and M.W. Phipps, "Thermal microactuators for surface-micromachining processes," *Proc. of SPIE - the International Society for Optical Engineering,* <u>2642</u>, 10-21 (1995).

[46]   Q. Long, P. Jae-Sung, and Y.B. Gianchandani, "Bent-beam electrothermal actuators-Part I: Single beam and cascaded devices," Journal of Microelectromechanical Systems, <u>10(2)</u>, 247-254 (2001).

[47]   P.A. Krulevitch, A.P. Lee, P.B. Ramsey, J. Trevino, J. Hamilton and M.A. Northrup, "Thin film shape memory alloy microactuators," *Journal of Microelectromechanical Systems*, <u>5(4)</u>, 270-782 (1996).

[48]   A. M. Flynn, L. S. Tavrow, S. F. Bart, R. A. Brooks, D. J. Ehrlich, K. R. Udayakumar, and L. E. Cross, "Piezoelectric micromotors for microrobots", *Journal of Microelectromechanical Systems*, <u>1(1)</u>, 44-51 (1992).

[49]   E.W.H. Jager, E. Smela and O. Inganas, "Microfabricating conjugated polymer actuators," *Science*, <u>290</u>,1540-1545 (2000).

[50]   E.W.H. Jager, O. Inganas, and I. Lundstrom, "Microrobots for micrometer-size objects in aqueous media: Potential tools for single-cell manipulation," *Science*, <u>288</u>, 2335-2338 (2000).

[51]   M. Okandan, P. Galambos, S. Mani, and J. Jakubczak, "Surface micromachined cell manipulation device for transfection and sample preparation," *Proc. of the Micro Total Analysis Systems Meeting*, 305-306 (2001).

[52]   P.I. Nikitin, A.A. Beloglazov, M.V. Valeiko, J.A. Creighton and J.D. Wright, "Silicon-based surface plasmon resonance combined with surface-enhanced Raman scattering for chemical sensing," *Rev. Sci. Instrum.*, <u>68(6)</u>, 2554-2557 (1997).

[53]   N. Felidj, J. Aubard, G. Levi, J.R. Krenn, A. Hohenau, G. Schider, A. Leitner, and F.R. Aussenegg, "Optomized surface-enhanced Raman scattering on gold nanoparticle arrays," *Appl. Phys. Lett.*, <u>82</u>, 3095-3097 (2003).

[54]   S. Kwon, G.L. Liu, K.H. Jeong and L.P. Lee, "Micro confocal line scanning system for multiplexed biochips," *Proc. 7th International Conference on Minaturized Chemical and Biochemical Analysis Systems*, 1255-1258 (2003).

[55]   D.L. Dickensheets and G.S. Kino, "A micromachined scanning confocal optical microscope," *Optics Letters*, <u>21</u>, 764-766 (1996).

[56] R. Juskaitis and T. Wilson, "Imaging in reciprocal fiber-optic based confocal scanning microscopes," *Opt. Commun.*, <u>92</u>**,** 315-325 (1992).

[57] M. A. Osborne, C. L. Barnes, S. Balasubramanian, and D. Klenerman, " Probing DNA surface attachment and local environment using single molecule spectroscopy," *Journal of Physical Chemistry B*, , <u>105</u>, 3120-3026 (2001).

[58] C. Peter, M. Meusel, F. Grawe, A. Katerkamp, K. Cammann and T. Borchers, "Optical DNA-sensor chip for real-time detection of hybridization events," *Fresenius' Journal of Analytical Chemistry*, <u>371</u>, 120-127 (2001).

[59] T. Funatsu, Y. Harada, M. Tokunaga, K. Saito and T. Yanagida, " Imaging of single fluorescent molecules and individual ATP turnovers by single myosin molecules in aqueous solution," *Nature*, <u>374</u>, 555-559 (1995).

[60] D. Axelrod, "Total internal reflection fluorescence microscopy in cell biology," *Traffic*, <u>2</u>, 764-774 (2001).

[61] K. Schult, A. Katerkamp, D. Trau, F. Grawe, K. Gammann and M. Meusel, "Disposable optical sensor chip for medical diagnostics: new ways in bioanalysis," *Analytical Chemistry*, <u>71</u>, 5430-5435 (1999).

[62] H.P Kao, N. Yang and J.S. Schoeniger, "Enhancement of evanescent fluorescence from fiber-optic sensors by thin-film sol-gel coatings," *Journal of the Optical Society of America A*, <u>15</u>, 2163-2171 (1998).

[63] J. Fujita, M. Levy, R. Scarmozzino, Jr. Osgood, R.M., L. Eldada, and J.T. Yardley, "Integrated multistack waveguide polarizer," *IEEE Photonics Technology Letters*, <u>10</u>, 93-5 (1998).

[64] G.L. Duveneck, M. Pawlak, D. Neuschafer, E. Bar, W. Budach, and U. Pieles, "Novel bioaffinity sensors for trace analysis based on luminescence excitation by planar waveguides," *Sensors and Actuators B*, <u>38-39</u>, 88-95 (1997).

[65] W. Budach, A.P. Abel, A.E. Bruno and D. Neuschafer, "Planar waveguides as high-performace sensing platforms for fluorescence-based multiplexed oligonucleotide hybridization assays," *Analytical Chemistry*, <u>71</u>, 3347-3355 (1999).

[66] A. Manz, N. Graber and H. M. Widmer, "Miniaturized total chemical analysis systems: A novel concept for chemical sensing," *Sensors and Actuators*, <u>B1</u>, 244-248 (1990).

[67] G.T.A. Kovacs, N.I. Maluf, and K.E. Petersen, "Bulk micromachining of silicon," *Proc. IEEE*, <u>86</u>, 1536-1551 (1998).

[68]   J.M. Bustillo, R.T. Howe, and R.S. Muller, "Surface Micromachining for Microelectromechanical Systems," *Proc. IEEE*, 86, 1552-1574 (1998).

[69]   Ph. Nussbaum, R. Völkel, H.P. Herzig, M. Eisner, and S. Haselbeck, "Design, fabrication and testing of microlens arrays for sensors and microsystems**,"** *Pure. Appl. Opt.,* 6, 617-636 (1997).

[70]   J. R. Wendt, M. E. Warren, W. C. Sweatt, C. G. Bailey, C. M. Matzke, D. W. Arnold, A. A. Allerman, T. R. Carter, R. E. Asbill, and S. Samora, **"**Fabrication of high performance microlenses for an integrated capillary channel electrochromatograph with fluorescence detection," *J. Vac. Sci. Technol.*, B17 3252-3255 (1999).

[71]   J.-C. Roulet, R. Volkel, H.P. Herzig, E. Verpoorte, N.F. de Rooij and R. Dandliker, **"**Microlens systems for fluorescence detection in chemical Microsystems**,"** *Opt. Eng*., 40, 814-821 (2001).

[72]   J. Hubner, K.B. Mogensen, A.M. Jorgensen, P. Friis, P. Telleman and J.P. Kutter, "Integrated optical measurement system for fluorescence spectroscopy in microfluidic channels," *Rev. Sci. Instrum.*, 72, 229-233 (2001).

[73]   B.G. Bryan and F.E. Lytle, "On-chip absorption measurements using an integrated waveguide," *Anal. Bioanal. Chem.*, 373, 519-525 (2002).

[74]   J. Kruger, K. Singh, A. O'Neill, C. Jackson, A. Morrison, and P. O'Brien, "Development of a microfluidic device for fluorescence activated cell sorting," *J. Micromech. Microeng.*, 12, 486-494 (2002).

[75]   J.R. Webster, M.A. Burns, D.T. Burke and C.H. Mastrangelo, "Electrophoresis system with integrated on-chip fluorescence detection**,"** *Proc. IEEE Thirteenth Annual Int. Workshop on Micro Electro Mechanical Systems*, 306-310 (2000)**.**

[76]   E. Thrush, O. Levi, K. Wang, J.S. Harris Jr. and S.J. Smith, "Integrated semiconductor fluorescent detection system for biochip and biomedical applications," *Proc. SPIE*, 4982, 289-297 (2002).

[77]   J. Guifeng; S. Attiya, G. Ocvirk, W.E. Lee and D.J. Harrison, "Red diode laser induced fluorescence detection with a confocal microscope on a microchip for capillary electrophoresis," *Biosens. Bioelectron*., 14, 861-869 (2000).

[78]   M.L. Chabinyc, D.T. Chiu, J.C. McDonald, A.D. Stroock, J.F. Christian, A.M. Karger, and G.M. Whitesides, **"**An integrated fluorescence detection system in poly(dimethylsiloxane) for microfluidic applications," *Anal. Chem.*, 73, 4491-4498 (2001).

[79]   A. Paulus, S.J. Williams, A.P. Sassi, K. Pin, H. Tan and H.H. Hooper, "Integrated capillary electrophoresis using glass and plastic chips for multiplexed DNA

analysis," *Proc. SPIE 1998 Symposium on Microfluidic Devices and Systems,* 94-103 (1998).

[80]   K. Kramer, Kwang W. Oh, C. H. Ahn, J. J. Bao, and K. R. Wehmeyer, "An optical MEMS-based fluorescence detection scheme with applications to capillary electrophoresis," *Proc. SPIE 1998 Symposium on Micromachining and Microfabrication,* 3515, 76-85 (1998).

[81]   J. Seo and L.P. Lee, "Integrated microfluidic optical systems (*i*MOS) with LED," *Proc. µTAS 2002 Symposium,* 1, 284-286 (2002).

[82]   J. A. Chediak, Z. Luo, J. Seo, N. Cheung, L.P. Lee, and T.D. Sands, "Hybrid integration of CdS filters with GaN LEDs for biophonic chips," *Proc. IEEE Sixteenth Annual Int. Conf. Micro Electro Mechanical Systems,* 323-326 (2003).

[83]   J.-C. Roulet, R. Völkel, H. P. Herzig, E. Verpoorte, N. F. de Rooij, and R. Dändliker, "Performance of an Integrated Microoptical System for Fluorescence Detection in Microfluidic Systems," *Anal. Chem.*, 74, 3400 – 3407 (2002).

[84]   Private communication with Dow Corning Corporation.

[85]   K. R. Williams and R. S. Muller, "Etch rates for micromachining processing," *J. Microelectromech. Syst.,* 5, 256-269 (1996).

[86]   C. Kuo-Shen, A. A. Ayon, Z. Xin, and S. M. Spearing, "Effect of process parameters on the surface morphology and mechanical performance of silicon structures after deep reactive ion etching (DRIE)," *J. Microelectromech. Syst.*, 11, 264-275 (2002).

[87]   D. Nilsson, S. Jensen, A. Kristensen, and A. Menon, "Silicon mold for casting polymer optics, "*Proc. Micromechanics Europe Conf. (MME 2002),* 111-114 (2002).

[88]   K. Brakke, "The surface evolver," *Experimental Mathematics*, 1, 141-165 (1992).

[89]   D. Axelrod, E.H. Hellen and R.M. Fullbright, *"*Total internal reflection fluorescence*," in* Topics in Fluorescence Spectroscopy, ch.7, J.Lakowicz, Plenum Press, New York (1992).

[90]   M. Wasilik and A. P. Pisano, "Low frequency process for silicon on insulator deep reactive ion etching," in *Proc. Device and Process Technologies for MEMS and Microelectronics II*, 462-472 (2001).

[91]   C. Sonnichse, T. Franzl, T. Wilk, G. von Plessen, J. Feldmann, O. Wilson and P. Mulvaney, "Drastic Reduction of Plasmon Damping in Gold Nanorods," *Phys. Rev. Lett.*, 88, 077402/1-077402/4 (2002).

[92]   M.V. Kunnavakkam, F.M. Houlihan, M. Schlax, J.A. Liddle, P. Kolodner, O. Nalamasu, and J.A. Rogers, "Low-cost, low-loss microlens arrays fabricated by soft-lithography replication process," *Appl. Phys. Lett.*, 82, 1152-1154 (2003).

[93]   A. Tronin and J.K. Blasie, "Variable acquistion angle total internal reflection fluorescence: A new technique for orientation distribution studies of ultrathin films," *Langmuir*, 17, 3696-3703 (2001).

[94]   R.R.A. Syms, "Refractive collimating microlens arrays by surface tension self-assembly," *IEEE Photonics Technology Letters*, 12, 1507-1509 (2000).

[95]   D.M. Freeman, A.J. Aranyosi, M.J. Gordon, and S.S. Hong, "Multidimensional motion analysis of MEMS using computer microvision," *Proc. IEEE Solid-State Sensor and Actuator Workshop*, 150-155 (1998),

[96]   S. Kwon, V. Milanovic, and L. P. Lee, "Large-Displacement Vertical Microlens Scanner with Low Driving Voltage," *IEEE Photonics Technology Letters*, 14, 1572-1574 (2002).

[97]   W.C. Tang, T.H. Nguyen, M.W. Judy and R.T. Howe, "Electrostatic-comb drive of lateral polysilicon resonators," *Sensors and Actuators*, A21-A23, 328-331 (1990).

[98]   D. W. Pierce, N. Hom-Booher and R.D. Vale, "Imaging individual green fluorescent proteins," *Nature*, 388, 338 (1997).

[99]   A. Menz and W. Benecke, "Silicon moulds for micro-injection moulding techniques," *Proc. MICRO.tec 2000,* 2, 645-648 (2000).

APPENDIX I. JOURNAL PUBLICATIONS

1. J. Seo, G. Liu, K. Jeong, and L.P. Lee, "A biochip for single molecular detection," to be published.

2. N. Chronis and L.P. Lee, "Polymer microrobotic workstation for single cell manipulation," to be submitted to Applied physics letters.

3. N. Chronis and L.P. Lee, "Electrothermally activated SU-8 microgripper for single cell manipulation," Journal of MicroElectroMechanical Systems (in press).

4. N. Chronis and L.P. Lee, "Polymer-based microrobotic workstation," to be submitted *to Nature Materials.*

5. K. Jeong, and L. P. Lee, "A novel microfabrication of a self-aligned vertical comb drive on a single SOI wafer for optical MEMS applications," J. Micromechanics and Microengineering, (in revision in October, 2004).

6. J.A Chediak, Z.S. Luo, J. Seo, N. Cheung, L.P. Lee and T.M. Sands, "Heterogeneous integration of CdS filters with GaN LEDs for fluorescence detection microsystems," *Sensors & Actuators A-Physical,* <u>A111</u>, 1-7 (2004).

7. J. Seo and L.P. Lee, "Disposable integrated microfludics with self-aligned planar microlenses," *Sensors & Actuators B-Chemical*, <u>B99</u>, 615-622 (2004).

8.   J. Seo and L.P. Lee, "Fluorescence enhancement in microfludics with self-aligned planar microlenses for single molecule detection," *Lab on a chip* (to be submitted).

9. S. Kwon, V. Milanovic and L. P. Lee, "Vertical combdrive based 2D gimbaled micromirrors with large static rotation by backside island isolation," Journal of Selective Topics in Quantum Electronics, <u>10</u>, (2004).

10. S. Kwon and L. P. Lee, "Micromachined lens scanning confocal microscopes," *Optics Letters*, 29, (2004).

11. S. Kwon, and L. P. Lee, "Stacked 2D microlens scanners," (submitted to) *Journal of Microelectromechanical Systems* (2003).

12. S. Chan, S. Kwon, T. Koo, L. P. Lee and A. A. Berlin, "Optical detection of small molecules using silicon nanopores as a surface enhanced Raman scattering (SERS) substrate," *Advanced Materials*, <u>15</u>, 1595-1598 (2003).

13. V. Milanovic, S. Kwon, L. P. Lee, "High aspect ratio silicon micromirrors with large static rotation and piston actuation," *IEEE Photonics Technology Letters (*2003) (in press).

14. S. Kwon, V. Milanovic, and L. P. Lee, "Large-Displacement Vertical Microlens Scanner With Low Driving Voltage," *IEEE Photonics Technology Letters*, <u>14</u>, 1572-1574 (2002).

APPENDIX II. CONFERENCE PUBLICATIONS

1. S. Kwon, G. L. Liu, K. Jeong, and L. P. Lee, "Micro confocal line scanner for multiplexed BioChips," *Proc. IEEE/LEOS Optical MEMS 2003*, 149 -150 (2003).

2. S. Kwon and L. P. Lee, "Stacked two dimensional micro-lens scanner for micro confocal imaging array," *Proc. IEEE Micro Electro Mechanical Systems, MEMS 2002*, 483-486 (2002).

3. S. Kwon, V. Milanovic, and L. P. Lee, "Vertical microlens scanner for 3D imaging," *Proc. IEEE Solid-State Sensor and Actuator Workshop, Hilton Head 2002,* 227-231 (2002).

4. S. Kwon, V. Milanovic, and L. P. Lee, "A high aspect ratio 2D gimbaled microscanner with large static rotation," *Proc. IEEE/LEOS Optical MEMS 2002*, 149 -150 (2002).

5. S. Kwon and L. P. Lee, "Focal length control by microfabricated planar electrodes-based liquid lens," *Proc. Solid State Sensors and Actuators, Transducers 2001*, 2, 1348-1351 (2001).

6. S. Kwon and L. P. Lee, "Programmable optochemical microprocessor for nanoscale biochemical analysis applications," ACS 2001 (2001).

7. N. Chronis and L.P. Lee, "Polymer-based microrobotic workstation for single cell analysis", to be presented in the *Eight International Conference on Micro Total Analysis Systems (µTAS)*, Sweden, Sept 2003.

8. N. Chronis and L.P. Lee, "Polymer MEMS-based microgripper for single cell manipulation", *17th IEEE International Conference on Micro Electro Mechanical Systems*, 17-20 (2004).

9. N. Chronis and L.P. Lee, "Total internal reflection-based biochip for high throughput bioassays," *Seventh International Conference on Micro Total Analysis Systems (µTAS)*, 1323-1326 (2003).

10. N. Chronis N. and L. P. Lee, "Polymer-based actuators integrated into microfluidic systems", *Sixth International Conference on Micro Total Analysis Systems (µTAS)*, 754-757 (2002).

11. K. H. Jeong, and L. P. Lee, "A new method of increasing numerical aperture of microlens for biophotonic MEMS", The 2nd Annual International IEEE-EMBS Special Topic Conference on Microtechnologies in Medicine & Biology, 380 -383 (2002).

12. K. H. Jeong, S. B. Oh and L.P. Lee, "Hydrophobic sealing for integrated microactuators in biofluidic system," *Proceedings of the MicroTAS Symposium*, 157-158 (2001).

13. K. H. Jeong, L.P. Lee, "A novel fabrication method of a vertical comb using a single SOI wafer", Transducers 2003, (2003).

14. J. Seo and L.P. Lee, "Self-aligned microlens arrays on microfluidic devices for nanovolume bioassay," *221st National Meeting, American Chemical Society* (2001).

15. J. Seo and L.P. Lee, "Selective plasma surface modification for self-aligned microlens arrays on microfluidic systems," *The Fifth International Symposium on Micro Total Analysis Systems (µTAS)*, 389-390 (2001).

16. J. Seo, Ertekin E., Pio M. S., and L. P. Lee, "Self-assembly templates by selective plasma surface modification of micropatterned photoresist," *15th IEEE International Micro Electro Mechanical Systems Conference*, 192-195 (2002).

17. J. Seo and L.P. Lee, "Integrated Si$_x$N$_y$ membrane mirofluidic circuits with single molecule detection and manipulation capability," *LabAutomation 2002*, (2002).

18. J. Seo , C. L. Kuyper, D.T. Chiu, and L.P. Lee, "Biophotonic MEMS for single molecule detection and manipulation," *Second Annual International IEEE-EMBS Special Topic Conference on Microtechnologies in Medicine & Biology*, 363-368, (2003) (Invited Talk).

19. J. Seo, and L.P. Lee, "Disposable integrated microfluidic optical systems (*i*MOS)," The SmallTalk2002 (The Microfluidics, Microarrays and BioMEMS Conference) (2002) (Best poster award).

20. J. Seo and L.P. Lee, "Integrated microfluidic optical systems (*i*MOS)," *The Sixth International Symposium on Micro Total Analysis System* (µTAS 2002), 284-286 (2002).

21. J. Seo, Oh S., and L.P. Lee, "Single layer 2-D optical scanners with integrated polymer microlenses," *IEEE/LEOS International Conference on Optical MEMS*, 151-152 (2003).

22. J.A. Chediak, Z. Luo, J. Seo, N. Cheung, L.P. Lee, and T.D. Sands, "Hybrid integration of CdS filters with GaN LEDs for biophonic chips," *Proc. IEEE Sixteenth Annual Int. Conf. Micro Electro Mechanical Systems*, 323-326. (2003).

23. Luo Z.S., Sands T., N.W. Cheung, J.A. Chediak, J. Seo, and L.P. Lee, "Pixel-to-point transfer: a process for integrating individual GaN-based light-emitting devices in heterogeneous Microsystems," *Integration of Heterogeneous Thin-Film Materials*

and Devices Symposium (Mater. Res. Soc. Symposium Proceeding, <u>768</u>, 117-121 (2003).

24. J. Seo and L.P. Lee, "Fluorescence amplification by self-aligned integrated microfluidic optical systems," *The 12th International Conference on Solid-state Sensors, Actuators and Microsystems (Transducers '03)*, 1136-1139 (2003).